THE SPECTRAL CHARACTERISTICS OF WIND-FARM POWER OUTPUT

BY

NICOLAS TOBIN

DISSERTATION

Submitted in partial fulfillment of the requirements
for the degree of Doctor of Philiosphy in Theoretical and Applied Mechanics
in the Graduate College of the
University of Illinois at Urbana-Champaign, 2018

Urbana, Illinois

Doctoral Committee:

Assistant Professor Leonardo P. Chamorro, Chair and Director of Research
Professor Marcelo Garcia
Professor Carlos Pantano-Rubino
Assistant Professor Aimy Wissa

Abstract

Over time-scales short enough that wind is relatively steady ($\lesssim$10 minutes), wind-power variability is due to atmospheric turbulence. Power fluctuations at time scales such as these are important for maintaining frequency regulation on the power grid. This thesis presents a holistic, physics-based approach to modeling the spatio-temporal structures of the atmospheric boundary layer, and the ways in which these structures impart themselves in wind-power variability. The following primary findings are presented.

Field and laboratory experiments were performed to unravel the structure of the power output fluctuations of horizontal-axis wind turbines based on incoming flow turbulence. The study considers the power data of three wind turbines of rotor sizes 0.12 m, 3.2 m and 96 m, with rated power spanning 6 decades from the order of 10^0 to 10^6 W. The 0.12 m wind turbine was tested in a wind tunnel while the 3.2 and 96 m wind turbines were operated in open fields under approximately neutrally-stratified thermal conditions. Incoming flow turbulence was characterized by hotwire and sonic anemometers for the wind tunnel and field setups. While previous works have observed a filtering behavior in wind turbine power output, this exact behavior has not, to date, been properly characterized. Based on the spectral structure of the incoming flow turbulence at hub height, and the mechanical and structural properties of the turbines, a physical basis for the behavior of temporal power fluctuations and their spectral structure is found with potential applications in turbine control and numerical simulations. Consistent results are observed across the geometrical scales of the wind turbines investigated, suggesting no Reynolds number dependence in the tested range.

The structure of the turbulence-driven power fluctuations in a wind farm is fundamentally described from basic concepts. A derived tuning-free model, supported with experiments, reveals the underlying spectral content of the power fluctuations of a wind farm. It contains two power-law trends and oscillations in the relatively low- and high-frequency ranges. The former is mostly due to the turbulent interaction between the flow and the turbine properties; whereas the latter is due to the advection between turbine pairs. The spectral wind-farm scale power fluctuations Φ_P exhibits a power-law decay proportional to $f^{-5/3-2}$ in the region corresponding to the turbulence inertial subrange and at relatively large scales, $\Phi_P \sim f^{-2}$. Due to the advection and turbulent diffusion of large-scale structures, a spectral oscillation exists with the product of a sinusoidal behavior and an exponential decay in the frequency domain.

Simultaneous power measurements from a model wind farm are presented to investigate the spectral correlation of their power output. Application of a random-sweeping hypothesis to the turbulent flow in a wind farm uncovers distinctive correlations, characterized by advection and turbulent diffusion of coherent motions. This correlation is most evident in the cross-spectra of power output between turbine pairs, which contributes to peaks and troughs in the power spectra of the combined signals. These peaks and troughs occur at frequencies corresponding to the advection time between turbines, and diminish in magnitude at high frequencies due to turbulent decoherence. Experimental results support the results from the random-sweeping hypothesis in predicting characteristic advection and decoherence frequencies. The presence of turbine wakes leads to coherence magnitudes smaller than expected. This difference appears to be a function of the flow approaching the first turbine in a pair. The impact of lateral displacement is unclear from the data.

Wind-farm large-eddy simulations are used to uncover the dependence of temporal correlations in the power output of turbine pairs on atmospheric stability. For this purpose, a range of five distinct stability regimes are investigated with the same aligned wind-farm layout used among simulations. The coherence spectrum between turbine pairs in each simulation is compared to theoretical predictions. We found that higher levels of atmospheric instability lead to higher coherence between turbines. This is attributed to higher dominance of atmospheric motions over wakes in highly unstable flows. An empirical model for wake-added turbulence is shown to adequately predict the variation of coherence with ambient turbulence intensity.

The modulation of boundary-layer turbulence across scales by passage through the rotor of a model wind turbine is assessed experimentally using synchronous upwind and downwind hotwire anemometers. Consistent with literature, results show that the rotor simultaneously eliminates large-scale motions, and introduces comparatively small-scale flow structures. The synchronous data allows for the distinct quantification of added and dampened turbulence by considering the temporal correlation between upwind and downwind time series. The destroyed turbulence is of a larger characteristic length scale than the created turbulence, but both scales increase with downwind distance. The intensity of the destroyed turbulence does not change substantially with downwind distance, suggesting that the turbine has a much stronger effect on turbulence destruction than simple natural evolution. The cross spectra between upwind and downwind velocity measurements suggest a dispersion relation for different time scales. In the near wake, lower-frequency components appear to be advected at velocity lower than the local wake velocity, and this advection velocity asymptotically approaches the local velocity at high frequency. This trend diminishes in magnitude with downwind distance.

Acknowledgments

Many people contributed to the completion of this work, and I want to express my gratitude to everyone who was involved in some way. Many thanks to my adviser, Leo Chamorro, who had a part in every last revision and always pushed me to go bigger. Thanks also to all of my labmates, who made my time spent at UIUC all the better. Of course, none of this work would have been possible without my collaborators, including Hao Zhu, Ali Hamed, Huiwen Liu, Yaqing Jin, Adam Lavely, Sven Schmitz, Matias Colombo, Imran Hayat, and Shifeng Fu. I would also like to acknowledge the support of the National Science Foundation, which supported me through both a fellowship and a research grant. Thank you to my parents, Melissa Lunderby, and the rest of my family for their love and support. Thank you also to all the new friends I made in Champaign-Urbana, who made this town feel like home, and to the friends I left two states away but who are as close as ever.

Table of Contents

List of Tables . . . . **vii**

List of Figures . . . . **viii**

Chapter 1 Introduction **1**
- 1.1 Interactions Between Wind Farms and The Atmospheric Boundary Layer 3
- 1.2 The Spectral Relation Between Turbulence and Power 4
- 1.3 Objectives 5
- 1.4 Outline 6

Chapter 2 Filtering of Small Scales by Turbine Rotors **9**
- 2.1 Abstract 9
- 2.2 Introduction 9
- 2.3 Experimental set-up 11
  - 2.3.1 Miniature wind turbine 12
  - 2.3.2 Small wind turbine 12
  - 2.3.3 Full-scale wind turbine 19
- 2.4 Analysis 19
  - 2.4.1 Turbine power fluctuations 19
  - 2.4.2 Evaluation of Results 22
  - 2.4.3 Discussion 24
- 2.5 Final Remarks 28

Chapter 3 Integrated Modeling of the Power Spectra of a Wind Farm **30**
- 3.1 Abstract 30
- 3.2 Introduction 30
- 3.3 Experimental Setup 32
- 3.4 Results and discussion 33
  - 3.4.1 Power fluctuations of turbines in wind farms 33
  - 3.4.2 Wind farm power fluctuations 36
  - 3.4.3 Wind-farm power from global incoming flow 38
  - 3.4.4 Covariance due to advection and turbulent diffusion . . . 38
- 3.5 Summary 43

Chapter 4 Experimental Investigation of Spatio-Temporal Power Correlations **46**
- 4.1 Abstract 46
- 4.2 Introduction 46
- 4.3 Cross Spectra in Wind Farms 48
  - 4.3.1 Coherence Spectrum 48

    - 4.3.2 Random Sweeping and the Coherence of Wall-Bounded Turbulence . . . 48
- 4.4 Experiments . . . 50
    - 4.4.1 Turbulent and Laminar Freestreams . . . 50
    - 4.4.2 Rough- and Smooth-Wall Boundary Layers . . . 51
- 4.5 Results . . . 51
- 4.6 Concluding Remarks . . . 59

Chapter 5 Numerical Investigation of Spatio-Temporal Power Correlations . . . 60
- 5.1 Abstract . . . 60
- 5.2 Introduction . . . 60
- 5.3 Coherence and the Random Sweeping Hypothesis . . . 62
- 5.4 Large-Eddy Simulations . . . 63
- 5.5 Results and Discussion . . . 66
    - 5.5.1 Advection of Turbulent Motions . . . 68
    - 5.5.2 Turbulent Decoherence of Turbulent Motions . . . 70
    - 5.5.3 Coherence Scaling Factor . . . 70
- 5.6 Conclusion . . . 72

Chapter 6 Modulation of Turbulence Scales Passing Through the Rotor of a Wind Turbine . . . 76
- 6.1 Abstract . . . 76
- 6.2 Introduction . . . 76
- 6.3 Experimental Setup . . . 78
- 6.4 Analysis . . . 79
- 6.5 Concluding Remarks . . . 89

Chapter 7 Conclusions and Future Directions . . . 91
- 7.1 Conclusions . . . 91
- 7.2 Unaddressed Topics . . . 91

References . . . 93

List of Tables

2.1 Basic geometry of the blades of the miniature and small wind turbine normalized by the rotor radius: c is the chord length, (α) is the angle with respect to the rotor plane. R is the rotor radius 15

2.2 Measured and estimated standard deviation of power fluctuations (σ_p) for the three turbines 27

5.1 The atmospheric stability states used for the wind farm simulations. 66

5.2 Number of windows used in calculating coherence from LES data across ranges of frequencies. 66

List of Figures

1.1 Levelized wind PPA prices by PPA execution date and region. Reproduced from [133]. 2
1.2 Wind-turbine wakes are visualized by fog formation in the Horns Rev 1 wind farm. Photo by Christian Steiness. 8

2.1 (a) Photograph of the Talbot Laboratory wind tunnel in the test section pointing downwind. (b) Schematic and (c) photographs of the miniature wind turbine. 13
2.2 Sample velocity and power output fluctuations for the miniature (a,b) and small (c,d) wind turbines. 14
2.3 (a) Photograph of the small wind turbine and the array of CSAT3 sonic anemometers. (b) Close look of the array of sonic anemometers facing upwind. 16
2.4 Incoming flow statistics normalized with the streamwise velocity at hub height. (a) Mean velocity. (b) Turbulence intensity. (c) Kinematic shear stress. 17
2.5 Left: (a) Schematic of the NACA 632-615 airfoil section. (b) Lift and (c) Drag coefficients of the blade airfoil section at Reynolds numbers of $Re_d = 1.5 \times 10^7$ and 4.5×10^9. 18
2.6 Conceptual schematic of turbine power response to incoming velocity via a transfer function 20
2.7 Fourier transform of impulse response function 23
2.8 Measured and modeled power output spectra for the three turbines. (a) Full-scale. (b) Small. (c) Miniature. 25
2.9 Measured and estimated real-time fluctuating power for the (a) full scale and (b) small wind turbines. 26
2.10 Model and measured power spectra of (a) 2.5 MW, (b) 1 kW and (c) 650 mW turbines 29

3.1 a) Photograph of the test section pointing upwind; b) Mean velocity U/U_{hub}; c) turbulence intensity $I_u = \sigma_u/U_{hub}$. Horizontal lines indicate the turbine-hub height. 34
3.2 Spectra of incoming turbulence (*red*), $\hat{G}(f)$ (*blue*) and turbine output power (*black*) of a) 1st and b) 4th row, $S_x = 7$; c) 4th row, $S_x = 10$. 35
3.3 Pre-multiplied power spectra of a) the local incoming velocity and b) the power output of the 1st, 2nd and 4th rows with $S_x = 7$ and 10 (solid and dotted lines). 37
3.4 Measured and modeled spectra of hub-height velocity of incoming flow (sub-figures) and output power inside wind farm. a) 5th row, $S_x = 7$; b) 4th row, $S_x = 10$. 39

3.5 Measured and modeled power variance of individual turbines in the wind farm with $S_x = 7$ (o) and $S_x = 10$ ($\triangle$). 40
3.6 a) Mean velocity (U/U_{hub}) and b) turbulence intensity I_u within the $S_x = 7$, c) Mean velocity (U/U_{hub}) and d) turbulence intensity I_u within the $S_x = 10$ model wind farm at hub height. 41
3.7 Measured and modeled spectra of output power in the wind farm. a) five rows, $S_x = 7$; b) four rows, $S_x = 10$. 44

4.1 Conceptual schematic freestream experiments. 52
4.2 Conceptual schematic boundary-layer experiments. 53
4.3 Sample coherence data from the rough-wall, $7D$-spacing experiment. 55
4.4 Conceptual schematic boundary-layer experiments. 56
4.5 Conceptual schematic boundary-layer experiments. 57
4.6 Dependence of zero-frequency coherence magnitude on turbulence intensity and integral time scale. 58

5.1 Isocontours of horizontal velocity at turbine hub height superimposed with isosurfaces of vertical velocity $u_z = -1$ m s^{-1}, for the 5 km × 5 km precursor simulation. 65
5.2 Sample coherence spectrum from two wind turbines in a neutral boundary layer flow. 67
5.3 Mean least-squares estimate of f_a for all flow cases. 69
5.4 Mean least-squares estimate of f_c for all flow cases. Dashed lines show RSH predictions for the different flow cases, with the indicated dependence trend on σ_1, the standard deviation of streamwise velocity. 71
5.5 Coherence scaling factor vs. expected fraction of coherent turbulence intensity. 73
5.6 Predicted coherence scaling factor vs. boundary-layer turbulence intensity. 74

6.1 Characteristics of the incoming boundary layer; a) mean velocity profile, b) turbulence intensity, c) power spectrum of streamwise velocity component. 80
6.2 Basic schematic of the experimental setup illustrating the synchronized flow measurements upwind and downwind of the model turbine using two hotwire anemometers. 81
6.3 Upwind, downwind, and downwind coherent velocity spectra: a) without turbine present; b) with turbine present. 82
6.4 The premultiplied wake-added power spectrum with downwind distance. 84
6.5 The premultiplied wake-destroyed power spectrum with downwind distance. 85
6.6 Evolution of added and destroyed turbulence intensity with downwind distance. 87
6.7 Evolution of added and destroyed integral time scale with downwind distance. 88
6.8 Conceptual schematic freestream experiments. 90

Chapter 1

Introduction

In recent years, wind power has become an effective and mainstream source of electricity in the United States, bringing along with it a number of benefits, ranging from preventing the emission of greenhouse gases, providing low-cost energy, and increasing development in rural areas. As electricity demand continues to grow, wind will play an important role in the domestic energy market.

According to the Department of Energy's 2016 Wind Technologies Market Report, 2016 saw an addition of 8203 MW of new nameplate capacity in the United States, amounting to an 11% increase in cumulative capacity. This places wind behind solar and natural gas power in terms of new capacity, with 27% of all new additions. This strong growth is primarily as a result of low cost due to improvements in technology and the extension of the federal Production Tax Credit (PTC). After an increase in prices for power purchase agreements (PPA) in the years leading up to 2009, seen in Figure 1.1 average prices have reduced to $20/MWh, significantly undercutting natural gas. The technological improvements that have driven this reduction in cost primarily do so by increasing the capacity of a turbine, i.e. taller towers, longer and lighter blades, and more efficient generators. In 2016, the average capacity of new turbines was 2.1 MW, an 11% increase from the years 2011-2015. This is primarily attributed to a 13% increase in the average rotor diameter in the same time, though the impact of larger rotors was tampered by the trend toward installing turbines in lower-resource sites.

As new projects transition to sites with less wind resource, there has similarly been a trend toward including a larger number of turbines into a wind farm, with the average new project in 2016 having a capacity of 132 MW. When large wind farms are built, it is clear that interactions between the array of turbines and the atmospheric boundary layer (ABL) become important. This problem is often exemplified by the famous picture of the Horns Rev wind farm in Denmark, shown in Figure 1.2, where the low pressure region in the turbine wakes has precipitated fog formation. This image showcases the importance of wakes in wind farm operation. The wake region behind a turbine is characterized by lower wind speeds and higher turbulence intensity. For a turbine in another's wake, this has the general effect of reducing power output and effective lifetimes, as unsteady forcing stresses the mechanical components. This wake loss has

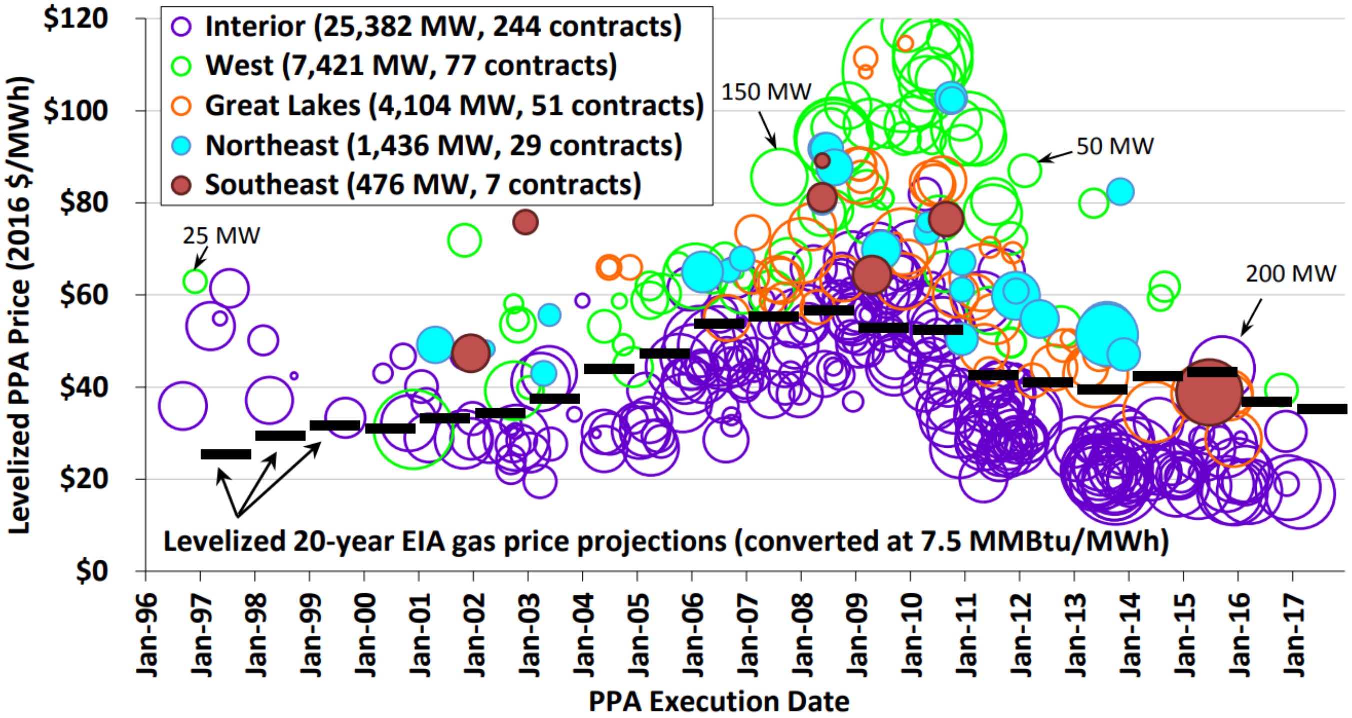

Figure 1.1: Levelized wind PPA prices by PPA execution date and region. Reproduced from [133].

been observed to reduce the power output of a turbine in the inner rows of a wind farm as compared to the first row up to the order of 50% [8]. However, the turbulent nature of the ABL tends to spread these wakes and lessen their impact by entraining more high-momentum fluid from above the wind farm into the level of the turbine rotors. Because of this, in later rows of turbines in a very large wind farm, the power production typically levels off to an asymptotic value. It has been shown experimentally that this asymptotic value is related to the turbulent downward flux of kinetic energy [15] from the energetic freestream atmosphere above the wind farm.

As it is the ABL that replenishes the extracted energy in a wind farm, it is clear that the power output of turbines in an array is inextricably linked to the large-scale characteristics of the ABL. The turbulent nature of the atmosphere then leads to the characteristic variability in wind power. Although wind-power variability occurs over a wide range of time scales, this linkage between turbulence and power fluctuations has important implications for grid operations, leading to power fluctuations on the order of 20%, even in conditions when the atmospheric flow is steady over long time periods. These fluctuations due to turbulence can occur over time scales ranging from seconds to tens of minutes, and are affected not only by the current state of the atmosphere, but by the mechanical characteristics of the turbines in a wind farm, the layout of the turbines, and their operational condition.

The goal of this dissertation is to form a greater understanding of the interaction between wind farms and the ABL, in particular focusing on the impact of the characteristics of turbulence, and the operational status of wind turbines. The motivation for this work is detailed in the following sections of this chapter.

1.1 Interactions Between Wind Farms and The Atmospheric Boundary Layer

The guiding goal of developing an in-depth understanding of wind farm/ABL interactions is to improve wind-farm performance. Although there is a variety of methods being applied to improve wind-farm performance, within the community investigating atmospheric phenomena in wind farms, this means the achieving the highest, least turbulent winds. Reductions in wind speeds can lead to substantially reduced power output, since the power of a turbine is proportional to the cube of the wind speed. Wind-speed reductions are typically due either to geographical features, or more commonly, the wakes of upwind turbines. These same aspects, geography and turbine wakes, can both also lead to higher levels of turbulence within wind farms, and therefore higher costs associated with dynamic loading on blades, gearboxes, etc.

Experiments in wind-farm flows are necessary in order to both uncover important governing physics, and validate theoretical models. These theoretical models are an important contribution to the overall goal of improving wind-farm performance. For instance, layout optimization of a wind farm benefits from simple analytical models, such as the early work of S. Lissaman [101] and Katic et al. [60], which include methods of superposing wakes from several upwind turbines, in order to estimate the total velocity deficit approaching a turbine deep within a wind farm. These simplified models are helpful, since they can easily be evaluated thousands of times, and can be incorporated into, for instance, a genetic algorithm to find optimal layouts. In contrast to analytical models, the most detailed modeling of wind-farm fluid dynamics commonly used is large-eddy simulations (LES). LES solves a spatially filtered version of the Navier-Stokes equations to fully simulate unsteady turbulent flows, and can result in data with extremely high temporal and spatial resolution. However, this comes at a much higher computational cost, with LES studies of wind farms typically requiring access to high-performance computing systems.

1.2 The Spectral Relation Between Turbulence and Power

One of the most important insights in quantifying the variability of wind power is its relation to ABL turbulence. Among the earliest observations of the fluctuating character of wind power was the work of Apt [3], who observed that the power spectrum of power fluctuations from wind turbines and small wind farms obeyed a power law of $f^{-5/3}$, consistent with Kolmogorov scaling of isotropic turbulence [66]. This parallel is commonly attributed to the idea of wind turbines acting as a probe of the turbulence. At short time scales over which the flow is steady, this can be justified by considering the wind-turbine power equation:

$$P = 1/2\rho C_P A u^3 = 1/2\rho C_P A(\overline{U} + u')^3, \tag{1.1}$$

where ρ is the density of air, C_P is the power coefficient of the turbine, A is the swept area of the rotor, u is the velocity approaching the turbine, $\overline{U}$ is the average of u, and $u' = u - \overline{U}$. By assuming that $u' \ll \overline{U}$, it is clear that

$$P' = 3/2\rho C_P A u', \tag{1.2}$$

where P' is the fluctuation part of the power. Other arguments can be made to show that arbitrary powers of u will also exhibit classical Kolmogorov scaling. This idea does, however, break down at very short time scales, when the inertia and response of the rotor determines the qualities of the power fluctuations.

This assumption of turbines as probes of the turbulence allows for other classical approaches in turbulence theory to be applied to the aggregate power of many turbines in a wind farm by considering the spatio-temporal correlations in a turbulent boundary layer. For instance, Bossuyt et al. [13] applied the Random Sweeping Hypothesis (RSH) with empirical formulations for the two-dimensional wavenumber spectrum of a turbulent boundary layer to propose a method of predicting the properties of aggregate power fluctuations in a wind farm, and observed a characteristic time scale of the fluctuations corresponding to the time it takes for a turbulent motion to pass between turbines.

However, in the works of Bossuyt et al. [13] and Liu et al. [77], it is clear that treating the turbines as active probes of the turbulence is an inadequate assumption, since they introduce wakes to the flow, which are highly energetic, small in scale, and break down from highly coherent trailing vortices. This assumption of the turbines acting as passive probes essentially over-predicts the magnitude of fluctuations, hinting toward a treatment for wakes as weakly correlated.

1.3 Objectives

The overarching objective of this thesis is to provide a detailed accounting of how ABL turbulence leads to wind-power fluctuations at short time scales ($\lesssim$ 20 minutes) which are important for grid operation. The topics explored are briefly detailed below.

- For a single turbine operating in the atmospheric boundary layer, to what extent is the assumption of an ideal probe valid? What is the role of rotor inertia in determining the response of the turbine to turbulent scales, and what time scales does the turbine response introduce to the power fluctuations?

- Can an integrated power fluctuation modeling framework be developed which accounts for the modulation of the flow by upwind turbines? How can existing engineering models be incorporated into this framework, and what are the shortcomings of such an approach?

- How are turbines correlated with each other in a wind farm? How, specifically, does the assumption of the turbines as passive probes impact the validity of theoretical predictions made? What is the role of wakes, and does this role diminish depending on the ambient turbulence?

- If the diminishing role of wakes does change with ambient turbulence, does this occur to an extent that is appreciable over a diurnal cycle? For typical atmospheric stability states, do the characteristics of turbine-turbine power correlations change?

- How do turbine wakes change the correlations existing in a turbulent boundary layer? How do wake-added motions evolve downwind, and how are they correlated with upwind ABL motions?

1.4 Outline

This thesis broadly presents a set of five journal articles which investigate the questions mentioned, the last three of which are currently under review.

The first of these articles, Chapter 2, appears in the Journal of Turbulence with the title *Spectral behaviour of the turbulence-driven power fluctuations of wind turbines*[121]. This articles experimentally investigates the power fluctuations of three wind turbines of different size, ranging from a rotor diameter of 0.12 m to one of 90 m. The filtering behavior of the turbines at relatively high frequencies is quantified, and shown to be well predicted by considering the inputs and outputs of kinetic energy in the rotor of the turbine. A filtering time scale is defined based on rotor inertia, and an engineering approach to modeling power fluctuations from a single turbine is provided.

Chapter 3 consists of a journal article appearing in Physical Review E with the title *Towards uncovering the structure of power fluctuations in wind farms.* This article extends the previous work to present an integrated approach to modeling aggregate power fluctuations from a wind farm, incorporating existing engineering models for the turbulence intensity, integral time scales, and mean velocity in the wakes of turbines. The role of turbine-turbine covariance is explored, and the RSH is investigated for its ability to predict this covariance. Power time series are measured from a simulated wind farm in a wind tunnel, and the characteristics of the power fluctuations are found to agree with predictions made with the proposed integrated modeling approach.

Chapter 4 is a manuscript entitled *Turbulence Coherence and its Impact on Wind-Farm Power Fluctuations*, and is under review in the Journal of Fluid Mechanics. The goal of this paper is to take a deeper look into the idealized assumptions of using the random sweeping hypothesis for turbine-turbine correlations in a turbulent boundary layer. Specifically, the role of ambient turbulence is experimentally investigated in the wind tunnel. It is found that the incoming turbulence intensity strongly impacts the ability of the RSH to make valid predictions, and that turbine-turbine correlations are over-predicted, particularly when the ambient turbulence intensity is low. Arguments are made to attribute this over-prediction to turbine wakes modulating the turbulent motions in the ABL.

A manuscript titled *The Impact of Atmospheric Stability on Wind-Power Coherence* is presented in Chapter 5, which is currently under review in the journal Physical Review Fluids. Inspired by the observation of over-predicted turbine-turbine correlations in very low turbulence environments, the goal of this manuscript is to investigate the amount by which turbine-turbine correlations can change over a diurnal cycle, in which the characteristics of the atmospheric boundary layer are impacted by the surface heating by solar irradiation. Large-eddy simulations are performed of a wind farm operating in boundary layers of varying atmospheric stability states, and it is found that the highly stable nocturnal boundary layer does lead to lower turbine-turbine correlation values. A simplified modeling approach for the over-prediction by the RSH of turbine-turbine correlation is investigated based on the assumption that wake-added motions lead to power fluctuations in downwind turbines which are uncorrelated with the power output of the turbine from which they are shed, which adequately captures the over-prediction behavior.

The final technical chapter, Chapter 6, is under review in the Journal of Turbulence with the title *Modulation of turbulence scales passing through the rotor of a wind turbine.* The purpose of this paper is to experimentally quantify the characteristics of the turbulence that has passed through a wind-turbine rotor. By synchronously measuring upwind and downwind velocity time series, statistical methods are applied to attribute downwind turbulence motions either to the wake or the atmospheric boundary layer. A distinction is made between wake-added motions, which evolve from the vortex shed from the turbine's hub, and wake-destroyed motions, which are large-scale motions that approach the turbine and lose coherence with their downwind counterparts. It is found that wake-destroyed motions slowly decrease in integral time scale with downwind distance, potentially from impinging of boundary-layer motions, while wake-added motions become less energetic and larger in scale, and are consistent with previous observation of wake meandering.

Finally, a number of unanswered questions and closing thoughts are include in Chapter 7.

Figure 1.2: Wind-turbine wakes are visualized by fog formation in the Horns Rev 1 wind farm. Photo by Christian Steiness.

Chapter 2

Filtering of Small Scales by Turbine Rotors

The contents of this chapter appear in the Journal of Turbulence [121], and are reproduced with permission from the Taylor & Francis Group on the condition of proper acknowledgment and the inclusion of a reference to the article on the journal's website.

2.1 Abstract

Field and laboratory experiments were performed to unravel the structure of the power output fluctuations of horizontal-axis wind turbines based on incoming flow turbulence. The study considers the power data of three wind turbines of rotor sizes 0.12 m, 3.2 m and 96 m, with rated power spanning 6 decades from the order of 10^0 to 10^6 W. The 0.12 m wind turbine was tested in a wind tunnel while the 3.2 and 96 m wind turbines were operated in open fields under approximately neutrally-stratified thermal conditions. Incoming flow turbulence was characterized by hotwire and sonic anemometers for the wind tunnel and field setups. While previous works have observed a filtering behavior in wind turbine power output, this exact behavior has not, to date, been properly characterized. Based on the spectral structure of the incoming flow turbulence at hub height, and the mechanical and structural properties of the turbines, a physical basis for the behavior of temporal power fluctuations and their spectral structure is found with potential applications in turbine control and numerical simulations. Consistent results are observed across the geometrical scales of the wind turbines investigated, suggesting no Reynolds number dependence in the tested range.

2.2 Introduction

In recent years, wind energy has increasingly become a mainstream form of electricity production in the United States. In 2012, wind accounted for approximately 4% of the total electricity production in the country, and led all other technologies for newly installed generation capacity [1]. However, as grid penetration increases, so does the need for improved behavioral understanding and predictions for proper management and optimization of this technology.

The understanding of wind turbine behavior over a broad band of turbulent scales is a critical component to the operation and maintenance of wind turbine and wind farms. Numerous efforts have been carried out to characterize wind turbine behavior at time scales ranging from several minutes to days, highly important for power system operations [97, 72] and for structural design considerations [67]. Cyclic motions on the order of seconds to minutes are a major contributor to dynamic loading on turbine blades and gearboxes [109]; however, characterizing turbine behavior as a result of very rapid and gradual changes in the velocity field is still an open problem involving complex flow-structure interactions.

The complex and unsteady behavior experienced by wind turbines is primarily modulated by the structure of the atmospheric boundary layer (ABL) turbulence [62] and the mechanical and structural properties of the turbines. Because energy is converted from the angular momentum of the rotor, and not directly from the wind, the power output and dynamic load responses are not linearly related to fluid power fluctuations, and are notably different across scales of motion [21]. The ABL turbulence exhibits characteristic features [112, 80] that can be used to gain insight into the flow-turbine interaction. For instance, a recent field study by Chamorro *et al* [21] showed the connection from the spectral distributions of the incoming flow to that of the power output and the stresses at the foundation for a full-scale wind turbine, and Sorensen *et al* [114] used the spectral structure of the turbulence to simulate the dynamic interaction between wind farms and power systems. However, much more detailed statistical information is necessary to characterize loads for wind turbines [87]. Improved understanding of the fluctuating behavior of wind turbines opens up the possibility of advanced strategies aimed to reduce dynamic loads[79, 18, 94] and to optimize the operation of wind farms, which are key and major contributor to the overall performance of the technology [10]. The use of incoming wind measurements to optimizing the turbine operation has attracted a large amount of interest from both academic and industrial researchers. Most of the research efforts have been motivated by recent developments in the LiDAR systems, which use the backscattering of light to measure atmospheric velocity. Wind velocity data from the LiDAR measurements, first used by Harris et al. [46] for improved load mitigation, has been proposed as a way to predict very short term fluctuations in turbine behavior (e.g., [82]). Recently, LiDAR measurements have been used to improve yaw alignment [68] and mitigate turbine structural damage [71]. Schlipf et al. [106] simulated a controller design implementing nonlinear predictions based on LiDAR measurements, and showed a possibility of up to 30 % reduction in lifetime fatigue loads. A thorough review of rotor control methods to reduce load reduction can be found in Barlas and van Kuik [6].

Advances in Large-Eddy Simulation (LES) for modeling wind turbines and wind farms have proven to be useful in the nuanced understanding of the way wind turbine wakes are shed and interact [16, 81]; high-fidelity parameterizations have shown some of the key features of turbine behavior [75, 96, 29, 116] and the effect of topological variables such the role of atmospheric stability and surface topography on wind turbine dynamics [31]. The current state of the art in the modeling of wind turbines, the actuator-line methods (ALM) of Sørensen and Shen [113] which introduces component lift and drag forces from turbine blades as body forces in the equations of motion, allows further improvements on the modeling including highly unsteady and turbulence-driven processes. However, advances in LES treatment of wind farms have yet to fully incorporate the effect of structural and mechanical components on turbine operation[56]. Even the most recent high-fidelity wind turbine computational simulations prescribe a fixed rotational velocity for the rotor, rather than accounting for its change in time [51]. Laboratory investigations have revealed key details of the turbulence and wind turbine/farm interactions. In particular, this includes turbulent flux of momentum into wind farms [15], topography [120] and turbine layout effects [27, 20], among others. However, few investigations have been made into the reaction of a turbine to the turbulence it experiences. Recent phenomenological results by Chamorro et al. [21] suggest that wind turbines can be modeled as a low-pass filter of the incoming turbulence for estimating the structure of the power output fluctuations. This observation opens new ways to address the turbulence modulation on cyclic loading and can lead to new strategies for reducing the effect of turbulence in the response and behavior of turbines.

In this work, we aim to contribute to the quantitative description of the behavior of wind turbine power output through a basic investigation of the energy balance of a wind turbine rotor. The simple physical basis introduced is tested on turbines of three vastly different sizes, demonstrating it is not scale dependent. In Section 2.3 we describe the experimental setup; while the analytical details of the turbine behavior are elaborated in Section 6.4. Remarks are summarized in Section 2.5.

2.3 Experimental set-up

High-resolution data of the power output and incoming flow turbulence to three horizontal-axis wind turbines of very different size and rated power were collected and used to probe the nature of power fluctuations of wind turbines and their spectral structure. The smallest turbine, hereon refereed as *miniature*, has a 0.12 m rotor diameter and was operated in a wind tunnel; the second turbine, referred as *small*, has a 3.2 m rotor diameter and was operated in an open field. We also used information from a full-scale wind turbine of 96 m rotor diameter. Details on this turbine and data can be found in Chamorro et al. [21]. The specific experimental setup for the miniature and small turbines is described as follows.

2.3.1 Miniature wind turbine

A horizontal-axis miniature wind turbine of $d_T = 0.12$ m rotor diameter, $P_{0,m} \approx$ 1 W rated power, and hub height $z_{hub} = 0.125$ m ($z_{hub}/d_T = 1.05$) was placed and tested in the Talbot Laboratory wind tunnel of the University of Illinois at Urbana-Champaign. The Eiffel-type wind tunnel has a test-section 0.914 m wide, 0.457 m high, and 6.1 m long (Figure 2.1 shows part of the test section pointing downwind). It was designed to have a ratio between the boundary-layer thickness on each sidewall less than 0.09. More details on the facility can be found in Adrian Adrian et al. [2]. The turbine's rotor is based on a reference model turbine by Sandia National Laboratory [107, 59], and the blades and nacelle were fabricated at the University of Illinois Rapid-Prototyping laboratory using an Objet Eden 350 machine and PolyJet Vero material. Details of the blade geometry along its span are included in Table 2.1. A Precision Microdrives 112-001 Micro Core 12 mm DC Motor is used as a loading system (generator). The angular velocity of the rotor (Ω) was controlled by the resistance of the generator, which was set to 2 ohms.

The mean incoming hub-height velocity was $U_{hub} = 6.5$ ms^{-1} during the experiment, giving a Reynolds number based on the rotor diameter of $Re_d = U_{hub}d_T/\nu = 5.5 \times 10^5$, where ν is the kinematic viscosity, and a tip-speed ratio $\lambda = \Omega d_T/(2U_{hub}) = 3.5$. During the testing, the miniature turbine operated with a power coefficient of $C_p = 0.11$.

The turbine was operated under free-shear flow in neutrally stratified conditions and nearly zero pressure-gradient, achieved via adjustment of the tunnel ceiling. Turbulence was generated with a passive turbulence-generator grate placed at the entrance of the test section, which produced a turbulence intensity at the turbine location of $I_u = \sigma_u/U_{hub} = 0.08$, where σ_u is the standard deviation of the streamwise velocity component. Wind measurements were performed at a height coincident with the turbine hub using a 5 μm hotwire anemometer controlled with a Dantec Dynamics system. Calibration of the probe was performed before the experimental run against a pitot-tube using six mean velocities in the vicinity of the mean flow conditions. Turbine power output was acquired with a Measurement Computing USB-1608HS datalogger and instantaneous voltage was measured directly from the terminals of the DC generator. Power was then inferred from instantaneous voltage and the resistance across the terminals of the datalogger. Both incoming flow turbulence and turbine power output were collected at a sampling frequency of f_s =5 kHz for a period of 240 s. A sample of the velocity and power output fluctuations of the miniature turbine is illustrated in Figures 2.2.a and 2.2.b.

2.3.2 Small wind turbine

A wind turbine of $d_T = 3.2$ m rotor diameter, rated power $P_{0,s} = 1$ kW and hub height $z_{hub} = 4$ m was placed in an open field with a mild adverse slope

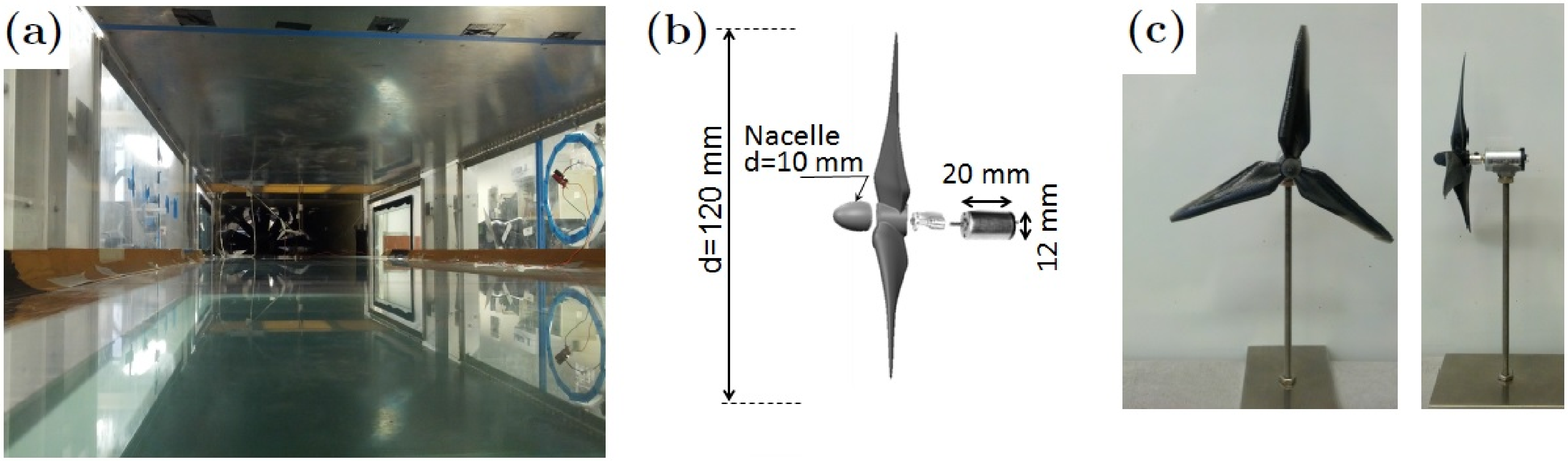

Figure 2.1: (a) Photograph of the Talbot Laboratory wind tunnel in the test section pointing downwind. (b) Schematic and (c) photographs of the miniature wind turbine.

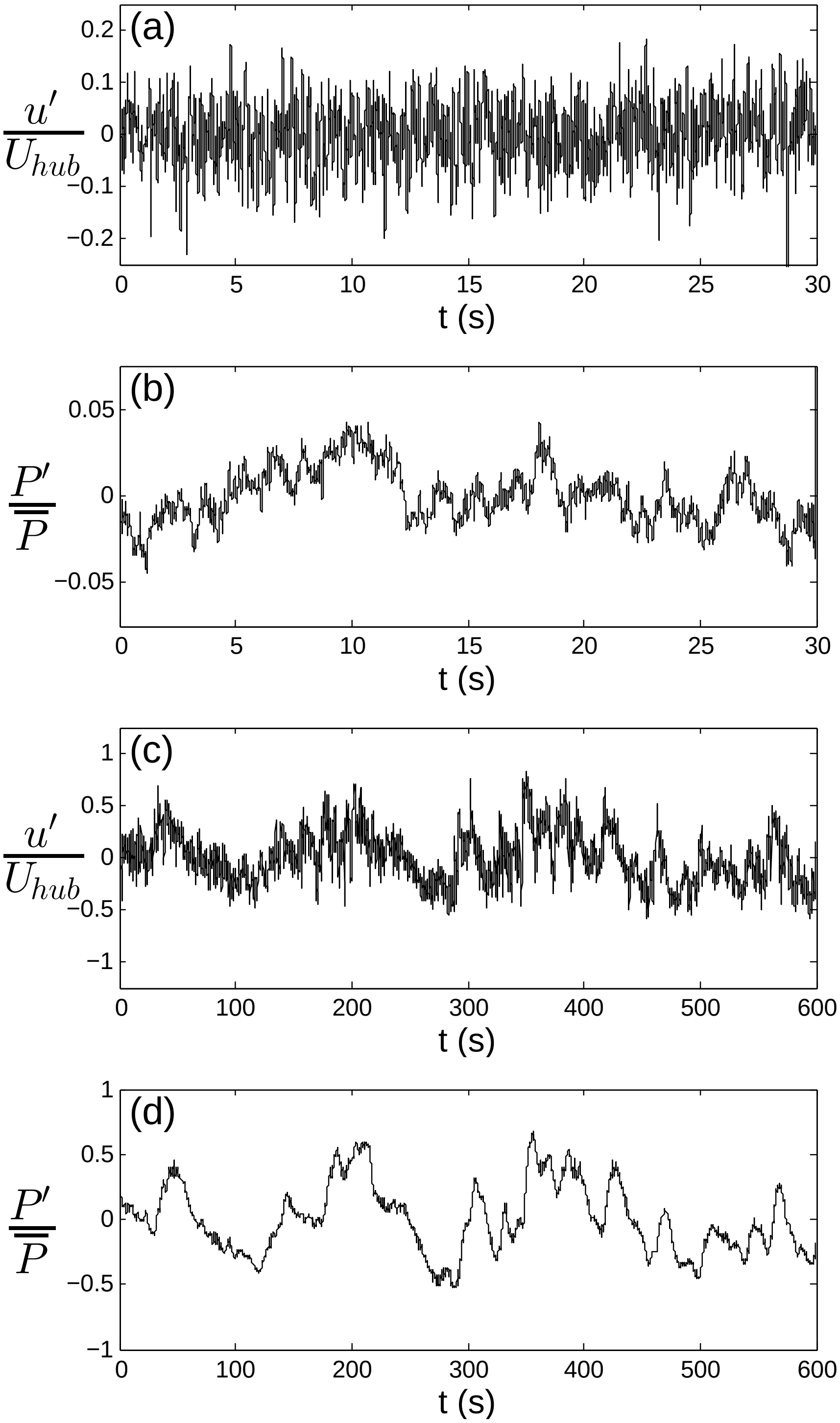

Figure 2.2: Sample velocity and power output fluctuations for the miniature (a,b) and small (c,d) wind turbines.

Table 2.1: Basic geometry of the blades of the miniature and small wind turbine normalized by the rotor radius: c is the chord length, (α) is the angle with respect to the rotor plane. R is the rotor radius

Small turbine

r/R	0.2	0.3	0.4	0.5	0.6	0.7	0.8	0.9	0.95
c/R	0.130	0.125	0.120	0.115	0.110	0.100	0.090	0.083	0.080
$\alpha(^o)$	8.4	7.5	6.5	5.6	4.6	3.7	2.7	1.8	1.3

Miniature turbine

r/R	0.2	0.3	0.4	0.5	0.6	0.7	0.8	0.9	0.95
$c/R)$	0.275	0.248	0.215	0.181	0.156	0.136	0.119	0.100	0.088
$\alpha(^o)$	31.8	23.9	17.7	12.8	9.4	7.5	6.0	4.6	3.9

and constant surface roughness (see photograph in Figure 2.3). The turbine was placed on a flat section of land immediately downstream of the sloped terrain so that near-ground flow acceleration would reverse the effects of shear. As a result, the rotor faced a roughly free-shear flow, as shown in Figure 2.4. The experiments were performed in the early afternoon, under approximately neutral thermal stratification as measured by the sonic anemometers and approximated by the time of day, with an air temperature of 14 ^{o}C. The turbine's hub height was set such that $z_{hub}/d_T = 1.25$, similar to the proportions of a utility-scale turbine. The angular velocity of the rotor was controlled by the resistance of the generator, which was set to 4 ohms. With this resistance, the resultant tip-speed ratio λ was 3.1 during the course of the experiment. The mean incoming hub-height velocity was 6.0 ms^{-1}, giving a Reynolds number $Re_d = 1.5 \times 10^7$. The generator produces three-phase AC power, which is then rectified to DC. During testing, the small turbine operated with a power coefficient of $C_p = 0.29$. The turbine's blades have a NACA 632-615 airfoil section; chord length and pitch along the blade span are described in Table 2.1. Lift and drag coefficients of the airfoil, using XFOIL simulations, for Reynolds numbers of $Re_d = 1.5 \times 10^7$ and 4.5×10^9, representing the case for the small turbine and of an equivalent turbine with 100 m rotor diameter are shown in Figure 2.5.

Incoming flow turbulence was characterized with an array of four Campbell Scientific CSAT3 sonic anemometers, which simultaneously measured the three velocity components of the flow at a frequency of 20 Hz. The anemometers were deployed in a vertical arrangement to sufficiently capture the characteristic behavior of the flow relevant to the turbine, approximately 3 meters away from the turbine tower in the plane of the rotor. One anemometer was placed at hub height, one half-way between the top tip and hub, one halfway between the bottom tip and hub, and the fourth was placed at the bottom blade tip. Figure 2.4 illustrates the mean velocity (U/U_{hub}), turbulence intensity and kinematic shear stress $(-\overline{u'w'}/U_{hub}^2)$ of the incoming flow at these four locations. For con-

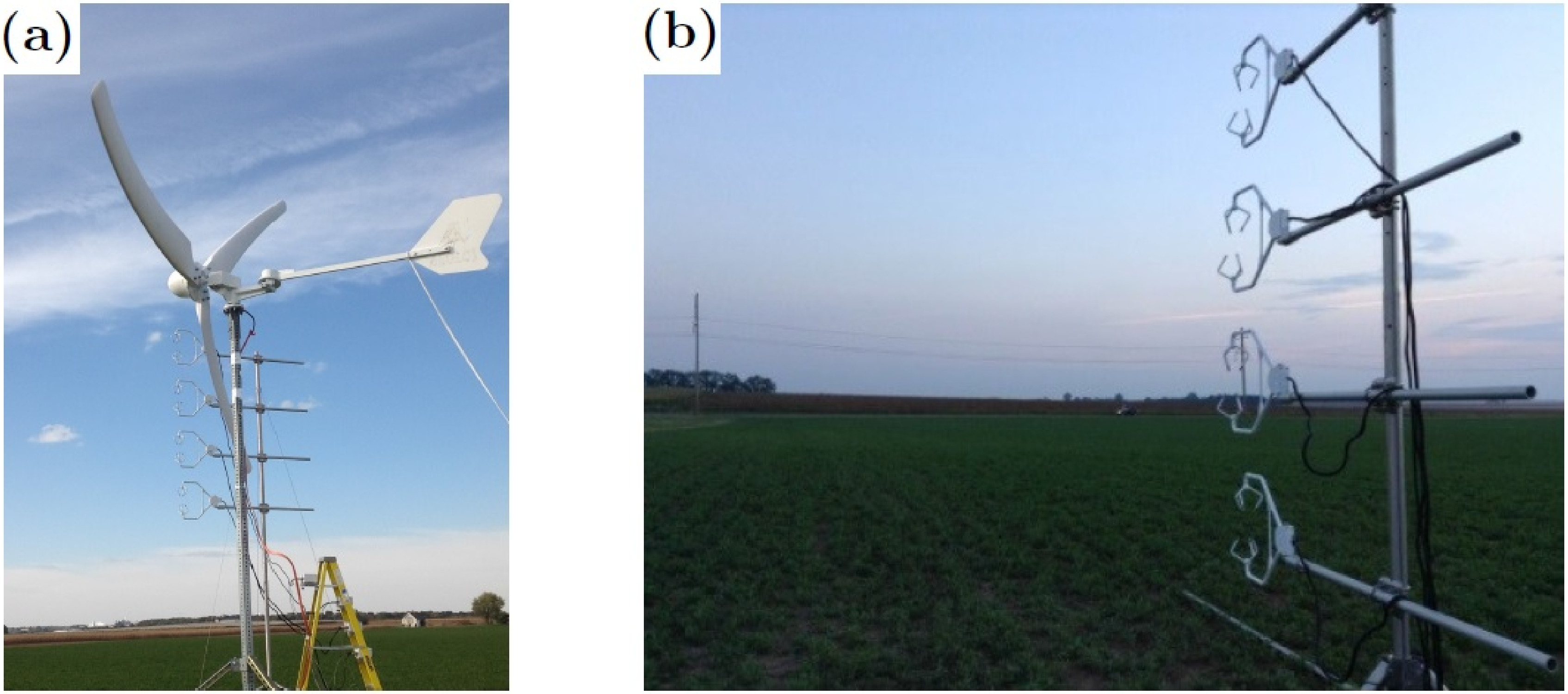

Figure 2.3: (a) Photograph of the small wind turbine and the array of CSAT3 sonic anemometers. (b) Close look of the array of sonic anemometers facing upwind.

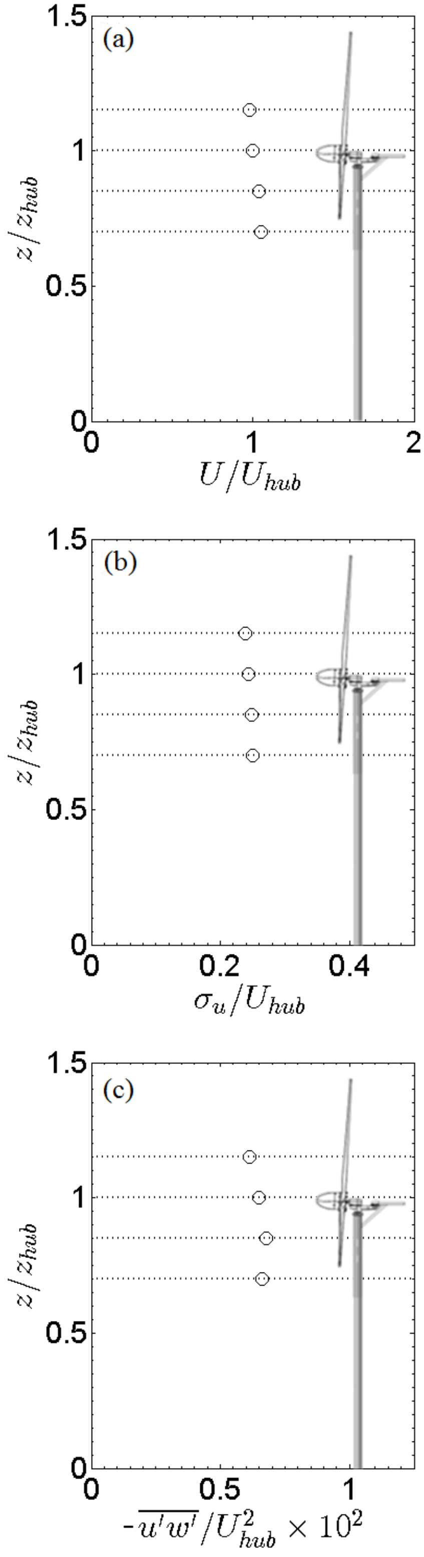

Figure 2.4: Incoming flow statistics normalized with the streamwise velocity at hub height. (a) Mean velocity. (b) Turbulence intensity. (c) Kinematic shear stress.

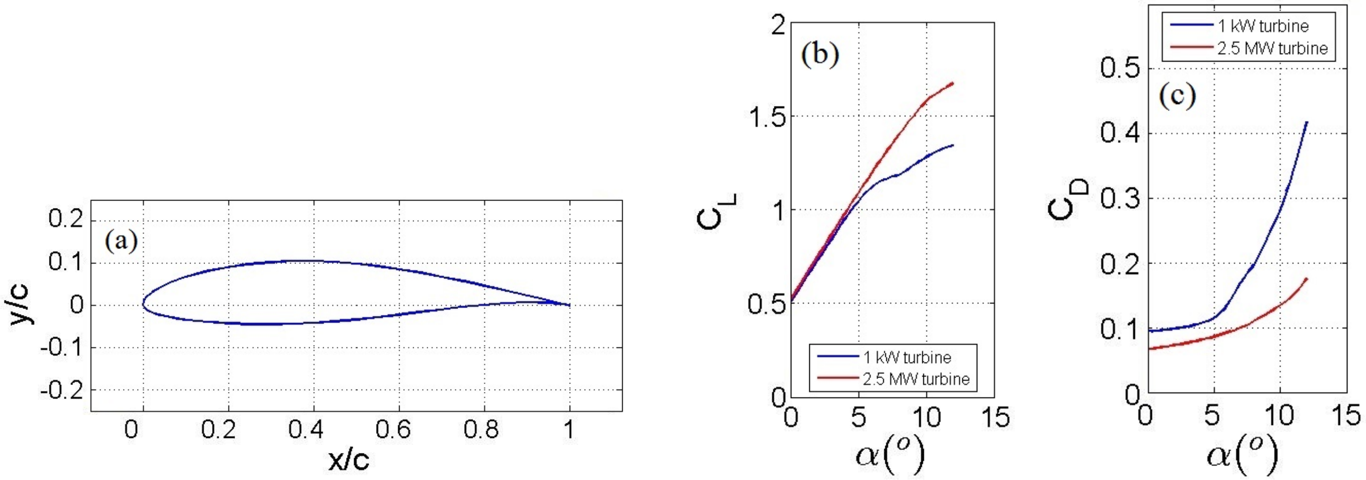

Figure 2.5: Left: (a) Schematic of the NACA 632-615 airfoil section. (b) Lift and (c) Drag coefficients of the blade airfoil section at Reynolds numbers of $Re_d = 1.5 \times 10^7$ and 4.5×10^9.

sistency with the other turbine cases, analysis is focused on hub-height velocity data. Data was recorded with a Campbell Scientific CR3000 datalogger. Voltage pulse data were taken from one of the three phases of the generator AC voltage to measure the turbine's rotational velocity, as the generator is fixed-gear. Instantaneous DC voltage was measured directly from the output of the rectifier. DC current was collected with an AcuAmp DCT100-42-24-F DC transducer. Measurements were taken over a 1 hour period, of which a subset of 10 minutes is analyzed for the current study. This sampling period was constrained to the field conditions during the experiment, including steadiness of wind direction and magnitude. A sample of the velocity and power output fluctuations of the small turbine is illustrated in Figure 2.2.

2.3.3 Full-scale wind turbine

To demonstrate a more complete picture of the flow-turbine power interaction, we also consider data reported from a previous investigation performed at the University of Minnesota Eolos Wind Energy Research Field Station. The facility consists of an instrumented Clipper Liberty 2.5 MW horizontal-axis wind turbine of 96 m rotor diameter and a 130 m meteorological tower, located 1.6 rotor diameters upstream of the turbine. Velocity was obtained from a sonic anemometer at hub height on the met tower, and power were collected for a period of 24 hours, one hour of which is analyzed in this study. During this time, the turbine operated with a power coefficient of $C_p = 0.49$. Details on the experimental data and facility can be found in Chamorro *et al* [21].

2.4 Analysis

In this section, we formulate a physical description of the power output fluctuations of wind turbines as a function of the structure of the incoming flow turbulence. Validation is performed with laboratory and field data from the three wind turbines described in the previous section. A conceptual schematic of the problem in consideration is illustrated in Figure 2.6.

2.4.1 Turbine power fluctuations

In working towards a solution to the problem, it is very effective to use the concept of signal filtering to model the turbine system response to incoming turbulence fluctuations. A recent study by Chamorro et al. [21] suggests that the power fluctuations are strongly modulated by the structure of the incoming flow in a complex manner; they identified three characteristic regions of the spectral domain with different behavioral responses to turbulence based on experimental results. In the first region, the turbine power output appears to be insensitive to flow scales smaller than the rotor diameter. In the second region, the turbine power and incoming flow show a non-linear interaction, while in the third region

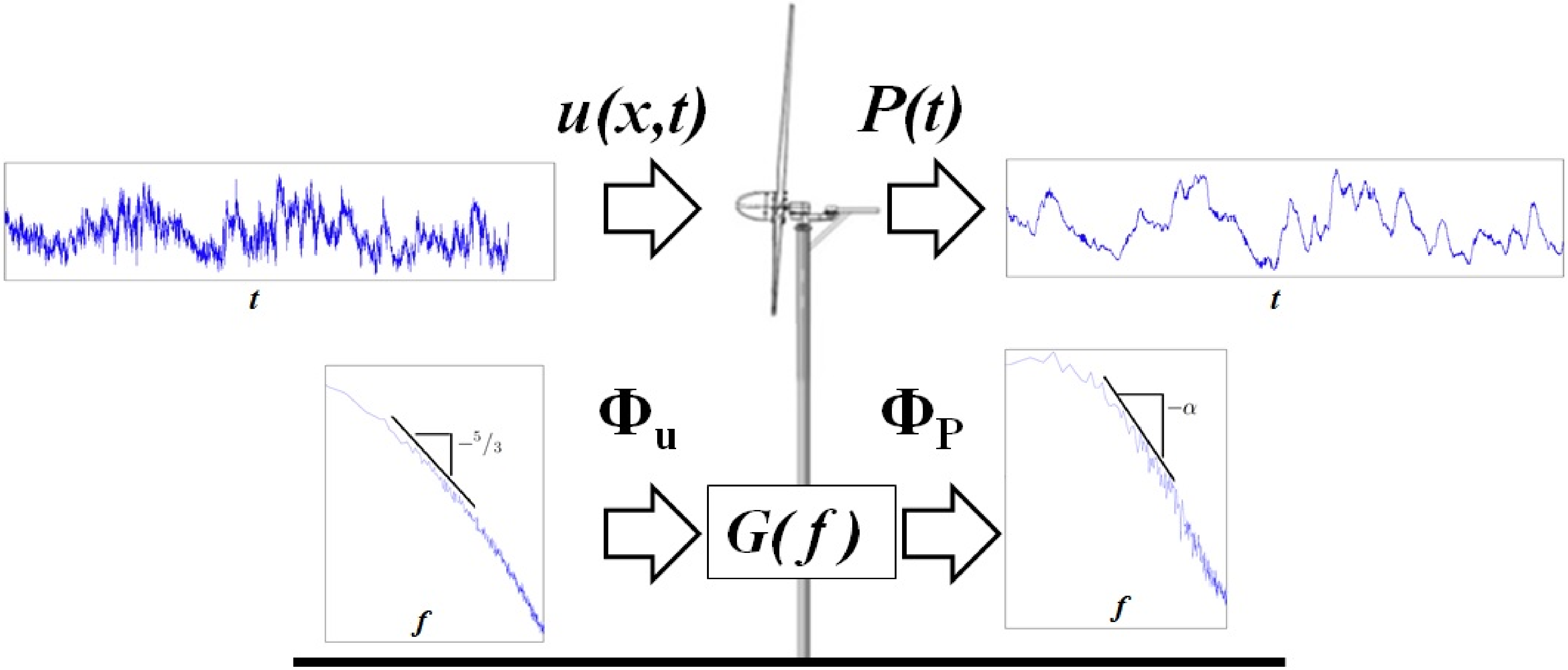

Figure 2.6: Conceptual schematic of turbine power response to incoming velocity via a transfer function

characterized by low wavenumbers, the turbine fluctuations appear to follow large scales of the flow. They observed a phenomenological relation between the power and velocity in the intermediate or second region of the spectral domain as:

$$\Phi_P(k) = G(k)\Phi_u(k) \tag{2.1}$$

where $G(k)$ represents a transfer function describing a power law in the wave number k in the 'inertial subrange' of the flow, of the form $G(k) \propto k^{-2}$. A similar power-law type of behavior of the power output of an entire wind farm was reported by Apt [3]. In these previous phenomenological works, there was no attempted analytical investigation of the underlying physical filtering process, which the current work seeks to do.

When constructing a thorough physical treatment of the problem, we can expect that within the intermediate range (or second region), both the structural characteristics of the turbine and flow define the power fluctuations. Taking these into consideration, we introduce a relation based on the impulse response of the turbine to fluctuations in wind power, which can be estimated from a basic energy balance of the wind/rotor/generator system. It may be assumed that the energy of the rotor enters strictly and instantaneously through the wind power via the wind turbine equation, and leaves the rotor through power produced by the generator. An energy balance of the system is shown in Equation 2.2,

$$\frac{dE_{rot}}{dt} = -P + 0.5C_p\rho A u^3(t) \tag{2.2}$$

where ρ is the air density, and A is the swept area of the turbine rotor. This can be converted into a differential equation for turbine power P by noting that $E_{rot} = 1/2I\omega^2$ and $P = \tau\omega$, where I is the rotor moment of inertia, ω is the rotational velocity in rad/s, and τ is electrical torque. This gives the relation $E_{rot} = \frac{PI\omega}{2\tau} = Pt_i$ where $t_i = \frac{I\omega}{2\tau}$, the inertial timescale, is a characteristic of the properties and operational status of the turbine. This leads to a nonhomogenous differential equation for $P(t)$ as given in Equation 2.3

$$\frac{dP}{dt} + \frac{1}{t_i}P = \frac{1}{t_i}0.5C_p\rho A u^3(t) \tag{2.3}$$

by assuming a first-order approximation that t_i takes its mean value at all points in time for a stationary flow. This nonhomogenous differential equation can be solved with a Green's function. Although the right-hand-side is a complicated, stochastic process, the left-hand side is a linear operator. As a result, the contributions to the turbine power from each previous point in time can be summed up with a weighting function of the form

$$G(t) = \Theta(t)e^{-\frac{t}{t_i}} \tag{2.4}$$

where $\Theta(t)$ is the Heaviside step function. The convolution of this Green's function with the right-hand-side gives the closed-form equation for power in time as shown in Equation 2.5.

$$P(t) = 0.5C_p\rho A t_i^{-1} \int_{-\infty}^{\infty} u^3(t-t')\Theta(t')e^{-\frac{t'}{t_i}}dt' \tag{2.5}$$

The convolution of the wind power equation with the impulse response function (or Green's function) bares a structural similarity with the transfer function concept proposed by Chamorro et al. [21], through the spectral domain transformation of the convolution theorem. Because the power spectrum of $u^3(t)$ will also implicitly contain the classical Kolmogorov $f^{-5/3}$ spectrum, it should be expected that the power spectrum of the impulse response shares some similarities to the previous observations. Certain similarities are present and will be illustrated below. The Fourier transform of the impulse response function is shown in Figure 2.7. The Fourier transform and power spectrum of the impulse response take the following forms.

$$\mathcal{F}\left(\Theta(t)e^{-t/t_i}\right) = \frac{1}{\sqrt{2\pi}}\left[\frac{it_i}{ft_i+i}\right] \tag{2.6}$$

$$|\mathcal{F}\left(\Theta(t)e^{-t/t_i}\right)|^2 = \frac{1}{2\pi}\left[\frac{t_i^2}{1+f^2t_i^2}\right] \tag{2.7}$$

As $f \rightarrow 0$ in Equation 2.7, it is easily seen that the transfer function will approach a constant value of $t_i^2/2\pi$. Such a flat response at low frequencies is consistent with the earlier observation where Φ_P appears to be proportional to Φ_u. As f becomes large, it is equally clear that the transfer function will approach the previously observed f^{-2} behavior.

2.4.2 Evaluation of Results

The analytic filtering behavior is investigated for the *miniature* 1 W (laboratory) and *small* 1 kW (field) wind turbines as well as in a 2.5 MW wind turbine (documented in Chamorro et al. [21]), where Reynolds numbers are $Re_d = 5.5 \times 10^5$, 1.5×10^7, and 4.5×10^8, respectively. Measured power output spectra from the three turbines are compared with the modeled spectra in Figure 2.8, which uses the velocity time series measured during each experiment. The abscissa of the figures is normalized with the turbine diameter and the incoming flow velocity at hub height for each case, but the ordinate is left purposely dimensional to highlight the several order of magnitude differences on the spectral distribution of the power in the three cases. Both power and velocity data are low-pass filtered in all three cases - the full-scale turbine at 0.2 Hz, the small turbine at 1 Hz, and the miniature turbine at 20 Hz. This filtered data also eliminate turbulent scales much smaller than the turbine rotor, which do not have effect on the power.

As illustrated in the figure, the modeled spectra show robust performance

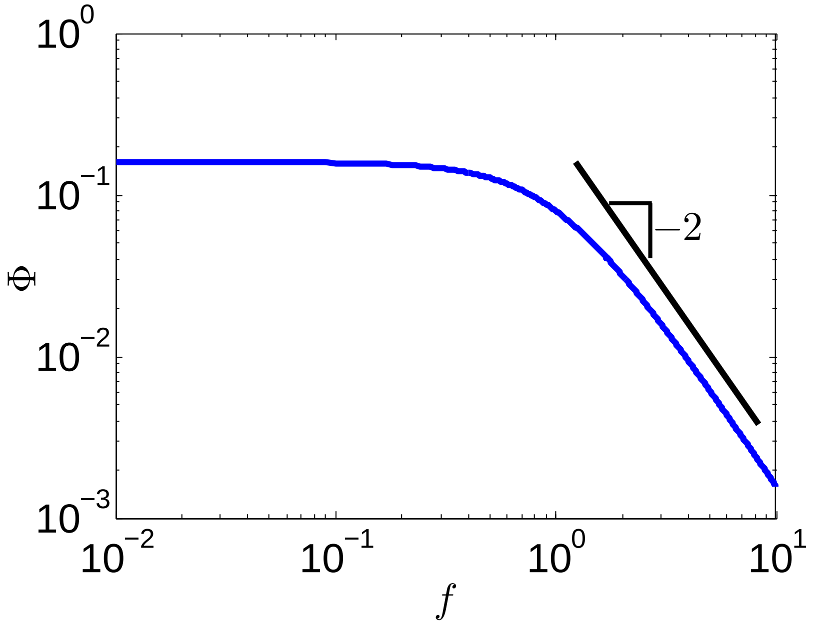

Figure 2.7: Fourier transform of impulse response function

across the turbine scales (rotor diameter from 0.12 m to 96 m) and turbine operation (tip speed ratio $\lambda \sim 3$ - 9). All necessary parameters for characteristic inertial timescale are directly inferred from measured data except for the moment of inertia. For the 2.5 MW turbine, the moment of inertia was estimated by the method of Rodríguez et al. [99], while it was measured directly for the miniature and small turbines. The spectral distribution of the measured power for the three cases also suggests that the power law decay proportional to the power $-5/3-2$ with frequency, i.e., $\Phi_P \propto f^{-5/3-2} = f^{-2}\Phi_u$, is a reasonable approximation across scales of the turbines and Reynolds numbers. It should be noted that the small and miniature turbine spectra exhibits some departure from the -5/3-2 shape. While the inertial time scale and the start of the turbulent inertial subrange line up well in the large turbine, this is not the case for the other two. This is simply a result of the scales involved in the three experiments, and is immaterial to the physics.

A good estimation of the temporal variation of the turbine power $P(t)$ from the streamwise velocity fluctuation $u(t)$ is also possible. Specifically, Equation 2.5 can be used with a velocity time series to estimate the instantaneous power output with high accuracy. The convolution of this real-space transfer function with the incoming fluctuating velocity time-series can also be seen as a near-term estimate of the fluctuating power when the velocity is obtained a certain distance (Δx) ahead of the turbine (see Simley et al. [110] on the topic of the frozen turbulence hypothesis for atmospheric LiDAR applications). The mean advection velocity is a good estimator for the phase drift, and is used as a lookahead time for the 96 m turbine ($t_{adv} \approx \Delta x / U_{hub}$ where t_{adv} is the mean advection time). As the velocity measurements for the small turbine were performed in the same cross-stream plane as the rotor, $t_{adv} = 0$ in that case. The results of this operation are shown in Figure 2.9 for the 3.2 and 96 m turbines (velocity and power measurements were not simultaneous in the 0.12 m case). The modeled power fluctuations are overlaid with actual power fluctuations in Figure 2.9. This Figure also includes a naive instantaneous power estimation using Equation 2.8, instantaneously applying the turbine power equation for every sampled velocity measurement. The latter is included merely to highlight the strong filtering effects on the velocity and the overreaction found if applied directly. Finally, in order to further demonstrate proper estimation of fluctuations, Table **??** shows the modeled and measured standard deviations for all three turbines.

$$P_i = \frac{1}{2} C_p \rho A u_i^3 \tag{2.8}$$

2.4.3 Discussion

Although the structure of the power output appears to have a characteristic feature, the interaction between flow and wind turbines involves many complex

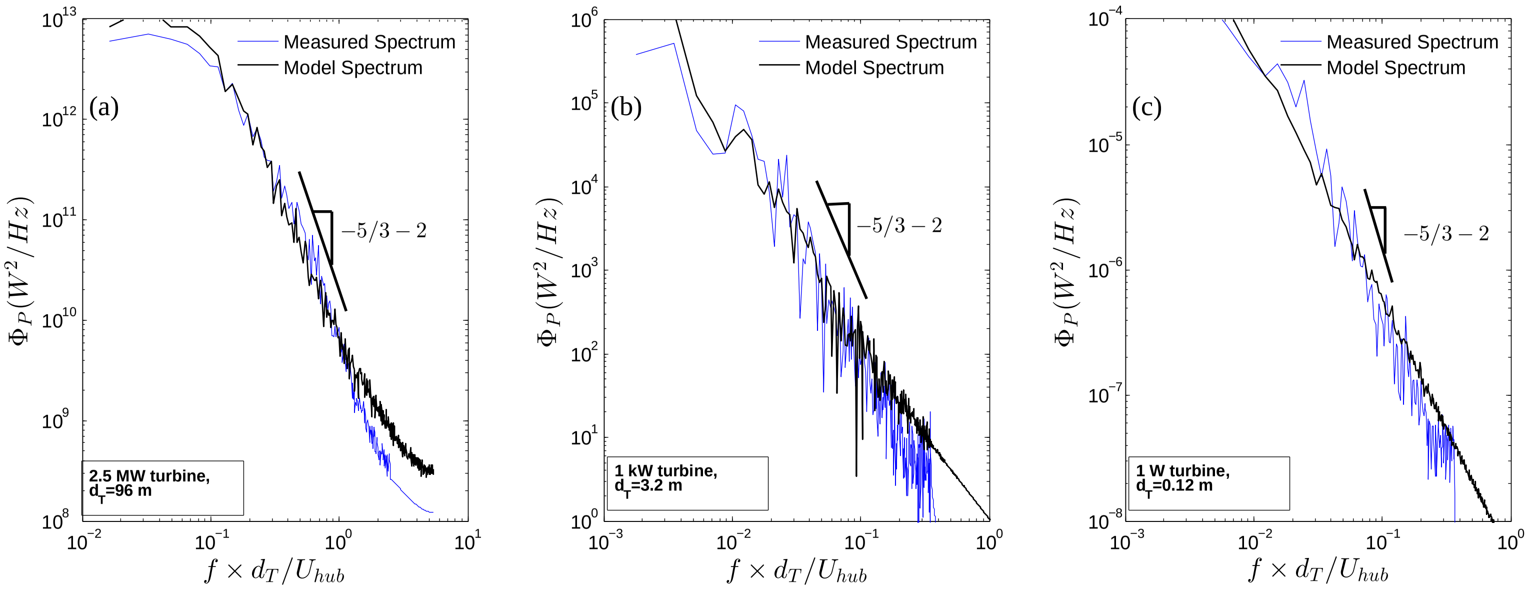

Figure 2.8: Measured and modeled power output spectra for the three turbines. (a) Full-scale. (b) Small. (c) Miniature.

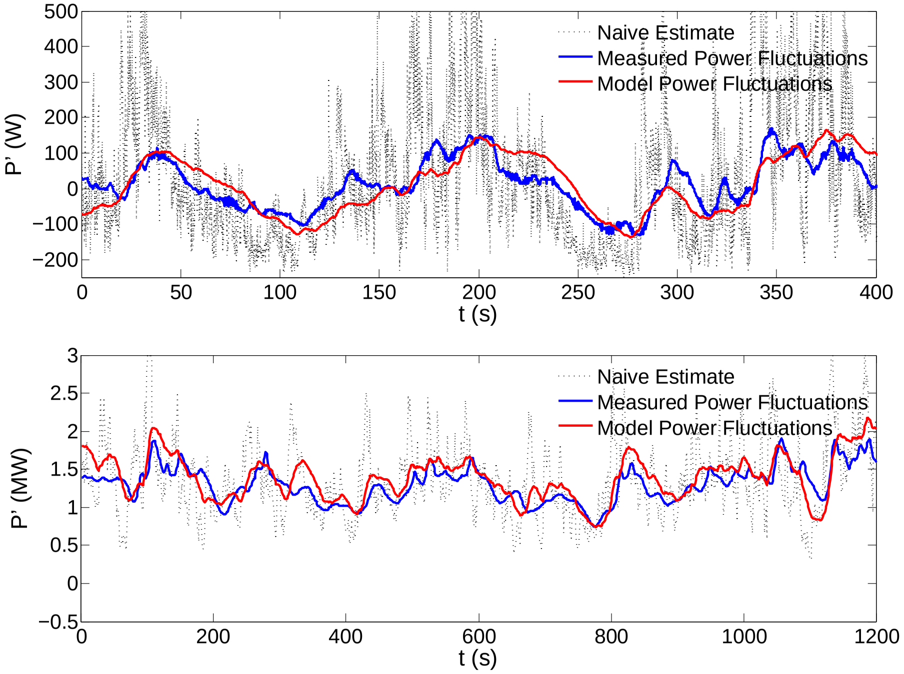

Figure 2.9: Measured and estimated real-time fluctuating power for the (a) full scale and (b) small wind turbines.

Table 2.2: Measured and estimated standard deviation of power fluctuations (σ_p) for the three turbines

σ_P	Miniature	Small	Full-scale
Measured (W)	7.8×10^{-2}	66	2.8×10^5
Modeled (W)	7.3×10^{-2}	89	2.9×10^5

processes. Intermittent gusts, rapid changes in the wind direction and passage of energetic flow structures are features of the ABL that can induce dynamic loads on individual wind turbines and blades [42, 36, 64]. Atmospheric stability is another important mechanism that modulates the dynamics of turbulence and, therefore the response and fatigue damage of wind turbines and farms (e.g., [104, 103]). In fact, Kelley [63] found a (critical) stability that maximizes blade fatigue of wind turbines within wind farms; however, statistical analysis performed by Nelson *et al* [89] found a small influence of atmospheric stability on fatigue and extreme loads in turbine blades. Dynamic stall triggered by turbulence flow patterns involves complex dynamics difficult to infer from a deterministic view. Albeit the importance of intermittent events, typically they are either completely ignored or highly underestimated. More robust models addressing these turbulence processes will provide major improvements towards the understanding of wind turbine behavior and will enable the development of advanced strategies. We believe that the simple physics presented in the current work should be able to accurately account for things such as atmospheric stability and intermittent gusts, as they would manifest themselves in velocity signals. Future efforts will be placed on testing these mentioned phenomena in improved parameterizations of turbine power and dynamic response.

While the relation proposed in this paper deviates from the $G(k)\Phi_u(k)$ formulation proposed by Chamorro et al. [21], an approximate result along those lines would help to provide information to be used in engineering applications. The spectrum of power may be estimated with a Butterworth filter acting on some model of Φ_u, for instance the von Kármán model [129]. The phenomenology of the filtering behavior of the turbine may be estimated by a Butterworth filter. This requires the estimation of two parameters: the cutoff frequency, and the forward gain. As seen in the preceding sections, the inverse of the inertial timescale is identically the cutoff frequency in the filtering behavior of the turbine. This simply leaves an estimation of the forward gain, or the response at zero frequency. A zero-frequency change is the same as a change in mean wind speed, so the forward gain can be estimated simply by taking the derivative of the turbine power equation with respect to velocity, as shown in Equation 2.9. This may be used in the absence of velocity time series data as an engineering approximation of power fluctuations. The approximate spectral relation is shown below in Equation 2.10.

$$G_0 = \frac{dP}{dU} = 3/2C_p\rho AU^2 \tag{2.9}$$

$$\Phi_P(f) = \frac{(3/2C_p\rho AU^2)^2}{\sqrt{1+(2ft_i)^4}} \frac{4\sigma_u^2 T}{(1+70.8(fT)^2)^{5/6}} \tag{2.10}$$

In Equation 2.10, T is the integral timescale, the first term is the Butterworth filter, and the second term is the von Kármán turbulence spectrum model. The results for the three cases tested in this research are shown in Figure 2.10.

2.5 Final Remarks

Building upon earlier and new experimental results, the present study further demonstrates that a wind turbine responds to a turbulent flow field in a complex way. Specifically, a turbine can be thought of as a low-pass filter, which dampens the effect of turbulence across scales in a characteristic fashion. Based on these observations, as well as a simple energy balance of the turbine rotor, we introduce a basis for the prediction of power output of wind turbines, which depends on the structure of the flow turbulence and mechanical and structural characteristics of a wind turbine. The framework allows for good estimates of power fluctuations by applying convolution of the incoming velocity and the impulse function, as well as accurate predictions in the power spectral domain. It has potential applications in both load mitigation of wind turbines, and higher-order accuracy in Large Eddy Simulation of wind turbines. In addition to the physically derived relation between wind power and electrical power, an engineering model is proposed based on a Butterworth filter which may be used to estimate power fluctuations at times when no time series information is available.

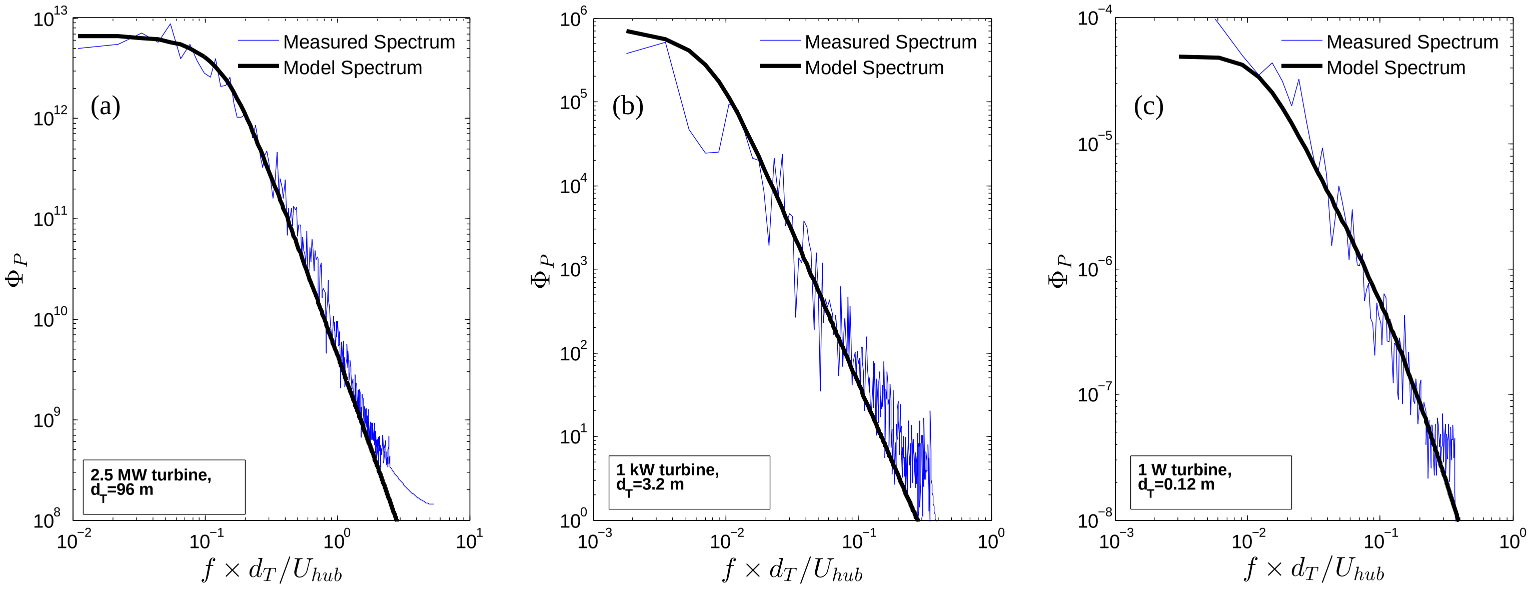

Figure 2.10: Model and measured power spectra of (a) 2.5 MW, (b) 1 kW and (c) 650 mW turbines

Chapter 3

Integrated Modeling of the Power Spectra of a Wind Farm

This work appears in the journal Physical Review E [77], and is copyrighted by The American Physical Society, which states that, "the author has the right to use the article or a portion of the article in a thesis or dissertation without requesting permission from APS, provided the bibliographic citation and the APS copyright credit line are given on the appropriate pages." Being author of this article, and having provided the bibliographic citation and acknowledged the American Physical Society as holder of the copyright of this work, I have fulfilled the requirements necessary to reprint this work. The majority of the analytical and the majority of the writing were done by Nicolas Tobin, but the experiments were performed by Huiwen Liu.

3.1 Abstract

The structure of the turbulence-driven power fluctuations in a wind farm is fundamentally described from basic concepts. A derived tuning-free model, supported with experiments, reveals the underlying spectral content of the power fluctuations of a wind farm. It contains two power-law trends and oscillations in the relatively low- and high-frequency ranges. The former is mostly due to the turbulent interaction between the flow and the turbine properties; whereas the latter is due to the advection between turbine pairs. The spectral wind-farm scale power fluctuations Φ_P exhibits a power-law decay proportional to $f^{-5/3-2}$ in the region corresponding to the turbulence inertial subrange and at relatively large scales, $\Phi_P \sim f^{-2}$. Due to the advection and turbulent diffusion of large-scale structures, a spectral oscillation exists with the product of a sinusoidal behavior and an exponential decay in the frequency domain.

3.2 Introduction

Wind is a mainstream source of electricity, and will play a leading role in achieving climate goals. Fundamental understanding on the relation between turbulence and wind turbines is key to improve reliability, predictability, and integration of wind farms into electrical grids.

Turbulence plays a dominant role in the structure of a wind farm's power output. In particular, turbulence intensity (I_u) is closely associated with power fluctuations [100], fatigue accumulation, [43] as well as forces and bending moments [126]. High turbulence can increase the mixing of wakes and thus alter the mean velocity and turbulence levels near downwind turbines [93]. Simple analytical models are widely used to characterize wakes, including mean velocity (e.g., [53, 9, 95, 28]) and I_u (e.g., [47, 134, 90, 45, 128, 115, 102]). Particular emphasis has been placed on the structure of the velocity fluctuations. Crespo and Herna [33] proposed a spectrum model for the evolution of wind-turbine wakes. Chamorro et al. [24] pointed out that wind turbines act as an 'active filter' of flow by modulating the large and small scales. Howard et al. [49] and Chamorro et al. [26] noted that the flow structures developing from upstream bluff bodies may leave strong signature on the fluctuations and spectrum of the power output of wind and hydrokinetic turbines. Recently, Jin et al. [58] showed the distinctive effect of background flow in the intermediate field and the increasing growth rate of the integral scale with turbulence.

Substantial effort has been placed on turbulence effects in wind farms. Sørensen et al. [114] proposed a model for the interaction between wind farms and power systems based on the turbulence spectrum. Milan et al. [83] suggested that for large time scales, the power fluctuations of wind farms can be considered to follow adiabatic wind dynamics with a similar $f^{-5/3}$ spectral behavior. However, recent work by Bandi [5] has shown that the effect of geographical smoothing on aggregate wind power outputs indicate an asymptotic limit of $f^{-7/3}$ for disperse wind farms. A similar observation was made by Apt for time scales ranging from 30 s to 2.6 days [3]. Chamorro et al. [21] showed three regions in the spectral domain defined by dynamical aspects of the flow and its interaction with the turbine. The power output appears insensitive to turbulence in the high-frequency region, where the turbulent scales are smaller than the rotor. In the intermediate region, with length scales up to those on the order of the atmospheric boundary layer thickness (ABL), the spectral content of the power fluctuations Φ_P and flow Φ_u exhibit a relationship characterized by a transfer function $G(f) \propto f^{-2}$. In the low-frequency range, very large-scale motions (with sizes on the order of the ABL and larger) directly impart their spectral characteristics onto the power output, and approach the $f^{-5/3}$ behavior observed by other authors. More recently, Tobin et al. [121] proposed a tuning-free model for $G(f)$ to predict power fluctuations of single turbines, which includes the modulation of the turbulence structure and the mechanical characteristics of the wind turbine. Mur-Amada and Bayod-Rújula [88] proposed that the sum of the frequency components of a single turbine approximates the wind farm output. However, it has since been observed that inter-turbine correlations have a marked effect on spectral structure, shown in field data by Calif et al. [17], the large-eddy simulations of Stevens and Meneveau [117]. and porous disk experiments by Bossuyt et al. [12].

Despite these efforts, a gap still remains in the quantitative description of the power fluctuations of wind farms as a function of the incoming turbulence, which is a building block for improving their efficiency and life span. This work aims to fill this gap by deriving wind-farm power fluctuations from first principles supported with experiments.

3.3 Experimental Setup

Wind tunnel experiments with two aligned wind farm models were performed to quantify the bulk power fluctuations and to test the developed model both for single turbine and wind-farm-scale power fluctuations. It is worth stressing that the model is scale-agnostic, and is able to predict the power structure of these model turbines and those at field scale 1 kW and 2.5 MW, as demonstrated by Tobin et al. [121].

Model wind farms were operated in the Talbot wind tunnel under nearly zero pressure gradient (fig. 3.1). The test section is 6.1 m long, 0.914 m wide, and 0.45 m high [2]. An active turbulence generator [58] created a realistic turbulent shear flow containing an inertial subrange spanning two decades. Roughness consisting of 5 mm chains every 0.2 m [91, 19] was also placed along the test section to develop a turbulent boundary layer (see Fig. 3.1b-c). The turbines are based on a reference model from Sandia National Laboratory [59, 108]. The rotors have a diameter $d_T = 120$ mm and hub height $z_{hub} = 125$ mm [124]. A Precision Micro-drives 112-001 Micro Core 12 mm was used as the loading system, with a rated power $P_0 \sim 1$ W. Additional characteristics quantities of the turbine can be found in Tobin et al. [122].

The distance Δ_x between turbines was $S_x = \Delta_x/d_T = 7$ and 10 in the flow direction, whereas both configurations has $S_y = \Delta_y/d_T = 2.5$ in the transverse direction. This resulted in 6×3 and 5×3 turbine arrays, where power measurements were performed on the central turbines. The experiments were conducted with an incoming hub-height velocity of $U_{hub} = 9.71$ ms^{-1} giving a Reynolds number $Re = U_{hub}d_T/\nu \approx 7.56 \times 10^4$. The turbines operated at a tip-speed ratio of $\lambda = \omega d_T/(2U_{hub}) \approx 4.9$, where ω is the angular velocity of the rotor. The measured power coefficient for the turbine is $C_p \approx 0.08$. This low value is due to the inefficiency of the generator (around ∼20% at the rotational speeds during the experiments) and not indicative of poor aerodynamic performance [59, 122]. The estimated thrust coefficient $C_T \approx 0.5$. The boundary layer had a thickness of $\delta/z_{hub} \approx 2.4$ and friction velocity $u_* \approx 0.46$ ms^{-1}.

Flow data were obtained from a high-resolution hotwire anemometer with the height adjusted by a bidirectional slide positioning system mounted at the top of the wind tunnel. The sensor voltage signatures were sampled at 10 kHz for a measurement period of 90 s when characterizing the boundary layer. Hotwire measurements were also taken in the upwind vicinity of each turbine to get the local incoming flow at a frequency of 20 kHz for a period of 120 s. A Measurement Computing USB-1608HS data acquisition system was connected to the generators to collect the instantaneous turbine voltages. Output power was measured at 100 kHz for a period of 120 s and inferred from the voltage and the terminal resistance (2Ω) of the generator.

3.4 Results and discussion

3.4.1 Power fluctuations of turbines in wind farms

To characterize the structure of the power fluctuations of wind farms, it is informative to first describe the fluctuations of individual turbines. Tobin et al. [121] proposed an analytical model that accounts for the underlying physical filtering process performed by a wind turbine in response to incoming turbulence. Based on the energy balance of the turbine's rotor,

$$dE_{rot}/dt = -P + 0.5 C_P \rho A u^3 \left(t\right) \tag{3.1}$$

where ρ is the air density, A is the swept area of the rotor, $E_{rot} = P t_i$ is the mechanical energy and P is the power. Here, $t_i = I\omega/2\tau$ is the inertial timescale that depends on the properties and operation of the turbine, I is the moment of inertia of the rotor and τ is the electric torque. To achieve maximum efficiency, $\tau \propto \omega^2$ is a standard control scheme used in variable speed wind turbines operating within region 2 [21, 32]. Here, a linearized relationship between τ and ω is used based on the assumption of small fluctuations respect to the mean rotational velocity. Solving equation 3.1 with a Green's function results in the following transfer function $\hat{G}\left(f\right)$ for Φ_P:

$$|\hat{G}\left(f\right)|^2 = {t_i}^2/[1 + 4\pi^2 f^2 {t_i}^2] \tag{3.2}$$

where $\Phi_P = \hat{G}(f)\Phi_u$, with Φ_u representing the velocity spectrum of the incoming flow. As $f \to 0$, $\hat{G}\left(f\right) \to {t_i}^2 = const$. This flat response at low frequencies is consistent with observations where Φ_P appears to be proportional to Φ_u. However, as f increases, $\hat{G}\left(f\right) \to f^{-2}$. A similar phenomenon occurs in the case of wind arrays, which is explored as follows.

The distributions of Φ_P, and Φ_u directly upwind of the rotors, for the central turbines at the 1st and 4th rows in the two setups is shown in Figure 3.2; the function $\hat{G}\left(f\right)$ is included as a reference. There, the peaks correspond to the turbine rotational frequency f_T and harmonics. The distinctive modulation of the flow structure and the turbine power via $\hat{G}(f)$ is made clear in this Figure. In particular, the power fluctuations of the turbines in the 4th row in the two setups also exhibit regions with spectral decay of f^{-2} and $f^{-2-5/3}$, but the location where they occur varies. Note that the beginning of the $f^{-2-5/3}$ region is shifted to a higher frequency in the 4th row. This is due to the difference in the wind farm layout, which modulates the structure and evolution of the turbulence inside the wind farm with respect to that of the incoming flow.

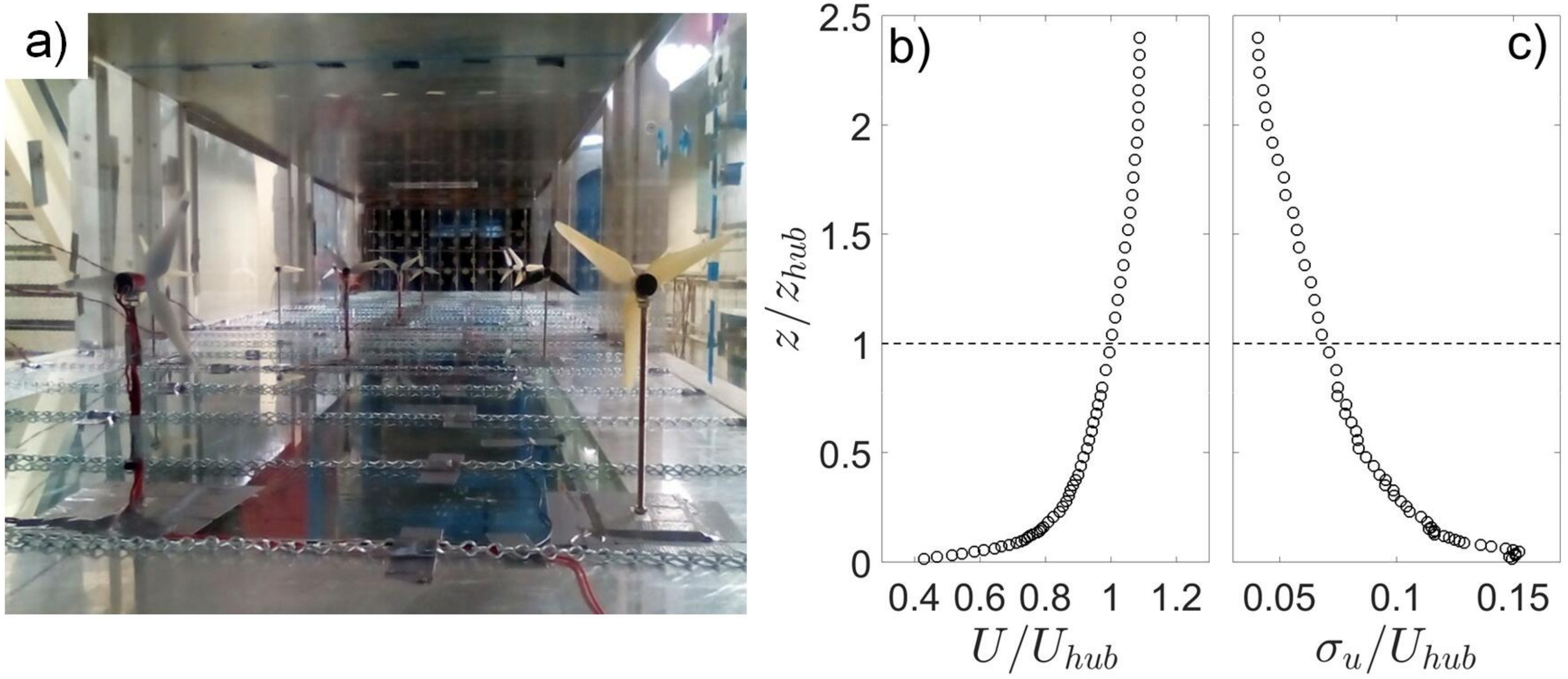

Figure 3.1: a) Photograph of the test section pointing upwind; b) Mean velocity U/U_{hub}; c) turbulence intensity $I_u = \sigma_u/U_{hub}$. Horizontal lines indicate the turbine-hub height.

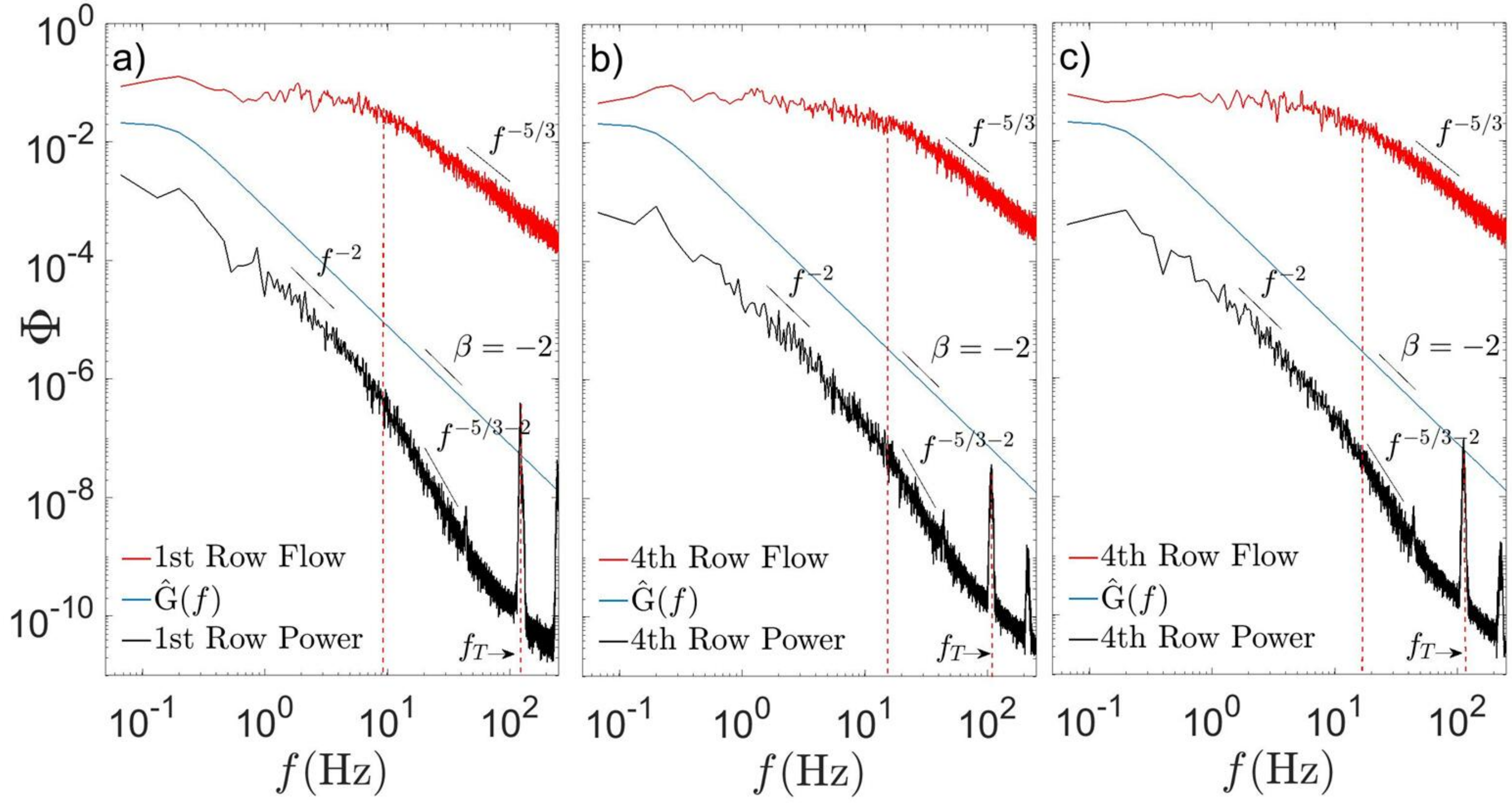

Figure 3.2: Spectra of incoming turbulence (*red*), $\hat{G}(f)$ (*blue*) and turbine output power (*black*) of a) 1st and b) 4th row, $S_x = 7$; c) 4th row, $S_x = 10$.

Further, the pre-multiplied spectra of the local incoming velocity $f\Phi_u$ and power output $f\Phi_P$ for the 1st, 2nd and 4th rows in the two setups are shown together in Figure 3.3. The representative turbulent scale of the incoming flow at hub height is larger than that of those within the wind farm due to the modulation of the wind turbines; this effect is reduced with increased turbine spacing. Compared with the inner rows, the power fluctuations of the 1st row are more energetic across all scales. The differences between the inner rows is much smaller, as flow velocity, I_u and integral length scale do not vary substantially.

3.4.2 Wind farm power fluctuations

Based on the features of Φ_P from single turbines within the wind farm, we model the power fluctuations in the ith row in the same way as the single turbine considering the local flow at hub height. Further, the local incoming Φ_u can be estimated with the von Kármán [129] model spectrum (Φ_u^K) using the local integral length scale (Λ^u) and velocity variance (σ_u^2), as follows:

$$f\Phi_u^K(f)/\sigma_u^2 = 4n_u/(1+70.8{n_u}^2)^{5/6} \tag{3.3}$$

where $n_u = f\Lambda^u/U$. In this context, Λ^u and U are representative of the incoming local flow (i-th row) at hub height. This procedure is shown in Figure 3.4 for the turbines in the 4th and 5th rows of the S_x=7 and 10. This suggests that Φ_u^K for the local velocity is able to properly infer the local Φ_u.

Using field measurements, Morfiadakis [86] proposed that Φ_u^K is suitable for canonical boundary layers. According to Figure 3.4, the local velocity spectrum at hub height appears to be well modeled by Φ_u^K. This suggests that it is appropriate in regions where tip vortices have no strong effect on the flow [22]. Appropriate estimation for Λ^u, U and σ_u^2 is key to allowing for the use of Φ_u^K. Like the case of a single turbine [121], the filtering effect of the turbine on the power output is estimated with a second-order Butterworth filter; the cutoff frequency is the inverse of the inertial timescale, and the forward gain can be estimated by taking the velocity derivative of the turbine power equation. The resulting spectral relation is then:

$$\Phi_P(f) = \frac{3/2C_P\rho AU^2}{\sqrt{1+(2\pi t_i)^4}} \frac{4\sigma_u^2T^u}{\left(1+70.8\,(fT^u)^2\right)^{5/6}} \tag{3.4}$$

A comparison between the modeled and measured power output spectra of selected wind turbines in the 4th and 5th rows of the two layouts is given in Figure 3.4. The modeled spectra show remarkable agreement with the power measurements and motivate the use for the collective Φ_P at wind-farm scale. Note that the spectral distribution for the two configurations clearly shows the $f^{-5/3-2}$ and f^{-2} power law decays. To assess the bulk performance of the model, a comparison between measured and modeled power variance σ_P^2 is shown in Figure

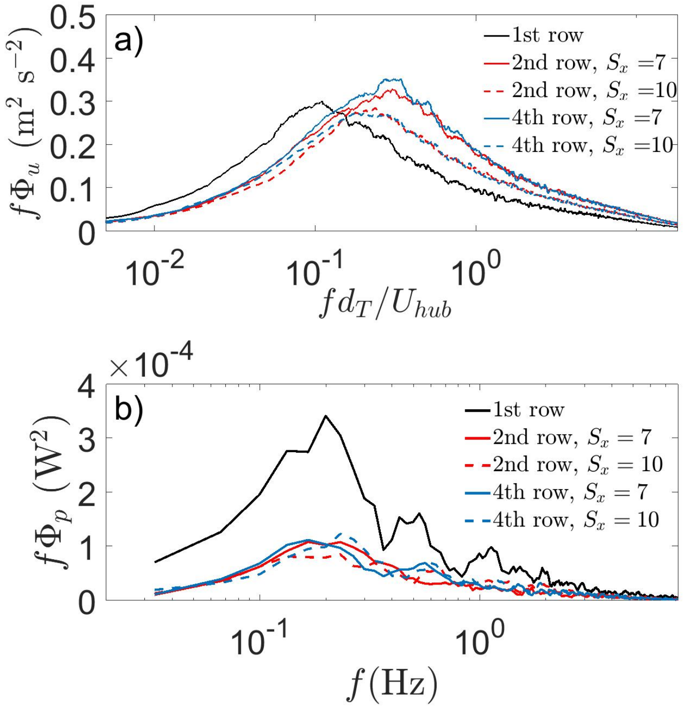

Figure 3.3: Pre-multiplied power spectra of a) the local incoming velocity and b) the power output of the 1st, 2nd and 4th rows with $S_x = 7$ and 10 (solid and dotted lines).

3.5. Note that the model only considers hub-height velocity.

3.4.3 Wind-farm power from global incoming flow

Usually, information on the incoming flow at each turbine is fairly limited. However, velocity data from the global incoming flow is likely available. Therefore, estimating the wind-farm power fluctuations with single-point measurements, namely the incoming flow at hub height of the first turbine, is very useful. Analytical models have been proposed to estimate wake flow in single turbines (e.g., [53, 44, 7, 9]) and within wind farms (e.g., [101, 34, 130]). Another key factor is I_u; various formulations exists for single turbine wakes [98, 47, 74, 33, 28] and within wind farms e.g., [43, 90]. A comparison of the mean flow and I_u for various models with the measurements is shown in figure 3.6.

It is possible to assume minor variations past 2-3 rows of turbines for practical purposes. Then, we can use the formulations for U and I_u to account for the local incoming flow. Here, we use the model by Voutsinas [130] with wake velocity models to simulate the velocity distribution inside the two model wind farms. The velocity model by Barthelmie [7] and I_u model of Quarton [98] are used to estimate the input parameters for the power fluctuations. Limited literature exists for Λ^u in turbine wakes or inside of wind farms. Experiments by Chamorro et al. [25] were found to fit well in the wind tunnel measurements by Jin et al. [58]. Hereon, despite some deviations with our measurements, the evolution curve from these sources was used for Λ^u.

3.4.4 Covariance due to advection and turbulent diffusion

Because nearby turbines simultaneously respond to large-scale atmospheric motions, the covariance of turbine pairs needs to be considered when predicting the total variance, as indicated in Equation 3.5.

$$\sigma^2\left(\sum_{i=1}^{N} P_i\right) = \sum_{i=1}^{N} \sigma^2_{P_i} + 2\sum_{i=1}^{N}\sum_{j>i}^{N} Cov\left(P_i, P_j\right) \tag{3.5}$$

The effect of covariance between turbine pairs inside of a wind farm is inspected with experiments by measuring the instantaneous power of the turbines both synchronously and asynchronously. As illustrated in the (sub-)Figure 3.7, covariance between turbines has a notable effect on the spectrum across scales. The first significant difference is in the low-frequency region, where neglecting covariance conspicuously under-predicts the spectral density. This is attributed to the fact that eddies with scales much larger than the separation between turbines modulate all their behaviors simultaneously. Furthermore, it is noted that significant bumps (oscillations) occur in the frequency region on the order of U/S_x and its harmonics. As anticipated, the frequencies where the bumps

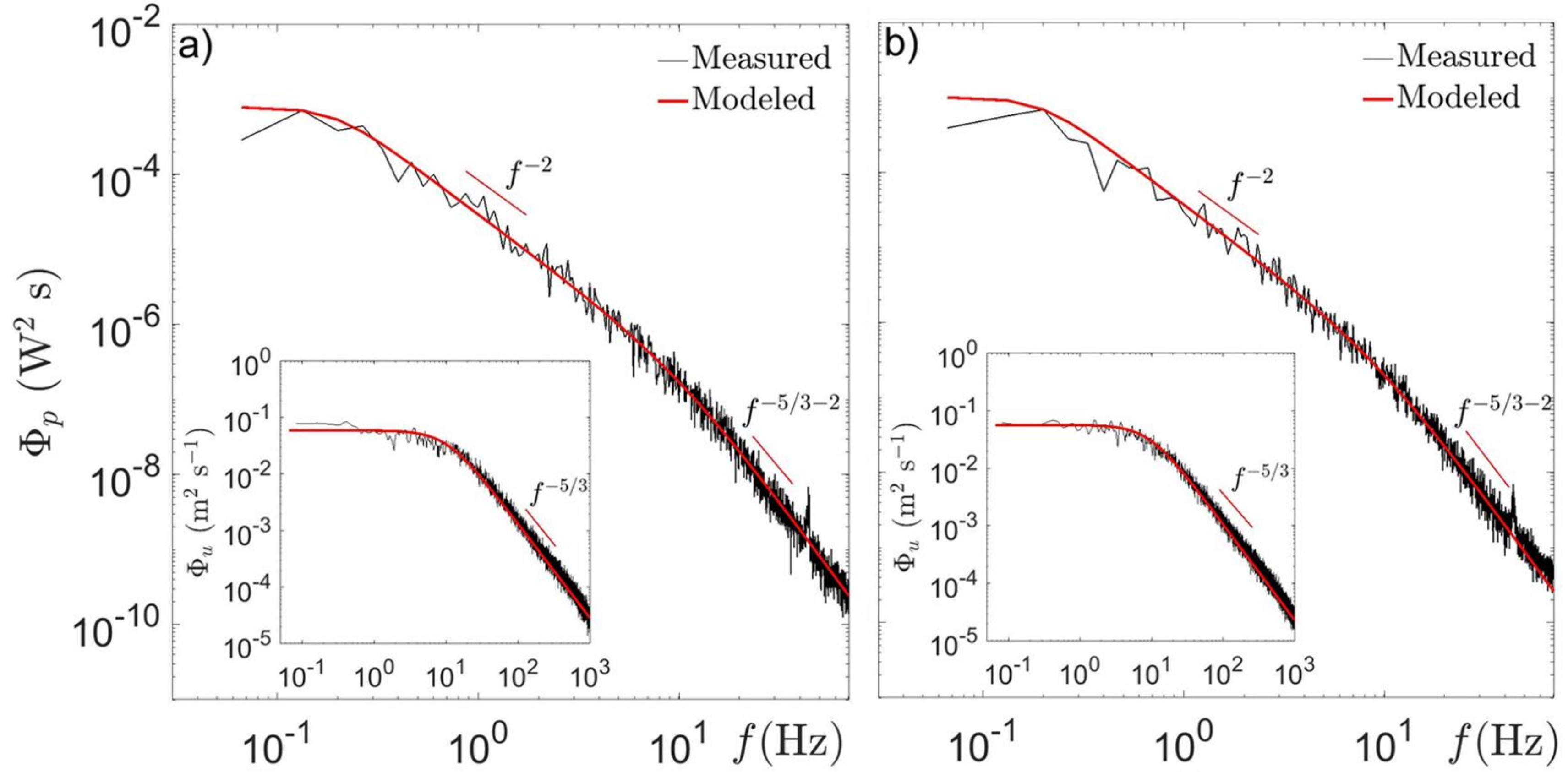

Figure 3.4: Measured and modeled spectra of hub-height velocity of incoming flow (sub-figures) and output power inside wind farm. a) 5th row, $S_x = 7$; b) 4th row, $S_x = 10$.

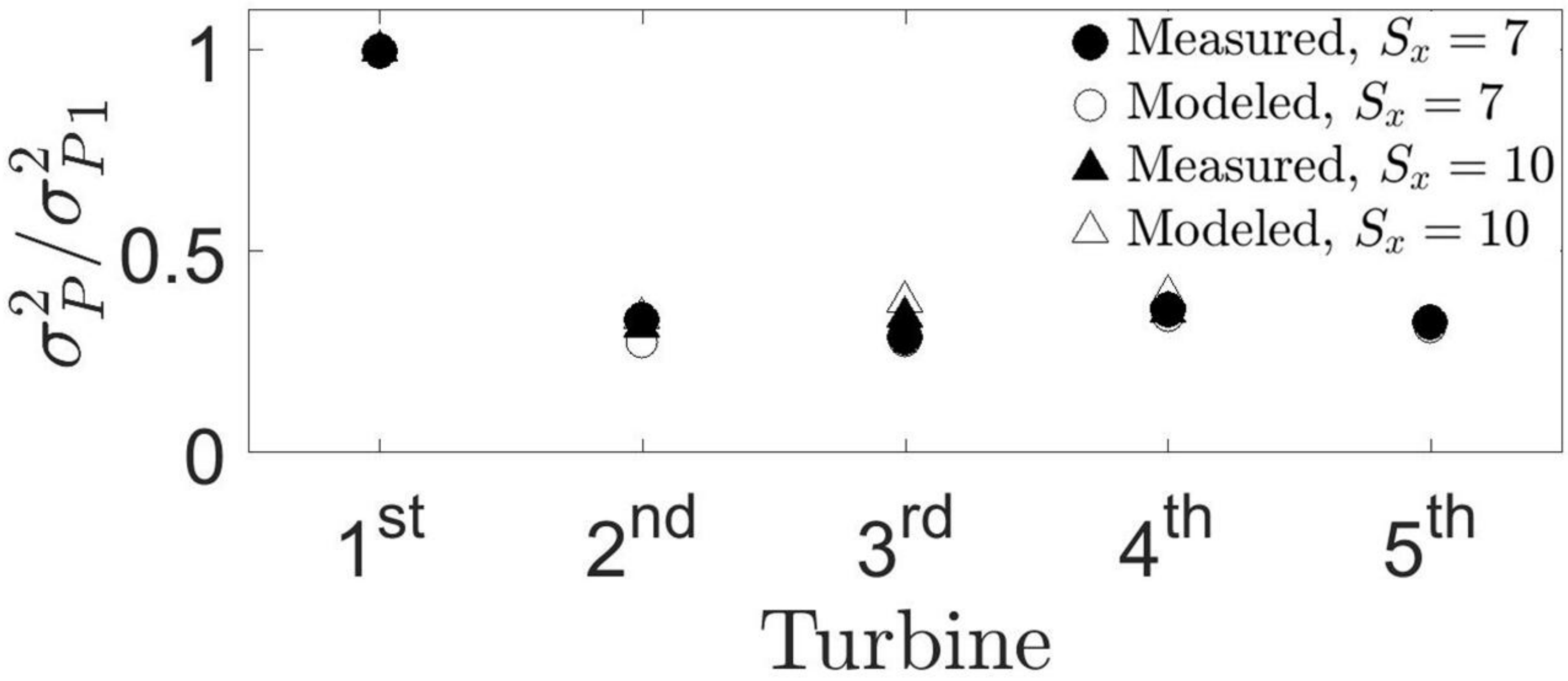

Figure 3.5: Measured and modeled power variance of individual turbines in the wind farm with $S_x = 7$ (o) and $S_x = 10$ ($\triangle$).

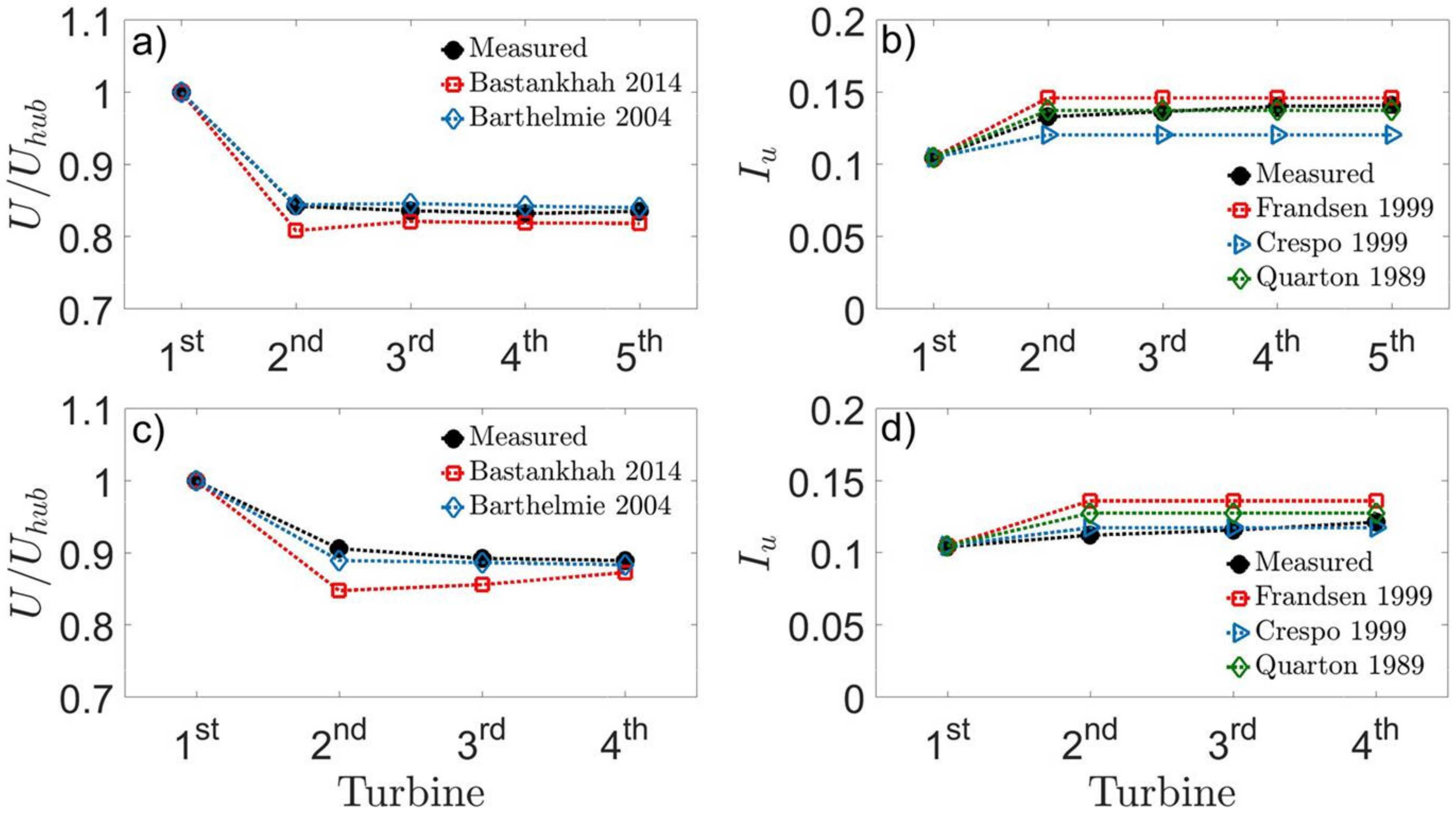

Figure 3.6: a) Mean velocity (U/U_{hub}) and b) turbulence intensity I_u within the $S_x = 7$, c) Mean velocity (U/U_{hub}) and d) turbulence intensity I_u within the $S_x = 10$ model wind farm at hub height.

occur in $S_x = 7$ case are larger than those of the $S_x = 10$ case correspondingly as the advection time between turbines is shorter. These bumps are attributed to motions that impart their signature on an upwind turbine, are advected downwind, and then impart their signature on a downwind turbine a short time later, leading to a periodic output. Although this leads to bumps at the advection time scale and its harmonics, the higher-frequency bumps are relatively weaker, likely due to turbulent decoherence of the small-scale structures.

To predict the power fluctuations with only incoming flow, it is necessary to estimate the covariance based on physical principles. Similar to Equation 3.5, the power spectrum of the wind farm must include a contribution of twice the co-spectrum of turbine pairs. The co-spectrum is the real part of the Fourier transform ($\mathcal{F}$) of the cross-correlation of the two power signals. The autocorrelation of the combined signal consists of the cross-correlation of the 1st signal with the 2nd, and of the 2nd signal with the 1st. The $\mathcal{F}$s of these signals are complex conjugates, which justifies taking the cross-correlation contribution as twice the real part of the $\mathcal{F}$.

Based on Taylor's frozen-eddy hypothesis [118] and Kraichnan's idealized random sweeping hypothesis [70], Wilczek and Narita [131] proposed a model to predict the two-time wavenumber co-spectrum of a laterally homogeneous turbulent shear flow. According to this model, the two-time co-spectrum is closely related to the instantaneous energy spectrum. Because power output fluctuations are driven by the turbulence, it is reasonable to connect the cross-correlation of the output power to that of the flow. The random sweeping hypothesis states that a frozen turbulence field is advected by the velocity $U+v'$, as given in Equation 3.6, where v' is referred to as the sweeping velocity.

$$\frac{\partial u(x,t)}{\partial t} + (U + v')\frac{\partial u(x,t)}{\partial x} = 0 \tag{3.6}$$

Considering two spatially separated points x_1 and x_2, taking the $\mathcal{F}$ of equation 3.6 and solving for the velocity $\hat{u} = \mathcal{F}(u)$, the following result is obtained:

$$\hat{u}(x_2, f) = \langle \exp\left(\frac{-2\pi i f \Delta x}{U + v'}\right)\rangle \hat{u}(x_1, f), \tag{3.7}$$

where $\langle\rangle$ denotes temporal averaging and $\Delta x = x_2$-x_1.

By assuming that the sweeping velocity v' is much smaller than the advection velocity, a similar approach to Wilczek and Narita is taken to model the two-point frequency spectrum. This leads to a complex exponential behavior in the co-spectrum due to advection and turbulent decoherence. By assuming a Gaussian probability density function for v', the following result can be obtained for the co-spectrum:

$$\phi_{1,2} = \phi_{1,1}(f)\exp\left(\frac{-2\pi i f \Delta x}{U}\right) \times \exp\left(\frac{-2\pi^2 f^2 \Delta x^2 \langle v' \rangle^2}{3U^4}\right) \tag{3.8}$$

where $\phi_{1,2}$ is the cross-spectrum of points x_1 and x_2, and $\phi_{1,1}$ is the power spectrum at location x_1. Because only the real part is taken, the complex exponential is reduced to a cosine contribution. We will further assume that $\langle v' \rangle^2 = \sigma_u^2$. Thus, assuming power is nearly uncorrelated between columns in the aligned layout wind farm, which is consistent with results of Stevens and Meneveau [117] and Bossuyt et al. [12], we derive the spectral form of the power output of an entire wind farm in the frequency domain as follows:

$$\Phi_{p_{wf}} = M\sum_{i=1}^{N}\Phi_{p_i} + 2M\sum_{i=1}^{N}\sum_{j>i}^{N}\Phi_{p_j} cos\left(2\pi f\tau_{ij}\right) \times \exp\left(-\frac{2}{3}\pi^2 f^2 {\tau_{ij}}^2 {I_j}^2\right) \quad (3.9)$$

where M and N are the number of columns in the transverse and streamwise directions. The co-spectrum of turbine pairs exhibits the product of a harmonic oscillation $cos\left(\pi f\tau_{ij}\right)$, and an exponential decay $exp(-\frac{2}{3}\pi^2 f^2 {\tau_{ij}}^2 {I_j}^2)$. The cosine portion of this formulation is from pure advection of frozen turbulence from one point upwind to another downwind. The exponential decay accounts for the fact that the turbulence is not perfectly advected, and becomes distorted as it move downwind, particularly so for high-frequency motions. Here, $\tau_{ij} = (j-i)S_x d_T/U_j$ represents the advection time between turbines i and j, and I_j denotes the local I_u of turbine j. Thus, Φ_{p_1} is the power spectrum of the first row and is calculated with Equation from [7] with incoming flow as input. The power spectra of turbine i (> 1) inside the wind farm, Φ_{p_i}, is calculated with the modeled parameters as input.

The predicted power output spectra of the two layouts is shown in Figure 3.7, with only incoming flow as input to Equation 3.9. In general, the formulation shows a good fit with measurements; the location and approximate magnitude of the bumps are also well predicted. The model does a comparatively poorer job of predicting low-frequency spectral densities. This may be due to the lack of good methods for estimating Λ^u and the assumption of laterally homogeneous flow in the sweeping hypothesis. Further, there is inherently greater uncertainty in low-frequency spectral density measurements, which can only be alleviated with greater measurement time. It should be noted that this formulation does not account for important dynamical occurrences in the wind-farm flow, such as wake meandering [50, 41].

3.5 Summary

This framework aims to fill outstanding gaps in the quantification of wind farm power fluctuations. With only the global incoming flow at hub height, the model is able to estimate the structure of the power fluctuations including range and level of characteristic regions as well as spectral oscillation. For a single turbine configuration, the spectral characteristics of the power fluctuation is determined via the incoming turbulence and transfer function. Spatio-temporal correlations

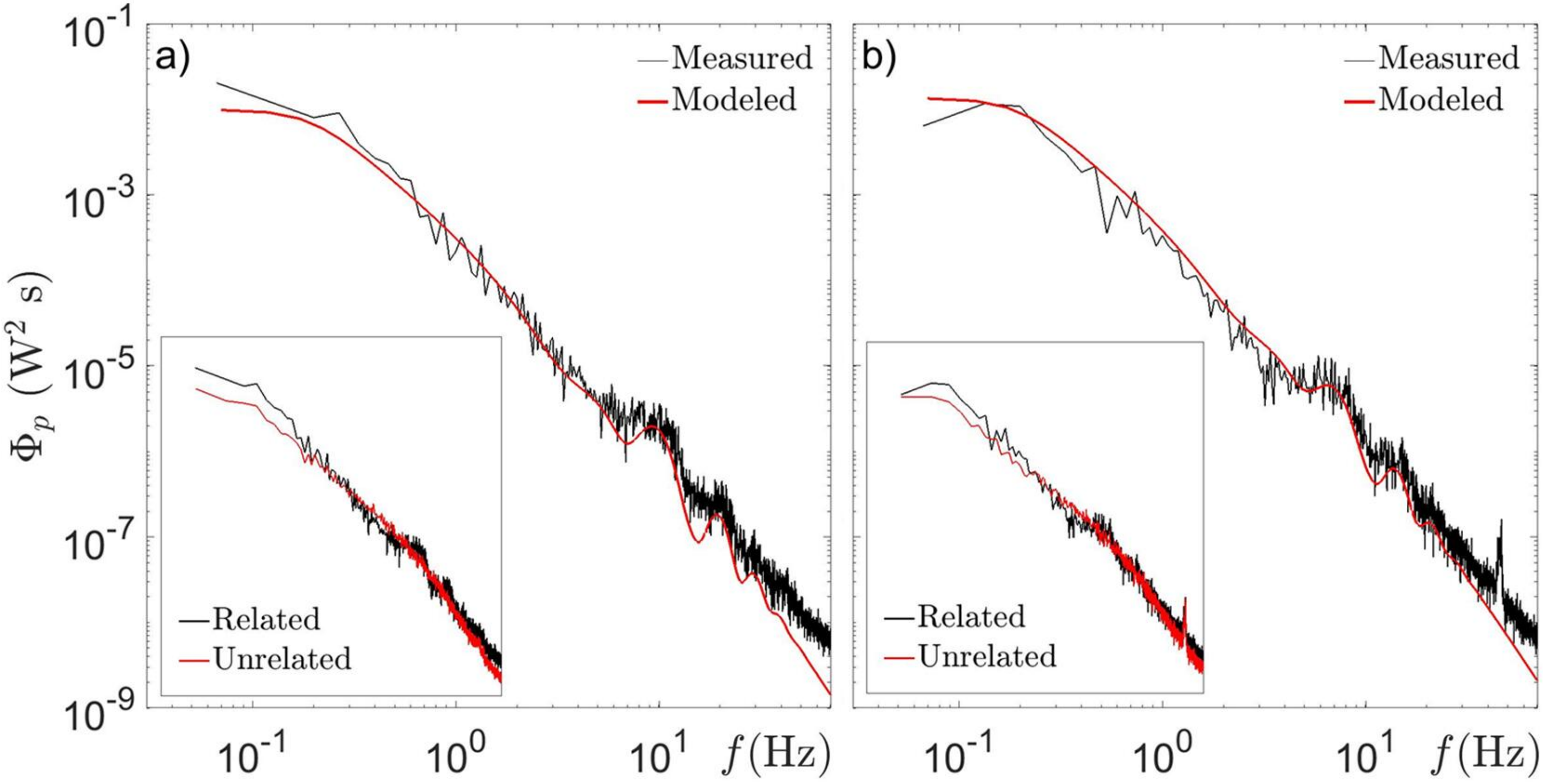

Figure 3.7: Measured and modeled spectra of output power in the wind farm. a) five rows, $S_x = 7$; b) four rows, $S_x = 10$.

related to the advection and turbulent diffusion of large-scale motions lead to small bumps in the spectra of power output in a wind farm.

This work has a broad impact in the scientific and engineering communities as well as industry dealing with wind-farm power fluctuations. Instead of the instantaneous measurements of flow characteristics at the vicinity of each turbine, the framework allows for the estimation of the total power fluctuations of a wind farm using I_u and Λ_u via Φ_u^K. As a distinctive characteristic caused by the spatio-temporal correlation of the flow, the local spectral maximum captured in our wind tunnel measurement have also been observed in field tests (fig. 6 in Calif et al. [17]) as well as numerical simulations (fig. 6 in Stevens and Meneveau [117]), which further verifies our framework. This study also leaves open questions for future investigation. In particular, the characterization of the integral time scale distribution in turbine wakes needs further quantification. Also, the effect of complex topography, wake meandering and layout need to be evaluated in generic conditions. We hope that the insight can provide forward-looking guidance for the power estimation of wind farms and better schemes controlling the power output fluctuations.

Chapter 4

Experimental Investigation of Spatio-Temporal Power Correlations

This chapter is an early version of an article that has since been published in the Journal of Fluid Mechanics by Cambridge Press [123]. The Transfer of Copyright agreement of Cambridge Press states that, "[authors] may reproduce the article or an adapted version of it in any volume of which [they] are editor or author subject to normal acknowledgement." As the author of this thesis and the article in Journal of Fluid Mechanics, and having acknowledged the transfer of copyright to Cambridge Press, I have fulfilled the requirements for reprinting this material.

4.1 Abstract

Simultaneous power measurements from a model wind farm are presented to investigate the spectral correlation of their power output. Application of a random-sweeping hypothesis to the turbulent flow in a wind farm uncovers distinctive correlations, characterized by advection and turbulent diffusion of coherent motions. This correlation is most evident in the cross-spectra of power output between turbine pairs, which contributes to peaks and troughs in the power spectra of the combined signals. These peaks and troughs occur at frequencies corresponding to the advection time between turbines, and diminish in magnitude at high frequencies due to turbulent decoherence. Experimental results support the results from the random-sweeping hypothesis in predicting characteristic advection and decoherence frequencies. The presence of turbine wakes leads to coherence magnitudes smaller than expected. This difference appears to be a function of the flow approaching the first turbine in a pair. The impact of lateral displacement is unclear from the data.

4.2 Introduction

Variability in wind power happens across a wide range of spatial and temporal scales, due to several important physical processes. Over very large scales, when considering the summed power output of several geographically distant wind farms, significant smoothing can occur due to individual wind farms being relatively uncorrelated. Whereas the power spectral density of the power output of a single turbine, or a small wind farm, has been shown to follow a power law of $f^{-5/3}$ [3], [61] observed a behavior of $f^{-2.56}$ when considering the aggregate power of 20 wind farms within ERCOT, the electricity market for most of Texas. [5] later deduced a formulation for the second-order structure function for the aggregate power output with wide geographic smoothing, corresponding to a power-law behavior of $f^{-7/3}$. [5] argues that this power law is the limiting behavior of geographic smoothing, as it is dominated by the immutable variability of individual wind farms.

The $f^{-5/3}$ power law observed by [3] has been explained as stemming from the Kolmogorov $f^{-5/3}$ law for isotropic turbulence [66]. Most justifications for this connection come from the fact that the power spectrum of a turbulent signal raised to any power will exhibit the same $f^{-5/3}$ behavior [5, 13]. This is relevant to the power spectra of wind turbines as the wind-turbine power equation states that $P \propto u^3$, where P is power and u is the wind velocity faced by the turbine. However, this $f^{-5/3}$ does not extend to timescales much faster than ~ 60 seconds, where the effects of rotor inertia filter velocity fluctuations, to give a power-law relation of $f^{-11/3}$ [121].

Different power-law relations are not the only interesting spectral characteristics in wind-farm power. It has previously been observed by multiple researchers that the spectra of the combined power output in wind farms exhibit characteristic peaks at integer multiples of the advective frequency $f_a = 1/t_a$, where t_a, the advective timescale, is the time it takes for a passive tracer particle to travel from one turbine to the next. Attempts to explain and predict this behavior have only recently been undertaken, however. [13] were able to accurately model experimentally measured spectra by treating the problem as a discrete sampling of the velocity in a turbulent boundary layer, with modeled velocity spectra combined with the Kraichnan-Tennekes sweeping hypothesis [69, 119]. The sweeping hypothesis makes the assumption that the turbulent velocity field is randomly advected by a mean and a large-scale sweeping velocity, and has shown to be useful in modeling spatio-temporal spectra in turbulent boundary layers [132].

In the following sections, we attempt to explain the advection phenomenon by creating formulations for the cross-spectra, and related coherence, of the power output of pairs of wind turbines using the random sweeping hypothesis, and testing the assumptions in the sweeping hypothesis with experimental data from the wind tunnel.

4.3 Cross Spectra in Wind Farms

4.3.1 Coherence Spectrum

The power spectrum $\Phi(\omega)$ of a given signal $X(t)$ is defined as the Fourier transform of the signal's autocovariance function $\gamma(\tau)$, as shown in equation 4.1

$$\Phi_X(\omega) = \int_{-\infty}^{\infty} \langle X(t)X(t+\tau)\rangle e^{-i\omega\tau} d\tau \tag{4.1}$$

For a combined signal $X(t) = X_1(T) + X_2(t)$, the autocovariance includes covariance terms between the two signals, i.e.

$$\gamma_X = \langle [X_1(t) + X_2(t)]\,[X_1(t+\tau) + X_2(t+\tau)]\rangle = \gamma_1 + \gamma_2 + \gamma_{1,2} + \gamma_{2,1}, \tag{4.2}$$

where $\gamma_{1,2}$ and $\gamma_{2,1}$ are covariance function between the two signals, where $\gamma_{1,2}(\tau) = \gamma_{2,1}(-\tau)$. This can be generalized to any number of combined signals X_i where $i = 1$, 2, ... N as:

$$\gamma_N = \sum_{i=1}^{N} \gamma_i + \sum_{i=1}^{N-1} \sum_{j=i+1}^{N} \gamma_{i,j} + \gamma_{j,i}. \tag{4.3}$$

Because $\gamma_{1,2}$ and $\gamma_{2,1}$ are mirrored about $\tau = 0$, their Fourier transforms are complex conjugates. For that reason, the combined power spectrum of the N signals is shown to be:

$$\Phi_N = \sum_{i=1}^{N} \Phi_i + 2 \sum_{i=1}^{N-1} \sum_{j=i+1}^{N} \Re(\Phi_{i,j}), \tag{4.4}$$

where $\Phi_{i,j}$ is the cross-spectrum of the signals X_i and X_j. In the case where the two signals are perfectly correlated, $|\Phi_{i,j}| = (\Phi_i \Phi_j)^{1/2}$. It is therefore natural to define the coherence spectrum $C_{i,j}$ as

$$C_{i,j}(\omega) = \frac{\Phi_{i,j}(\omega)}{\sqrt{\Phi_i(\omega)\Phi_j(\omega)}}, \tag{4.5}$$

4.3.2 Random Sweeping and the Coherence of Wall-Bounded Turbulence

In predicting the coherence of the output of pairs of wind turbines, we proceed by using the assumption of Kraichnan-type random sweeping [69]. In order to apply this directly to the power output of wind turbines in a wind farm, two simplifications need to be made. The first of these is that the power spectrum of a signal raised to some power follows the same power law as the signal itself, as $P \propto u^3$. This has been shown to be true by several authors. The second assumption made is that the wind farm flow can be treated as laterally homogeneous. This is clearly not true, as turbine wakes are an important flow characteristic in wind farms. This assumption will be evaluated by the data. The random-sweeping hypothesis makes the assumption that turbulent velocity $\mathbf{u}'$ does not evolve temporally, but is instead advected by a large-scale random sweeping velocity $\mathbf{v}$, as indicated below:

$$\frac{\partial \mathbf{u}'}{\partial t} = \mathbf{v} \cdot \frac{\partial \mathbf{u}'}{\partial \mathbf{x}} = 0 \tag{4.6}$$

The assumption that the small-scale turbulent field and the large-scale sweeping velocity do not non-linearly interact can not be strictly true, though it is attractive for its ability to make analytically tractable expressions for turbulent correlations. Moreover, the random-sweeping hypothesis has been shown to make very good predictions for a range of turbulent flows. The terms $\mathbf{u}'$ and $\mathbf{v}$ in Equation 4.6 are both vectorial. However, if the coordinate axes are defined such that u_1 is aligned with the yaw of a wind turbine, the other components can be ignored in estimating power fluctuations. Furthermore, since $\langle u_1'^2 \rangle$ is typically much larger than $\langle u_2'^2 \rangle$ and $\langle u_3'^2 \rangle$ in a turbulent boundary layer, Equation 4.6 may be reduced to:

$$\frac{\partial u_1'}{\partial t} = (V_1 + v_1') \frac{\partial u_1'}{\partial x_1} = 0. \tag{4.7}$$

The Fourier transform of Equation 4.7 with respect to t can then be taken, which reduces the random sweeping to an ordinary differential equation in x_1 for the quantity $\hat{u}_1(x, \omega)$, which is the Fourier transform of $u'(x, t)$. The cross-spectrum of the turbulent fluctuations at two points that are displaced by a distance x_1 in the streamwise direction can then be expressed as:

$$\Phi_{x,x+\Delta x} = \langle \hat{u}(x, \omega) \hat{u}(0, -\omega) \rangle = \langle \hat{u}(0, \omega) \hat{u}(0, -\omega) \rangle \left\langle \exp\left(\frac{-i\omega \Delta x}{V + v'} \right) \right\rangle. \tag{4.8}$$

If v' is further assumed Gaussian with variance σ_v^2 and small compared to V, the exponential term in angle brackets in Equation 4.8 can be simplified to give the result:

$$\Phi_{x,x+\Delta x} = \langle \hat{u}(0, \omega) \hat{u}(0, -\omega) \rangle \exp\left(-\frac{i\omega \Delta x}{V} \right) \exp\left(-\frac{\omega^2 \Delta x^2 \sigma_v^2}{2V^4} \right). \tag{4.9}$$

Making the further assumption that the lateral behavior of the covariance function $\langle u'(x, y, t) u'(0, 0, 0) \rangle$ is separable, and takes the form of an exponential decay with a length parameter L_y, the final expression for the real part of the cross-spectrum is

$$\Re(\Phi(\Delta x, \Delta y, \omega)) = \Phi(0,0,\omega)\cos\left(\frac{\omega \Delta x}{V}\right)\exp\left(-\frac{\omega^2 \Delta x^2 \sigma_v^2}{2V^4}\right)\exp\left(\frac{y^2}{L_y^2}\right). \tag{4.10}$$

Up to this point, the assumption has been made that the spectra at points $(0,0)$ and $(\Delta x, \Delta y)$ are identical. This may not be the case, however. In order to assure that $0 \leq C_{i,j} \leq 1$, $\Phi(0,0,\omega)$ in Equation 4.10 should be replaced with $(\Phi_i \Phi_j)^{1/2}$. Then, a closed-form expression for the coherence can be taken as

$$C_{i,j}(\omega) = \cos\left(\frac{\omega \Delta x}{V}\right)\exp\left(-\frac{\omega^2 \Delta x^2 \sigma_v^2}{2V^4}\right)\exp\left(\frac{y^2}{L_y^2}\right). \tag{4.11}$$

4.4 Experiments

To test the analytical results found in Section 4.3.2, a set of experiments was performed in the Eiffel-type wind tunnel of the Renewable Energy and Turbulent Environment Group (RE-TE-G) at the University of Illinois. This open-return wind tunnel has a test section of length 6 meters, height 45 cm, and width 90 cm. In order to assess the impact of both turbulence intensity and integral scales, four different flow conditions were tested, along with different inter-turbine spacings for each flow condition. Each layout consisted of three columns of turbines spaced 2.5 rotor diameters apart laterally, and either three or four rows. The model turbines used in the experiment have a rotor diameter $D = 0.12$ m, and are based on a model hydrokinetic turbine from Sandia National Labs [59, 107]. The approach velocity varied between the four test cases, resulting in a range of Reynolds numbers Re_D of 9×10^4 to 1×10^5. The rotors were attached to an electric generator with a rated power of approximately 1 W, which was used both as a loading system and a method to directly measure the power output. The tip-speed ratio λ of the turbines was kept constant at $\lambda = 5.0$ by adjusting the resistance across the generator. The power output from the center column of turbines was sampled simultaneously from the generators of each turbine at a sampling rate of 100 kHz for a duration of 480 s. The incoming velocity was measured both for the incoming boundary layer, and for each turbine that had power measurements taken. Velocity measurements were done via hotwire, and were sampled at a rate of 10 kHz for a duration of 60 s.

Full details on the various flow conditions and wind-farm layouts tested are given in the following subsections.

4.4.1 Turbulent and Laminar Freestreams

Three rows of turbines with hub height $z_h = 0.175$ m were placed with streamwise spacings of 5, 7, and 10 rotor diameters. In the case of laminar inflow, no modifications were made to the wind tunnel, and the upstream contraction and flow straighteners in the wind tunnel resulted in a turbulence intensity of

0.3%, with a mean hub-height velocity of 8.3 ms^{-1}. For the case with a turbulent freestream, an active turbulence-generating grid was placed immediately downwind of the wind tunnel contraction. The turbulence generator consisted of 10 vertical and 3 horizontal rotating bars with agitator wings, which randomly switched rotational direction once per second, and spun at a rate of 0.2 Hz. This led to the creation of large-scale turbulent motions in the relatively short distances of the wind-tunnel test section, with a mean hub-height velocity of 8.3 ms^{-1} and an incoming turbulence intensity of 3% at hub height. The second row of turbines was moved, with lateral offsets as compared to the first and third rows of 0, 0.5, and 1 rotor diameter. A sketch of the experimental layout is given in Figure 4.1.

4.4.2 Rough- and Smooth-Wall Boundary Layers

Four rows of turbines with hub height $z_h = 0.125$ m were placed with streamwise spacings of 7 and 10 rotor diameters. Both cases used the active turbulence generating grid described in the freestream flow section. The smooth-wall boundary layer was created by allowing the flow to develop over the wind-tunnel floor, for a roughness height z_0 of 0.019 mm, a mean hub-height velocity of 8.6 ms^{-1} an incoming hub-height turbulence intensity of 8%. The rough-wall boundary layer used B-flute single-face corrugated cardboard, which resulted in a surface roughness of 0.52 mm, with a mean velocity of 8.5 ms^{-1} and a turbulence intensity of 10%. A sketch of the setup is shown in Figure 4.2

4.5 Results

Each simultaneous set of data was split into ten equally sized non-overlapping windows, and the estimated coherence $\hat{C}$ of each turbine pair was found by averaging the coherence of each subset of data. The result was used to infer the two characteristic frequencies related to advection and turbulent decoherence. The characteristic frequencies ω_a and ω_c, as well as the zero-frequency amplitude a were found by a least-squares fit as indicated below.

$$(a, \omega_a, \omega_c) = \underset{a,\omega_a,\omega_c}{\operatorname{argmin}} \sum_{j=1}^{n} \left| \hat{C} - a \exp\left(\frac{-i\omega_j}{\omega_a}\right) \exp\left(-\frac{\omega_j^2}{2\omega_c^2}\right) \right|^2 . \tag{4.12}$$

In Equation 4.12, two phenomena may contribute to the parameter a. The first of these is lateral displacement, in which case $a = \exp(\Delta y^2/L_y^2)$. However, there may also be a contribution from the alteration of the incoming flow by the turbine wake, leading to a values significantly different than 1 when $\Delta y \neq 0$. Because both power and velocity spectra follow the $\omega^{-5/3}$ law, power coherence can be taken as roughly equal to the coherence of two points immediately upwind of each turbine in the pair. Without either turbine present, the coherence

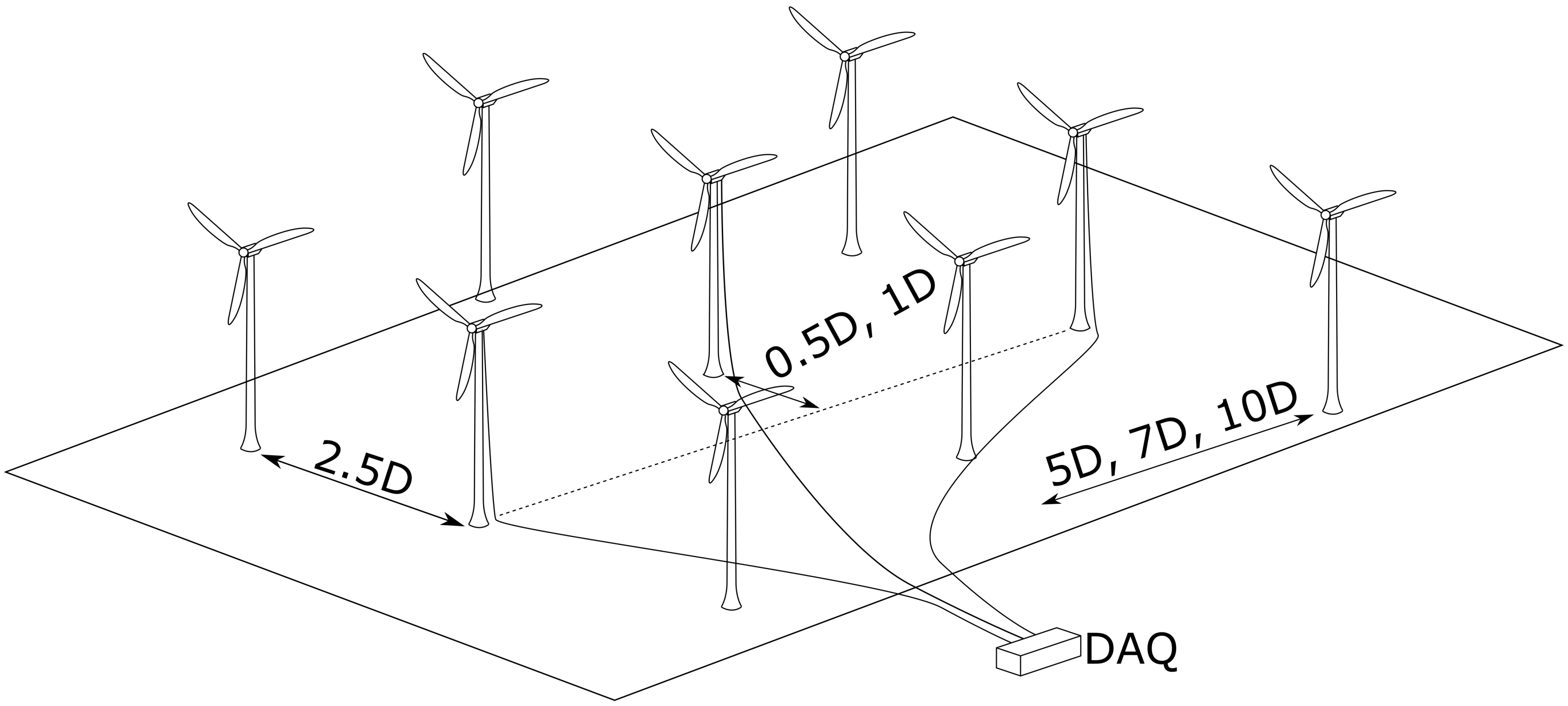

Figure 4.1: Conceptual schematic freestream experiments.

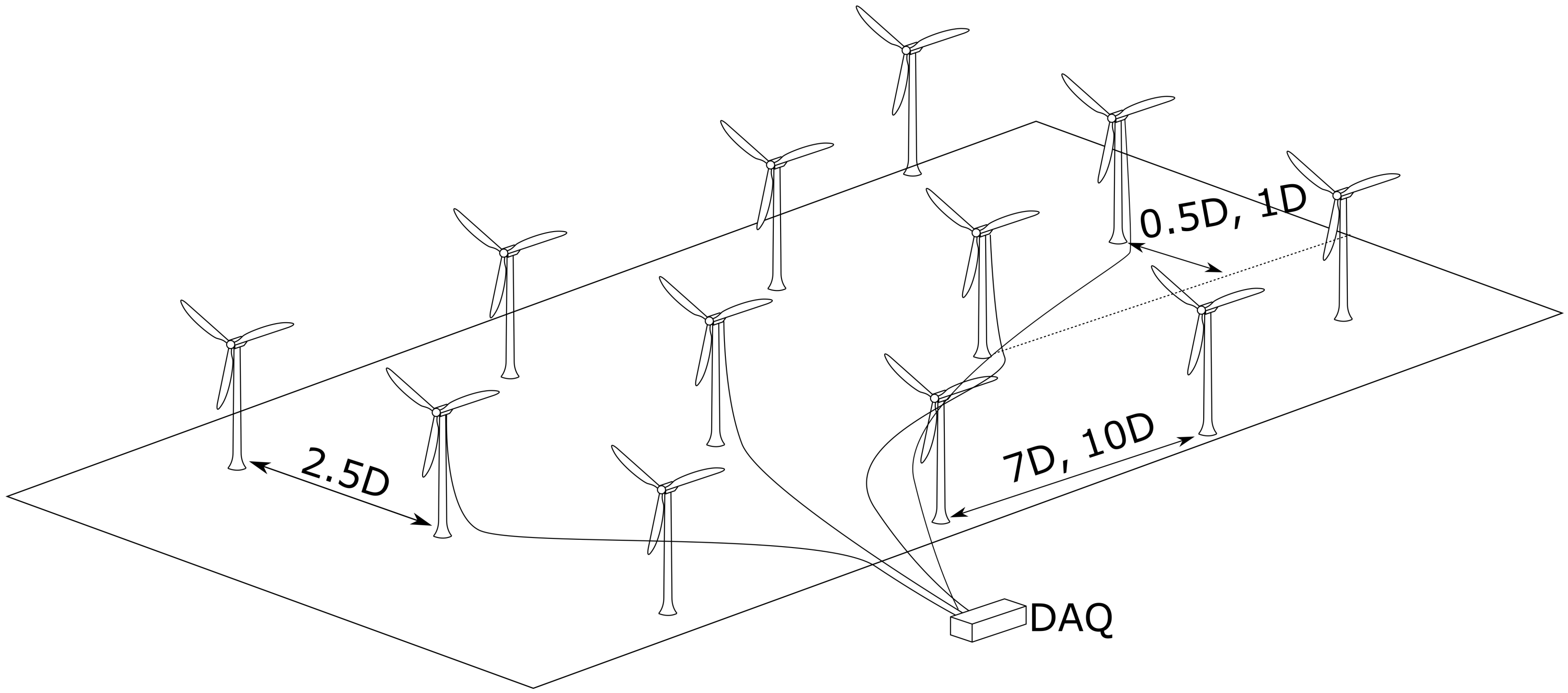

Figure 4.2: Conceptual schematic boundary-layer experiments.

of these two points should be closely approximated by the sweeping hypothesis. However, the modulation of the flow structure by the turbine interacting with the flow should affect the coherence. In the absence of a simple physical explanation for the change in coherence across the turbine rotor, we simply assume that the passage through a turbine rotor reduces the coherence by a multiplicative constant a at all frequencies.

The least-squares estimates of the characteristic frequencies ω_a and ω_c can then be compared to their theoretical values as predicted in Section 4.3.2. Namely, we should expect that

$$\omega_a = \frac{V}{\Delta x}, \tag{4.13}$$

and

$$\omega_c = \frac{V^2}{\Delta x \sigma_v}. \tag{4.14}$$

The general complex exponential behavior of the power spectrum is quite consistent with the data. An example coherence spectrum is shown in Figure 4.3. The least-squares estimates for ω_a closely fit the predictions, with and R^2 value of 0.64. However, the values of ω_c show significantly more noise, with an R^2 value of 0.44, although the general trend is predicted well. Measured values of the two frequencies are plotted versus their prediction in Figures 4.4 and 4.5.

The data suggest that the zero-frequency coherence magnitude a is dependent on the characteristics of the approaching flow. Though other flow statistics may contribute to the coherence, we find that the integral time scale of the flow approaching the most upwind turbine in a pair as well as the turbulence intensity can explain much of the variation of a with different flows. The turbine operation may also impact a; for instance, if a turbine is strongly curtailed, it should not introduce as many uncorrelated turbulent scales in its wake as a turbine that is operating at optimum efficiency. However, this is beyond the scope of the current work. As seen in Figure 4.6, a clear parametric dependence exists for a on the values of I_u, or turbulence intensity, and T_u, which is the integral time scale of the flow approaching the first turbine in a pair. This figure shows only a values for turbine pairs which are one row apart. This result suggests that the impact of wakes on the coherence is most pronounced when the flow is laminar or has smaller-scale turbulent motions. This might be the case during clear nights, when the atmospheric boundary layer is generally stable. On the other hand, strong coherence is found with very large, energetic turbulent motions which may be found in the day-time unstable boundary layer.

For turbine pairs spanning more than two rows, smaller values of a are found. The data appear to suggest that the a value for a pair separated by two rows may be equal to the square of a similar setup separated by only one row. That is, where a_1 is the a-value for a pair of turbines separated by one row and a_2 is a similar a-value for turbines separated by two rows, $a_2 = a_1^2$. Similarly, a values for a pair separated by three rows are approximately equal to the cube

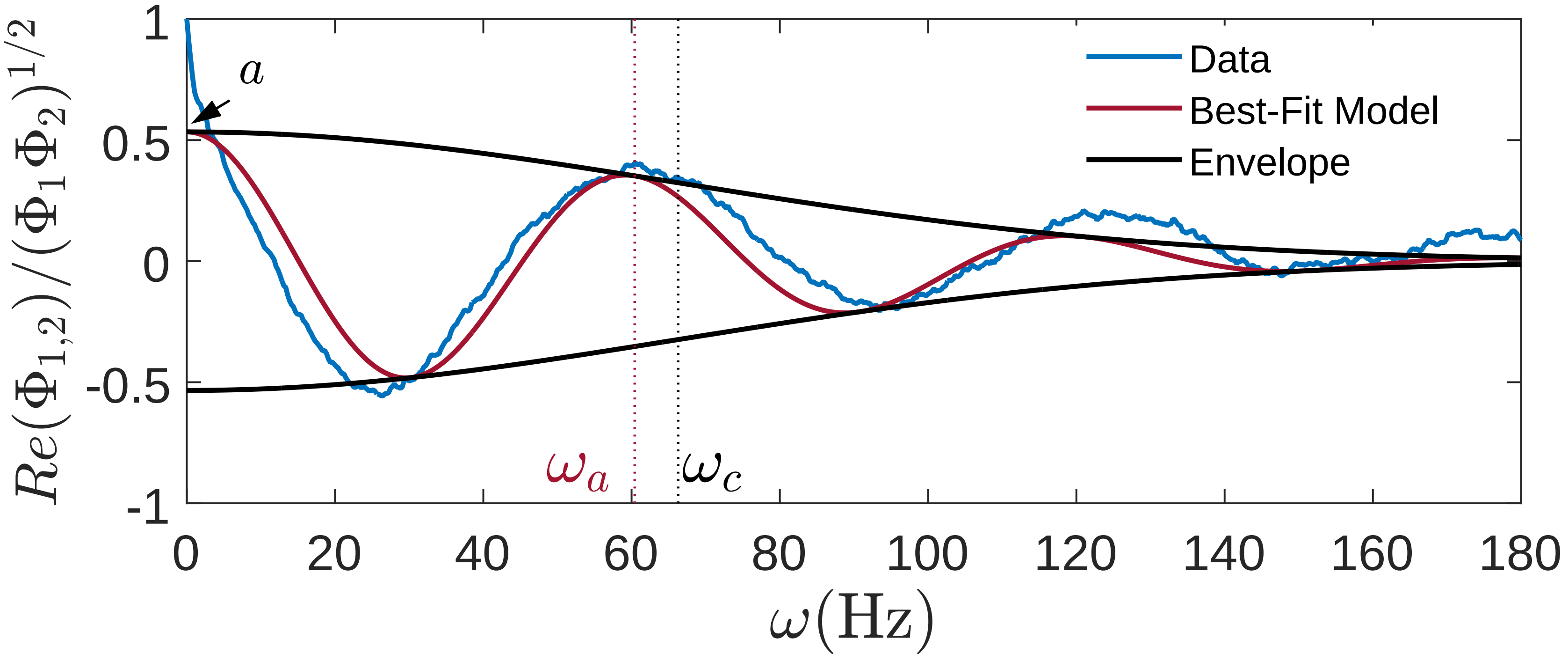

Figure 4.3: Sample coherence data from the rough-wall, $7D$-spacing experiment.

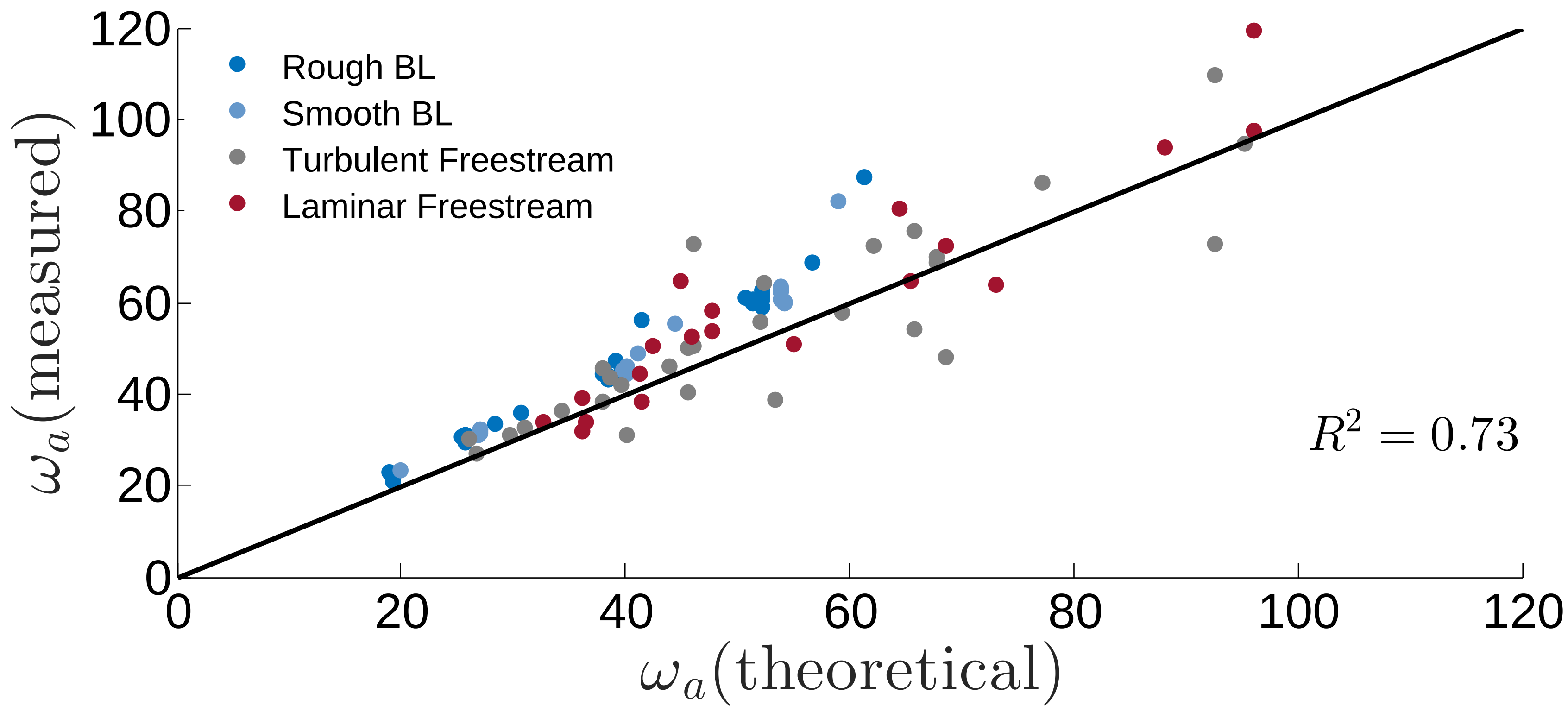

Figure 4.4: Conceptual schematic boundary-layer experiments.

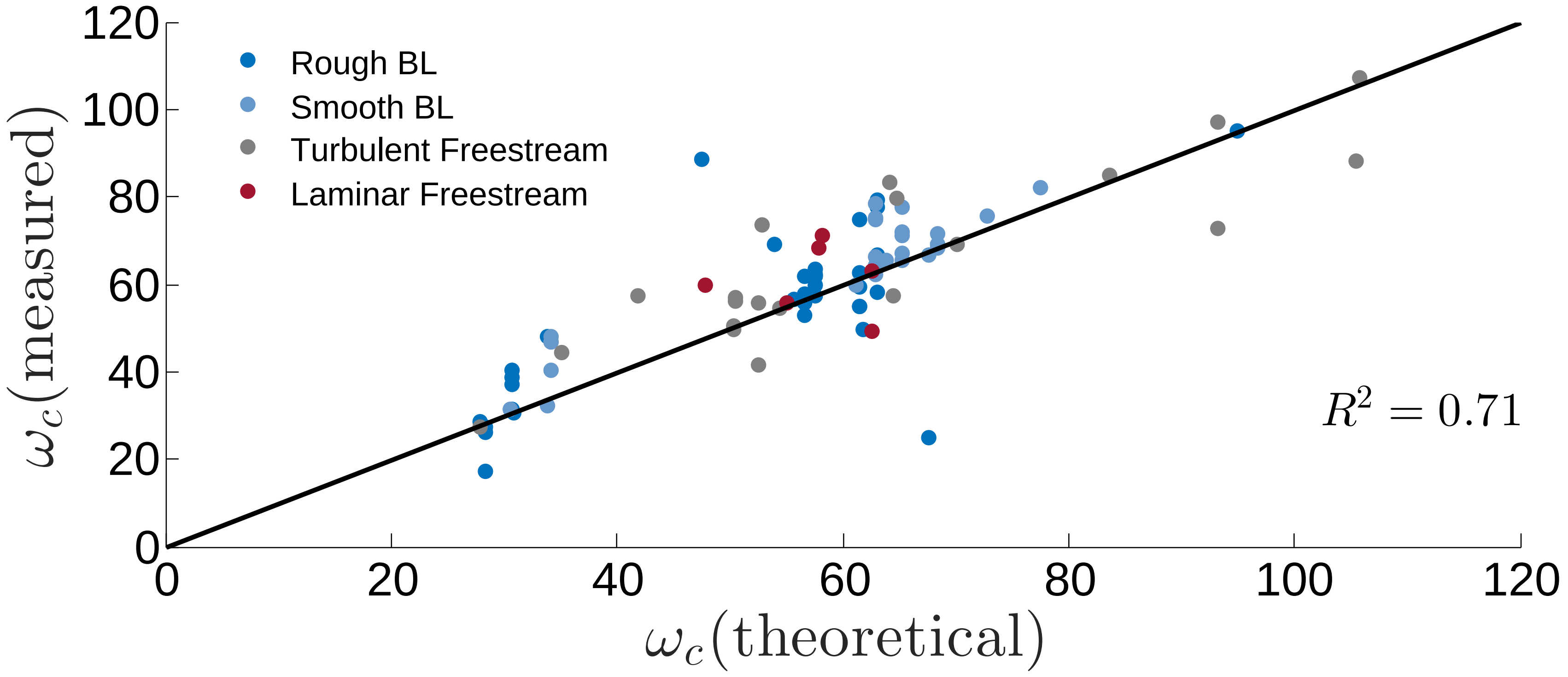

Figure 4.5: Conceptual schematic boundary-layer experiments.

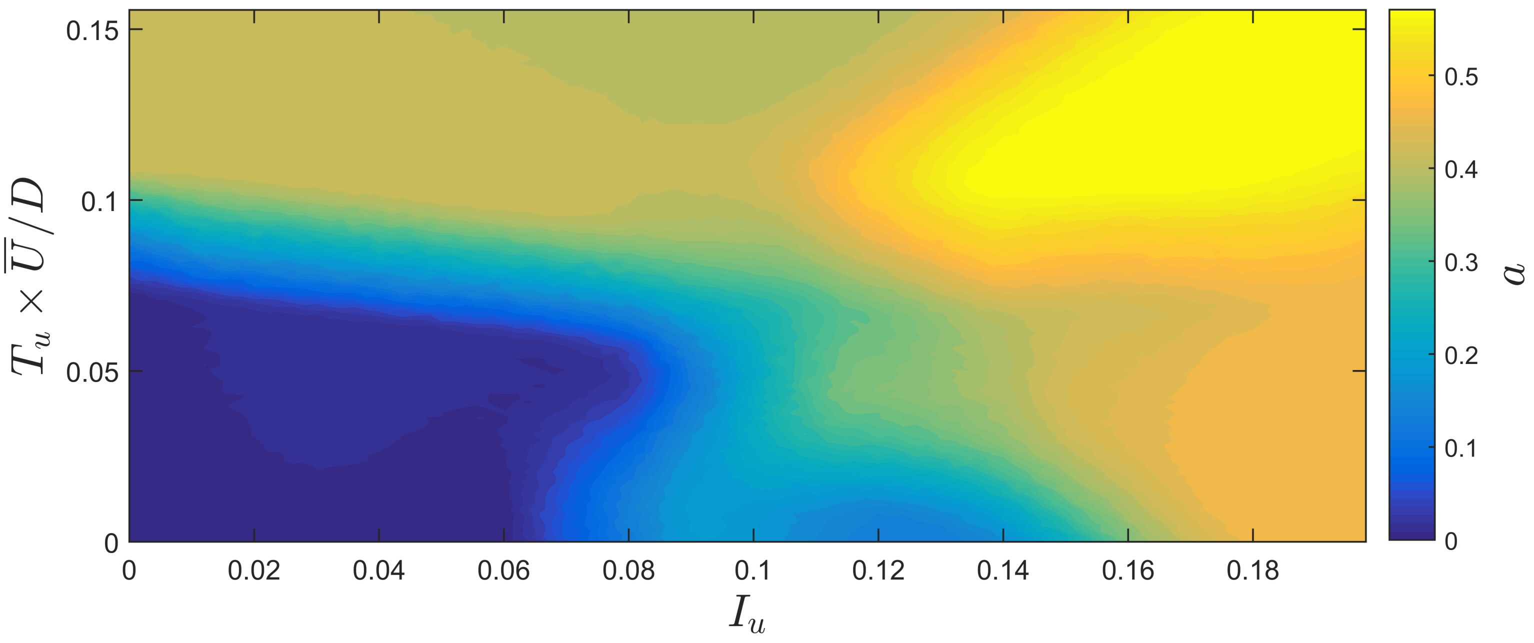

Figure 4.6: Dependence of zero-frequency coherence magnitude on turbulence intensity and integral time scale.

of a similar one-row setup. When comparing two-row pairs to similar one-row pairs, the exponent is 2.2 ± 0.3. When comparing three-row and one-row pairs, the exponent is 3.3 ± 0.9. It therefore cannot be ruled out that $a_n = a_1^n$. More data would help to validate this hypothesis.

The effect of lateral displacement is unclear from the data. While a monotonically decreases with greater Δy in both of the boundary-layer cases, the data from the freestream cases decrease between $\Delta y = 0$ cm and $\Delta y = 6$ cm, but then subsequently increase again at $\Delta y = 12$ cm. It is unclear why this difference occurs, though wake effects may play a role.

4.6 Concluding Remarks

The random-sweeping hypothesis does well in predicting the general behavior of the coherence of wind-turbine pairs. The complex exponential structure predicted is observed in the experimental data. However, the turbine wakes appear to diminish the magnitude of the coherence by a multiplicative constant $a \in [0, 1]$. It is found that a is strongly dependent on the structure of the flow approaching the first turbine in a pair. Namely, the turbulence intensity and integral scales of the flow appear to affect a in such a way that flows with high-energy, large motions have the largest values of a. However, it is still not clear how the turbulence created in the turbine wake impacts the coherence. A physical framework which accounts for the described observations is therefore desirable. This framework should describe the turbine-induced turbulence, which is expected to lead to non-coherence in the power output of turbine pairs. The data from the laterally displaced turbines does not clearly show a trend in the magnitude of coherence.

Chapter 5

Numerical Investigation of Spatio-Temporal Power Correlations

5.1 Abstract

Wind-farm large-eddy simulations are used to uncover the dependence of temporal correlations in the power output of turbine pairs on atmospheric stability. For this purpose, a range of five distinct stability regimes are investigated with the same aligned wind-farm layout used among simulations. The coherence spectrum between turbine pairs in each simulation is compared to theoretical predictions. We found that higher levels of atmospheric instability lead to higher coherence between turbines. This is attributed to higher dominance of atmospheric motions over wakes in highly unstable flows. An empirical model for wake-added turbulence is shown to adequately predict the variation of coherence with ambient turbulence intensity. The majority of the analytical work and the majority of the writing in this chapter were done by Nicolas Tobin, but the large-eddy simulations were performed by Adam Lavely.

5.2 Introduction

The characteristics of spatiotemporal correlations in atmospheric flows play a major role in determining the variability of wind-power resources. For instance, Archer and Jacobson [4] found that interconnecting a number of wind farms would allow for an average of 33% of the yearly averaged power to be used as baseload power by reducing variability. This occurs due to distant wind farms are not strongly correlated, whereas a single wind farm is not able to reliably supply baseload power. Using power data from a set of 19 wind farms, Archer and Jacobson [4] suggested that there was seemingly no saturation point, past which the inclusion of more wind farms would not allow for greater reliability. Katzenstein et al. [61] used a dataset from 20 wind farms in Texas to show how geographic smoothing impacted wind-power fluctuations at different timescales. They found that over timescales of one hour, a reduction in variability of 87% was achieved, while the 24-hour variability was not significantly attenuated. This is consistent with the findings of Bandi [5], who used turbulence theory to show that a limiting behavior exists in the smoothing of wind-power fluctuations, and used the same Texas wind-farm dataset as Katzenstein et al. [61] as well as a set of 224 Irish wind farms to confirm that this limit has already been reached in these two aggregates. A similar asymptote in smoothing behavior was found by Fertig et al. [37], who analyzed the power output of a large number of wind farms throughout the United States, considering the effect of theoretical interconnects between four geographical regions and found that much of the reduction in variability that was achieved with a very large number of wind plants can be reproduced with only four or five.

It is clear from the literature that correlations corresponding to length scales on the order of hundreds of meters and timescales from an hour to days impact power fluctuations. However, Fertig et al. [37] noted that Sørensen and Shen [113] used a similar method of analysis to investigate fluctuations over short timescales in a single wind farm, pointing to a "fractal property of wind energy". Sørensen and Shen [113] noted that the spectrum of the power fluctuations from a wind farm includes cross-spectral terms, and modeled them with an empirical coherence function, originally suggested by Schlez and Infield [105], which uses fitted constants to model the decay of correlation at high frequencies as a function of streamwise and lateral displacement, and found that this empirical model fit well to the data from two offshore wind farms in Denmark. Also included in their model coherence function is a complex exponential term that accounts for the phase lag as motions pass between rows of turbines, though the implications of this assumption were not discussed. Over short timescales, when the wind is relatively steady, Stevens and Meneveau [117] observed that strong spectral peaks occur in the aggregate spectrum of a wind farm, and these peaks correspond to the time it takes for turbulent motions to pass from one row of turbines to the next. This is consistent with the suggestion of Sørensen and Shen [113] that the coherence spectrum have a sinusoidal characteristic associated with the inter-row passage time scale.

Though Sørensen and Shen [113] showed that the empirical coherence function of Schlez and Infield [105] was effective in predicting the correlation terms in the spectra of wind farms, recent effort has gone toward a more physical understanding, using the Kraichnan-Tennekes [69, 119] random-sweeping hypothesis (RSH). Liu et al. [77] applied the RSH as part of an effort toward modeling the power fluctuations of an entire wind farm, and arrived at an expression for the coherence function that did not depend on fitted parameters, but instead on the turbulence intensity of the incoming boundary-layer flow and showed good agreement with wind-tunnel experimental results. Bossuyt et al. [13] similarly used the RSH in treating a wind farm as a discrete sampling kernel of the turbulent boundary layer, and successfully predicted the spectral peaks measured in a wind-tunnel experiment.

However, both Liu et al. [77] and Bossuyt et al. [13] made the simplifying assumptions of a wind farm in a neutrally stable atmospheric boundary layer, and that wakes do not play an important role in determining the correlations of turbine pairs. However, in both instances, the magnitude of the spectral peaks was slightly over-estimated, particularly for pairs of turbines that were separated by more than one row. This may be because, depending on the lateral separation between a pair of wind turbines, either turbine may experience wake motions from upwind turbines. As wake motions tend to be much smaller in scale than boundary-layer motions, and are inherently localized, a component of the turbulence approaching either turbine may, then, not be strongly correlated with that approaching the other turbine. Since the characteristics of the boundary-layer turbulence depend strongly on the atmospheric stability state, the fractional contribution to the overall turbulence kinetic energy that is due to upwind wake motions, and therefore the characteristics of turbine-turbine correlations, should therefore depend on atmospheric stability.

In this paper we aim to explore the characteristics of the coherence spectrum of turbine pairs as a function of atmospheric stability and wake-added turbulence, with data from large-eddy simulations spanning several atmospheric stability conditions. In Section 5.4, the methods of performing the large-eddy simulations as well as the details on the different stability states are presented. In Section 5.5, the impact of flow conditions on turbine-turbine coherence is investigated, as well as the effects of lateral displacement between turbine pairs.

5.3 Coherence and the Random Sweeping Hypothesis

The Kraichnan-Tennekes random-sweeping hypothesis is an expansion of the frozen turbulence hypothesis, which makes the assumption that turbulent motions are advected by the mean velocity, and do not evolve temporally. The RSH similarly assumes that turbulent motions do not evolve temporally, but adds a random sweeping velocity to the advection, so that

$$\frac{\partial \mathbf{u}'}{\partial t} + (\mathbf{V} + \mathbf{v}')\frac{\partial \mathbf{u}'}{\partial \mathbf{x}} = 0, \tag{5.1}$$

where $\mathbf{u}'$ is the vector field of turbulent fluctuating velocity, $\mathbf{V}$ is the mean velocity vector, and $\mathbf{v}'$ is a large-scale sweeping velocity. By assuming that the sweeping velocity is zero-mean and normally distributed with standard deviation σ_1, Liu et al. [77] suggested that the cross-spectrum $\Phi_{1,2}$ of two turbines spaced a distance Δx apart in the direction of the mean flow would take the form

$$\begin{aligned}\Phi_{1,2}(f) = &\sqrt{\Phi_1 \Phi_2} \exp\left(-\frac{2\pi i f \Delta x}{V_1}\right) \times \\ &\exp\left(-\frac{2\pi^2 f^2 \Delta x^2 \sigma_1^2}{V_1^4}\right),\end{aligned} \tag{5.2}$$

and therefore, the coherence spectrum $C_{1,2}$ could be expressed as

$$\begin{aligned} C_{1,2}(f) =& \frac{\Phi_{1,2}}{\sqrt{\Phi_1 \Phi_2}} = \exp\left(-\frac{2\pi i f \Delta x}{V_1}\right) \times \\ & \exp\left(-\frac{2\pi^2 f^2 \Delta x^2 \sigma_1^2}{V_1^4}\right), \end{aligned} \tag{5.3}$$

However, as seen in Fig. 7 of Liu et al. [77] and Figures 5 and 6 of Bossuyt et al. [13], a straightforward application of the RSH, treating turbines as probes of turbulence, tends to overpredict the magnitude of the spectral bumps.

5.4 Large-Eddy Simulations

We use large-eddy simulation (LES) to simulate a wind farm within Earth's atmospheric boundary layer using a finite-volume solver for the incompressible filtered Navier-Stokes equations. The solver contains in-house modifications to the National Renewable Energy Laboratory's SOWFA [31, 30, 57] solver for atmospheric turbulence, adding the Moeng surface stress model [84, 85] for better capturing the velocity gradient near the wall and the Smagorinsky sub-filter model [111] to SOWFA's OpenFOAM [52] framework.

The velocity, u_i, is decomposed into the resolved, $\bar{u}_i$, and sub-filter, u_i', velocities

$$\bar{u}_i = u_i - u_i' \tag{5.4}$$

where the resolved portion is used in the momentum equation,

$$\frac{\partial \overline{u}_i}{\partial t} + \frac{}{\partial x_j}(\overline{u}_i \overline{u}_j) = -\underbrace{2\epsilon_{i3k}\omega_3 \overline{u}_k}_{\text{a}} - \underbrace{\frac{1}{\rho_0}\frac{\partial p_0}{\partial x_i}}_{\text{b}} - \underbrace{\frac{1}{\rho_0}\frac{\partial \tilde{p}}{\partial x_i}}_{\text{c}} - \underbrace{\frac{\partial \tau_{ij}^D}{\partial x_j}}_{\text{d}} + \underbrace{g\left(\frac{\overline{\theta} - \theta_0}{\theta_0}\right)}_{\text{e}} + \underbrace{\frac{F_i}{\rho_0}}_{\text{f}} \tag{5.5}$$

which includes terms for atmospheric boundary-layer flows. The time derivative and convective transport terms are found on the left-hand side. The right-hand-side includes (a) the Coriolis force from rotation, (b) the driving pressure gradient, (c) the local pressure gradient and the stress-tensor trace, (d) the viscous stresses, τ, (e) the Boussinesq approximation for the buoyancy taking into account the local temperature variation, and (f) the applied body force from the turbine, calculated using an actuator disk model. The incompressible continuity equation,

$$\frac{\partial \overline{u}_i}{\partial x_i} = 0 \tag{5.6}$$

is enforced using a pressure Poisson equation. A transport equation for the potential temperature,

$$\frac{\partial \theta}{\partial t} + \frac{\partial}{\partial x_j}(\overline{u}_j \overline{\theta}) = -\frac{\partial q_j}{\partial x_j} \tag{5.7}$$

is solved with a Boussinesq approximation for buoyancy where q_j includes both the SFS contribution to turbulent transport and flux through the domain boundaries. We use second-order schemes for spatial and temporal derivatives, and the precursor-to-wind farm one-way coupling documented by Churchfield et al. [31] and Jha et al. [56]; this allows developing atmospheric turbulence in a larger, periodic domain which is then fed into a smaller domain with the wind farm.

A 5 km × 5 km × 2 km precursor domain with 10 m spacing is used to develop atmospheric turbulence within a periodic domain [65]. The boundary layer is allowed to develop until it reaches equilibrium, where the boundary layer height becomes stationary within a single vertical cell and $\overline{u}_* = (\overline{\tau}_w/\rho)^{1/2}$ becomes constant. This is done with a capping inversion for the moderately-convective and neutral simulations. The turbulence is then fed into a smaller atmospheric boundary layer domain as a temporal boundary condition with mesh resolution of 4 m over a 1.5 km × 1.5 km × 0.4 km domain containing a wind farm with sixteen 2.5 MW turbines modeled using an actuator disk [14] approach, following validated practices [55, 54]. The wind turbines are aligned in a 4×4 pattern with 5 diameter (D) spacing in both directions ($S_x/D = S_y/D = 5$) with the incoming mean wind aligned with the turbine columns. The pitch and RPM controllers are set to constant values appropriate for the local mean wind speed within the wind farm configuration. A temporally constant geostrophic wind [35] is prescribed to model the low-level jet for the stable boundary layer for the wind-farm simulation. The wind farms are run through the start-up transient where the turbine wakes develop and then data are sampled for 2000 seconds.

Table 5.1 shows the various stability states modeled with the surface heating used and the mean wind speed and turbulence intensity at half the boundary layer height from the precursor simulation. Representative, spatially-distributed instant of the streamwise velocity at the turbine hub-height is shown in Figure 5.1, where iso-contours of the vertical velocity $u_z = -1$ m s^{-1} are superimposed for the lower half of the domain. The moderately convective boundary layer, shown in Figure 5.1a, has elongated horizontal velocity structures aligned with the flow that correlate well with negative vertical velocity. These structures are on the order of rotor diameter in width and longer in length, leading to the structure being felt by downwind turbines within the array. The velocity structures in the neutral case (see Figure 5.1b) are smaller than the convective case and are not elongated in the streamwise direction. These structures are on the order of a rotor diameter in both horizontal directions. The weakly stable case illustrated in Figure 5.1c also lacks the elongated structures found in the moderately convective case, and has structures associated with the temperature not found within the neutral case.

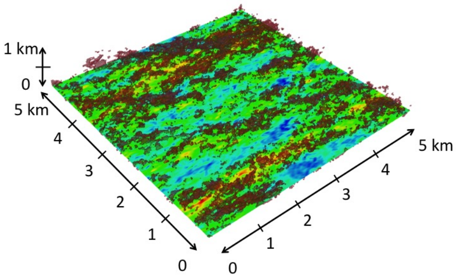

(a) Moderately convective ($\frac{-z_i}{L} = 7.8$)

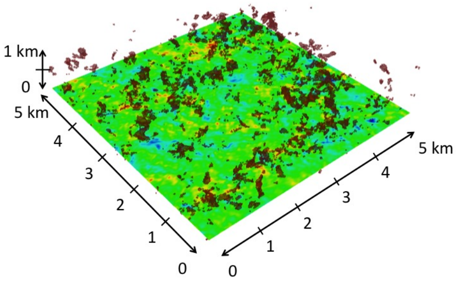

(b) Neutral ($\frac{-z_i}{L} = 0$)

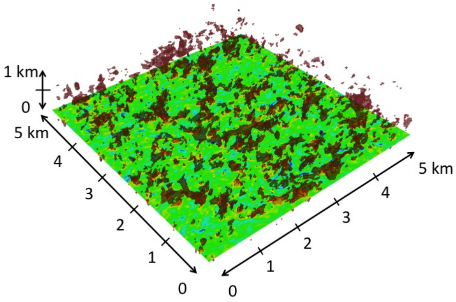

(c) Weakly stable ($\frac{-z_i}{L} = -2.1$)

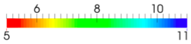

Figure 5.1: Isocontours of horizontal velocity at turbine hub height superimposed with isosurfaces of vertical velocity $u_z = -1$ m s^{-1}, for the 5 km × 5 km precursor simulation.

Table 5.1: The atmospheric stability states used for the wind farm simulations.

Boundary Layer	**Stability** ($-z_i L^{-1}$)	**Surface Heating** (K m s^{-1})	**Wind Speed** (m s^{-1})	**Turbulence Intensity** (%)
Moderately Convective	7.8	0.20	9.59	17.2
Slightly Convective	2.3	0.04	9.51	15.4
Neutral	0	0	8.41	11.1
Stable	-2.1	-0.03	9.26	8.8

5.5 Results and Discussion

In calculating the coherence of turbine pairs from the LES data, a significant trade off is in maintaining both high frequency resolution at low frequencies, and low bias at high frequencies. This trade off lies in the number of sub-windows to use when calculating the spectra and cross-spectra of power output. When using a small number of windows, high-frequency coherence estimates are noisy and biased; however, low frequency components are estimated with adequate resolution to characterize the advection time. That is, the coherence was estimated at enough frequencies to properly characterize a cycle in the advective term of the RSH coherence equation 5.3. In contrast, with a large number of windows, the high-frequency coherence results are unbiased, but the low-frequency coherence is not sufficiently resolved. We therefore estimated the coherence with a different number of windows, and accepted only a specific range of frequencies from each estimate so that coherence estimates were reported only for frequencies with fewer than 16 cycles in each window, as we found that this gave the best coherence results. The frequency ranges and the number of windows used in that range are listed in Table 5.2. An example of the calculated coherence from the neutrally convective case is shown in Figure 5.2.

fS_xD/U	0-1	1-2	2-4	4-8	8-16	16-32	32-64	64-128
N^o of windows	2	4	8	16	32	64	128	256

Table 5.2: Number of windows used in calculating coherence from LES data across ranges of frequencies.

With the coherence estimates, the f_a, f_c, and C_0 were found such that the RSH estimate minimized the squared error between prediction and data, so that the function fitted to the data was

$$C_{fit} = C_0 \exp\left(-\frac{2\pi i f}{f_a}\right) \exp\left(-\frac{f^2}{2f_c^2}\right). \tag{5.8}$$

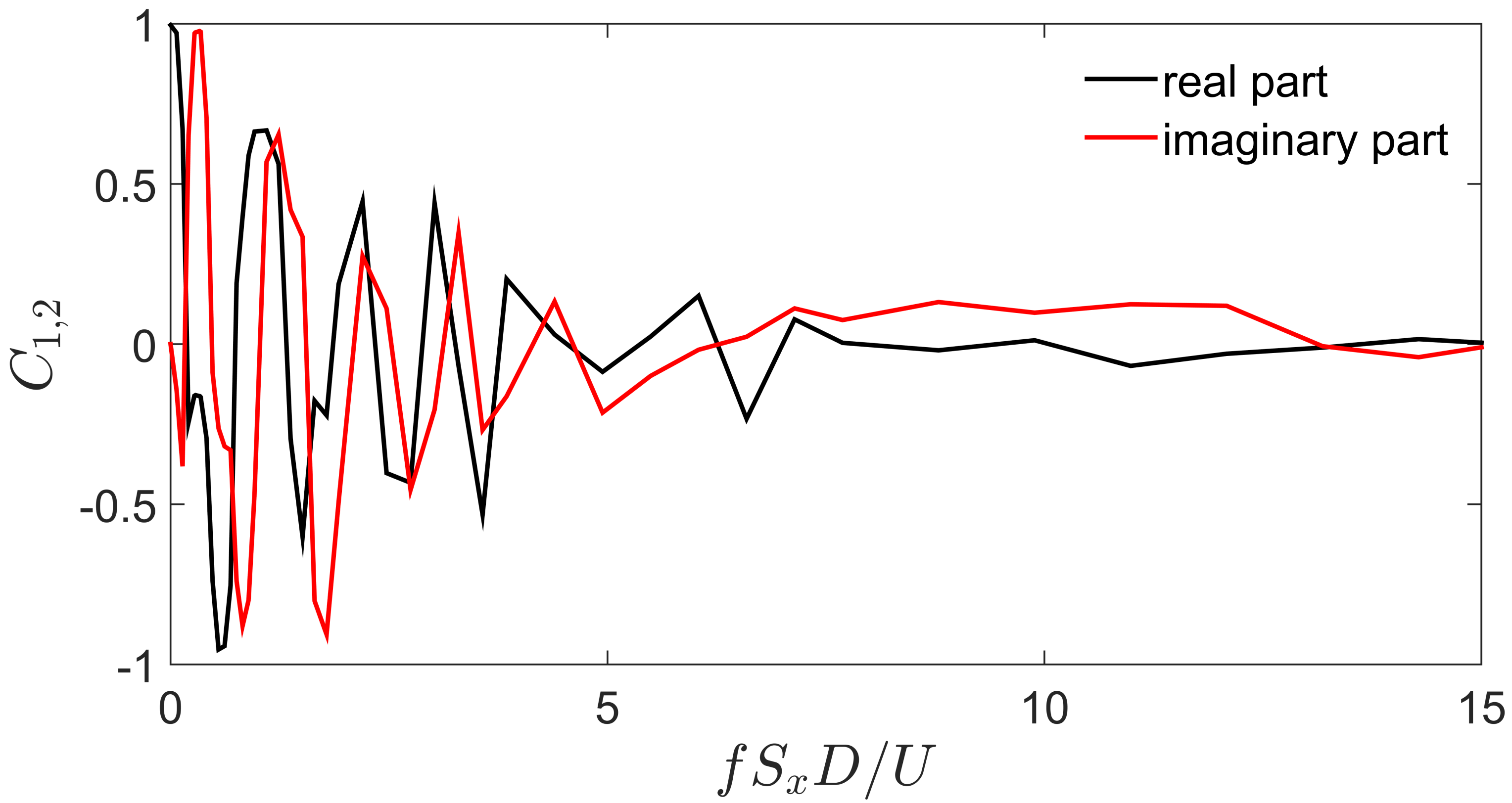

Figure 5.2: Sample coherence spectrum from two wind turbines in a neutral boundary layer flow.

The two characteristic f_a and f_c [77] are compared to their prediction from the RSH, namely

$$f_a = \frac{U}{\Delta x}, \tag{5.9}$$

and

$$f_c = \frac{U^2}{2\pi \Delta x \sigma_1}. \tag{5.10}$$

Further, the role of the atmospheric turbulence in determining the coherence scaling factor C_0 is assessed.

5.5.1 Advection of Turbulent Motions

The mean fitted values of f_a are shown in Figure 5.3 plotted against streamwise distance for each inter-turbine spacing, and for each stability condition. Also plotted in the figure is the value of f_a predicted by the RSH; it shows a clear trend toward lower frequencies with higher separation, as the advection time between turbines becomes higher. The f_a values are fit closely between the five flow conditions. The advection frequency does not appear to be strongly impacted by turbine wakes, at least in the four rows of turbines investigated. This suggests that coherent motions are primarily advected at the boundary-layer velocity, rather than the local wake velocity.

The fact that motions are advected at the undisturbed boundary-layer velocity comes with interesting implications about the role of wakes as compared to large-scale atmospheric motions in the context of the RSH. The RSH makes the assumption that the sweeping velocity occurs at length and time scales that are very large compared to turbulence scales of interest. This is a valid assumption of large-scale atmospheric motions, which may be kilometers long and last over timescales on the order of tens of minutes, as compared to typical ∼1 km inter-turbine separations in wind farms, and the resultant advection time of ∼60 s. However, this is not true of wake-added turbulent motions, which are typically over timescales an order of magnitude higher than the time it takes for the rotor to complete one revolution and smaller [24, 78], so that the wake-added motions are similar or smaller in scale to the advection time scale, allowing them to nonlinearly interact. Wake-added motions may then not be expected to contribute to the coherence between turbine pairs, with the coherence instead being dominated by the impinging of turbulent motions from above. Although the added drag by wind turbines will impact the characteristics of the overhead boundary layer, this typically occurs over many rows of turbines, and would not be expected to occur over the relatively small extent of the modeled wind farms.

It is noted that no dependence of the lateral spacing on the advective frequency was found; f_a values for turbine pairs that were separated laterally were the same as those not laterally separated within uncertainty.

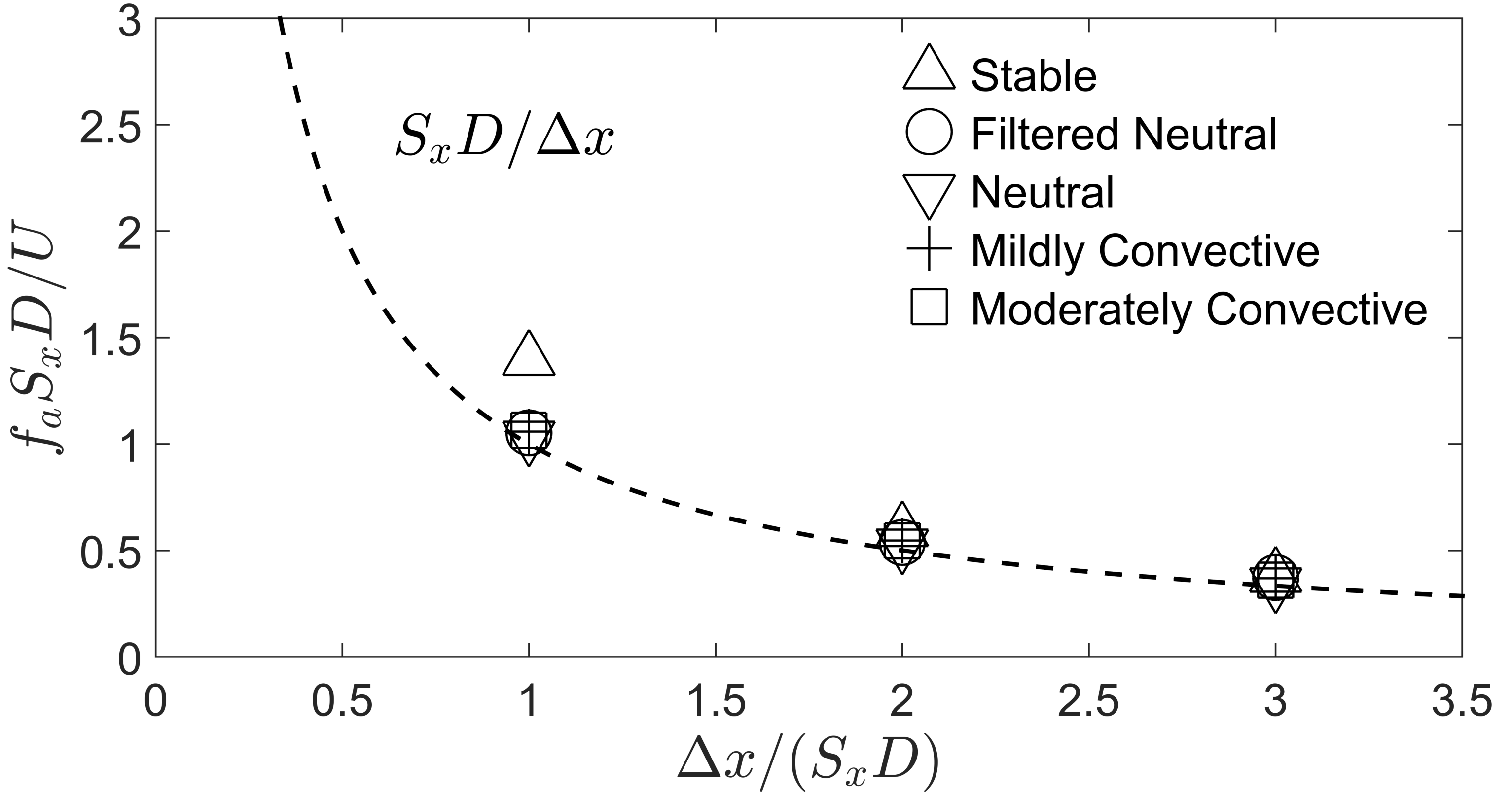

Figure 5.3: Mean least-squares estimate of f_a for all flow cases.

5.5.2 Turbulent Decoherence of Turbulent Motions

Further evidence of the dominant role of atmospheric motions is seen in the decoherence frequency, the estimates of which are presented in Figure 5.4. The mean values of the decoherence frequency are shown plotted along with their predicted trend, according to Equation 5.4. The fact that the decoherence frequency follows the trend predicted by the RSH suggests that the proper turbulence intensity scale for this quantity is that of the incoming boundary layer. If the wake turbulence were dominant in the distortion of high-frequency components, a trend should exist showing f_c values deviating below their RSH predictions with larger Δx, as the wakes of an increasing number of turbines impacts the turbulence approaching the downwind turbine in a pair with larger separation. This trend, however, is not observed; though deviations between measurements and RSH predictions are larger than for the values of f_a, the boundary-layer turbulence appears to be the appropriate scale in predicting f_c.

5.5.3 Coherence Scaling Factor

Though the timescales of turbine-turbine coherence does not appear to be altered by turbine wakes, the wakes will nonetheless introduce turbulence scales that impact the downwind turbine in a pair, and lead to fluctuations in that turbine. Although correlations have been observed between a turbine's power and the motions in its wake [48], we proceed with the assumption that these scales are small enough that they experience sufficient nonlinear evolution that they do not lead to correlations between the power output of two turbines. There is therefore a fraction of the turbulence approaching the downwind turbine that does not lead to power coherence. We proceed to link this fraction to the wake-added turbulence, using existing empirical formulations from the literature.

The turbulence intensity in the wake, I_{wake}, is commonly decomposed [19] into a contribution from the ambient (I_0) and wake-added (I_+) components, as

$$I_{wake}^2 = I_0^2 + I_+^2. \tag{5.11}$$

Since the power spectral density of a turbine's power output is proportional to the turbulence kinetic energy [121], the coherence should then scale as

$$C_{1,2} \propto \frac{\hat{I}_0 \hat{I}_{wake}}{I_0 I_{wake}}, \tag{5.12}$$

where $\hat{I}_0$ and $\hat{I}_{wake}$ are the components of the upwind and wake turbulence that are coherent. If the upwind turbulence is assumed to advect naturally between rows via impinging of large-scale motions, and the wake-added turbulence is not expected to contribute any to any turbine-turbine power correlations, then $\hat{I}_0 = \hat{I}_{wake} = I_0$, and

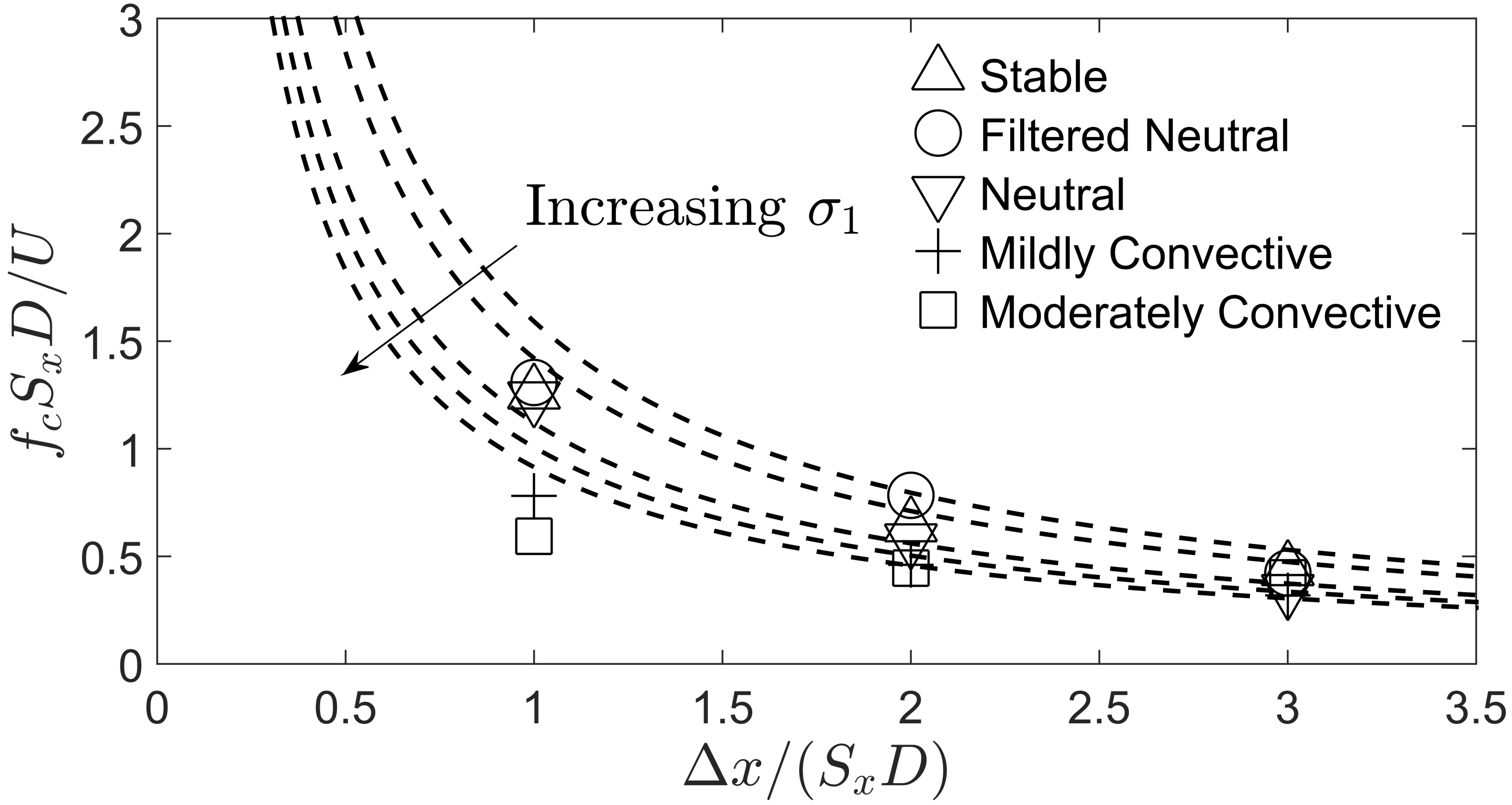

Figure 5.4: Mean least-squares estimate of f_c for all flow cases. Dashed lines show RSH predictions for the different flow cases, with the indicated dependence trend on σ_1, the standard deviation of streamwise velocity.

$$C_{1,2} \propto \frac{I_0}{\sqrt{I_0^2 + I_+^2}}, \tag{5.13}$$

which is a natural prediction for the coherence scaling factor a. Though the turbulence of the incoming boundary layers was measured during the simulations, the turbulence approach each turbine was not. We therefore rely on the empirical formulation of Crespo et al. [34] for the wake-added turbulence,

$$I_+ = 0.73a^{0.8325} I_0^{0.0325} (x/d)^{-0.32}, \tag{5.14}$$

to predict the turbulence intensity approaching each row of turbines in the five stability cases. We then model the coherence scaling factor $C_0^{i,j}$ for turbines i and j as

$$C_0^{i,j} = \frac{I_i}{I_j}, \tag{5.15}$$

where turbine i is assumed to be farther upwind. The measured values of C_0 for turbine pairs that have no lateral separation are depicted in Figure 5.5, showing adequate agreement with predictions. Although the similarity of layout among the five cases allows for direct testing of the change in coherence scaling factor between flow cases, the noise in these measurements does not allow for a statistically significant trend to be shown toward higher coherence with larger atmospheric turbulence. However, the clear trend in Figure 5.5 suggests the following approximate functional dependence of the coherence scaling factor on boundary-layer turbulence intensity:

$$C_0 = \frac{I_0}{\left(I_0^2 + (0.73a^{0.8325} I_0^{0.0325} (x/d)^{-0.32})^2\right)^{1/2}}. \tag{5.16}$$

This dependence is shown plotted for a pair of turbines separated by 5 rotor diameters for several axial induction factors, from 0.1 to 0.3, over a range of turbulence intensity values in Figure 5.6.

Although the turbulence model of Crespo and Hernandez [34] adequately predicts the coherence scaling factor, it should be noted that other wake-added turbulence models are commonly used in the literature as well.

5.6 Conclusion

Large-eddy simulations are used to show the impact of atmospheric stability on turbine-turbine power coherence. By fitting the data to a predicted coherence function based on the random-sweeping hypothesis, characteristic time scales are deduced, and deviations from the RSH predicted are attributed to wake motions. Results suggest that power coherence can be largely attributed to large-scale atmospheric motions, and that wake-added turbulence does not lead

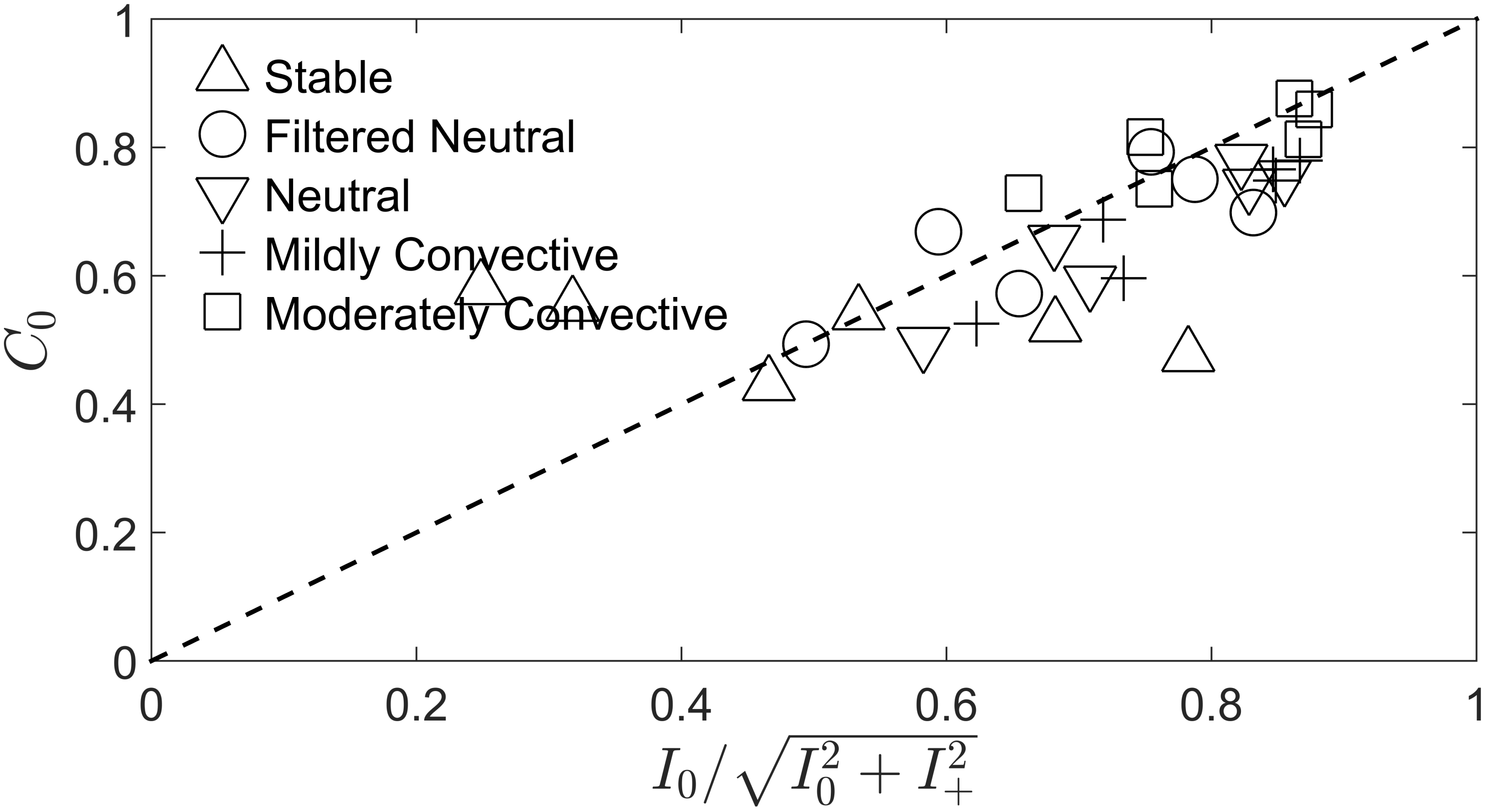

Figure 5.5: Coherence scaling factor vs. expected fraction of coherent turbulence intensity.

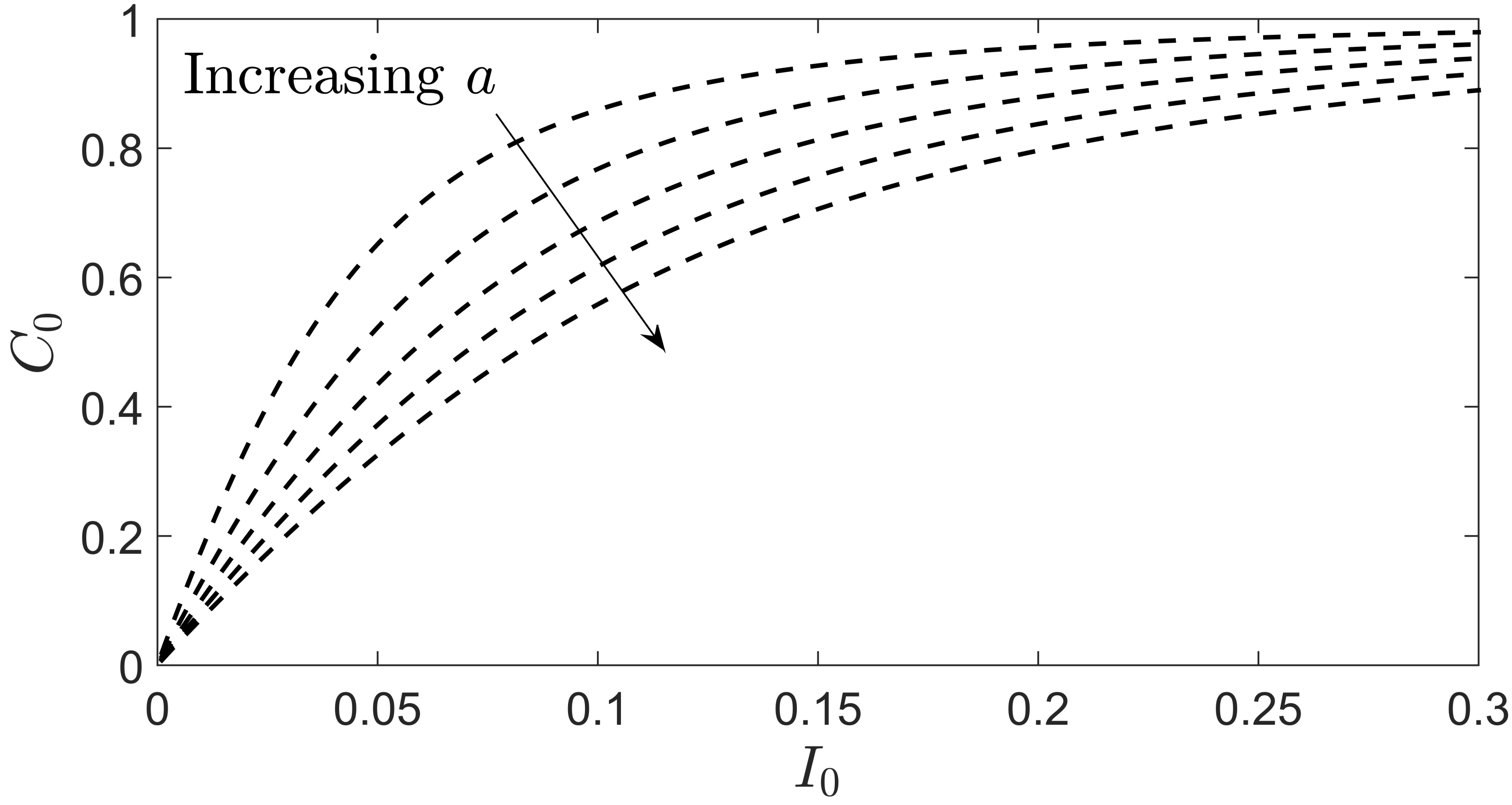

Figure 5.6: Predicted coherence scaling factor vs. boundary-layer turbulence intensity.

to correlations between turbines. This result is used to create an empirical prediction between the ambient atmospheric turbulence and the axial induction factor and spacing of the turbines. This empirical relation fits well with the LES data, suggesting that the dependence of power coherence on the atmospheric stability is primarily a matter of turbulence intensity.

Chapter 6

Modulation of Turbulence Scales Passing Through the Rotor of a Wind Turbine

6.1 Abstract

The modulation of boundary-layer turbulence across scales by passage through the rotor of a model wind turbine is assessed experimentally using synchronous upwind and downwind hotwire anemometers. Consistent with literature, results show that the rotor simultaneously eliminates large-scale motions, and introduces comparatively small-scale flow structures. The synchronous data allows for the distinct quantification of added and dampened turbulence by considering the temporal correlation between upwind and downwind time series. The destroyed turbulence is of a larger characteristic length scale than the created turbulence, but both scales increase with downwind distance. The intensity of the destroyed turbulence does not change substantially with downwind distance, suggesting that the turbine has a much stronger effect on turbulence destruction than simple natural evolution. The cross spectra between upwind and downwind velocity measurements suggest a dispersion relation for different time scales. In the near wake, lower-frequency components appear to be advected at velocity lower than the local wake velocity, and this advection velocity asymptotically approaches the local velocity at high frequency. This trend diminishes in magnitude with downwind distance.

6.2 Introduction

The turbulent nature of the atmospheric boundary layer is one of the most technically challenging aspects of wind power. The interactions between wind farms and the atmosphere have been under investigation for decades, as consideration of this interplay is essential for the development of well-engineered, cost-effective wind farms. The turbulent environment in the vicinity of a wind farm plays an integral role in the characteristics of wind-power variability across scales [3, 5, 77], dictates the design loads for the turbines used in the wind farm [109], and re-energizes the low-momentum wake regions within wind farms [15]. However, the ambient turbulence is significantly impacted by turbine wakes, which have been shown to introduce as well as attenuate turbulent scales [24], leading to a new equilibrium state for the flow within wind farms [78], and even to distinct boundary-layer physics in the limit of very large wind farms [16].

Due to the contribution of wakes to power deficits, dynamic loading, and downward kinetic energy flux, the turbulence characteristics of wake motions are of major importance to wind-farm performance as they contribute in ways that are distinct from the atmospheric boundary layer turbulence. For instance, wake meandering plays an important role in defining the turbulence scales that impact turbines within a wind farm, and is characterized by energetic far-wake motions at a Strouhal number $St = f_s D/U_{hub} \simeq 0.1 - 0.3$, where f_s is the meandering frequency, D is the turbine diameter, and U_{hub} is the mean hub-height velocity [92]. Two hypotheses exist to explain the onset of wake meandering; some authors [50] have found that small-scale vortices in the wake shear layer interact with the hub vortex to lead to large-scale wake meandering, which is consistent with the observations that meandering frequency scales with the Strouhal number [25, 92] and is, therefore, defined by the length scales of the turbine. A competing interpretation of wake meandering considers that this phenomenon is primarily driven by large-scale atmospheric turbulence; it is based on the model of [73], which treats the wake deficit as a passive tracer that is advected by the ambient turbulence, and benefits from field-scale experimental validation [11, 125].

Significant efforts have gone toward applying insights of wake dynamics to wind-farm optimization, including wake steering and the use of heterogeneous turbines in an array to minimize the exposure of downwind turbines to the wakes of upwind ones. Among several other method of wake control, Fleming *et. al.* [38] numerically investigated intentional yaw misalignment in the upwind turbine of a pair to deflect the wake laterally, and found this to be an effective method of increasing combined power. Yawed wake steering has been experimentally applied at the Scaled Wind Farm Technology (SWiFT) site in Lubbock, Texas [39], as well as in a commercial offshore wind farm in China [40], both showing good agreement with theoretical and numerical predictions. In an effort to similarly reduce wake effects, Chamorro *et. al.* [23] presented wind-tunnel measurements of a wind farm with alternating rows of two differently sized wind turbines, and showed a decrease in turbulence in the vicinity of turbine rotors. Vasel-Be-Hagh and Archer [127] presented an optimization paradigm based on collectively optimizing wind-farm power by changing the hub heights of turbines in a wind farm, validated the simple engineering approach with large-eddy simulations, and showed that power increases on the order of 2% are possible. Xie *et. al.* [135] similarly showed that there are benefits to collocating small vertical-axis wind turbines in an array of larger horizontal-axis turbines, also showing a significant increase in wind-farm energy production.

The role of wake-added turbulence to wind-farm dynamics is undoubtedly an important one, so that wake turbulence is commonly modeled for engineering applications. This is typically done by modeling the so-called wake-added turbulence intensity I_+, defined such that

$$I_{wake}^2 = I_0^2 + I_+^2, \tag{6.1}$$

where I_{wake} is the turbulence intensity in the wake, and I_0 is the approaching turbulence intensity. Several empirical methods of modeling I_+ exist [34, 47, 74, 28]. However, this simplistic approach does not inform the modulation of length scales in the wake turbulence, and is inconsistent with the observation of Chamorro *et. al.* [24] that the turbulence in a wake not only has an increased energy in the relatively high-frequency part of its spectrum, but also a reduction in the low-frequency range. It also may be inappropriate when considering the power variability of the aggregate power output of a wind farm, as covariance between turbine pairs is impacted by large-scale coherent motions [77, 13], which may be altered by turbines. An appropriate model may then be expressed as follows:

$$I_{wake}^2 = I_0^2 + I_+^2 - I_-^2, \tag{6.2}$$

where I_- is the wake-suppressed turbulence intensity. Separately characterizing the two would therefore be more consistent with previous observations of dampened large-scale motions. The goal of this work is to provide such a characterization via experimental investigation of wake-added and wake-suppressed motions. This is done with synchronous measurements of the flow right upwind and downwind of the turbine using hotwire anemometry, which allows for a statistical characterization of their respective energy content. Details of the experiments are outlined in Section 6.3, the methods of analysis and results are provided in Section 6.4, and concluding remarks are included in Section 6.5.

6.3 Experimental Setup

A model wind turbine was placed and operated in the eiffel-type wind tunnel of the Renewable Energy and Turbulent Environment Group at the University of Illinois. The test section of the wind tunnel is 6.1 m in length, 0.46 m high, and 0.91 m wide. The turbine had a hub height $z_{hub} = 0.125$ m, a rotor diameter $d_T = 0.12$ m, and operated at a tip-speed ratio $\lambda = 0.5 d_T \Omega / U_{hub} = 5.0$, where Ω is the rotational velocity in rad s^{-1}, with power and thrust coefficient of 0.45 and 0.79, respectively. The turbine is based on a reference model designed at Sandia National Laboratory [107, 59].

The incoming boundary layer was developed over a low-roughness wall, which was tripped at the inlet of the test section with a series of vertical strakes. This led to a boundary layer thickness $\delta / d_T \approx 2.4$, a friction velocity $u_* = 0.313$ m s^{-1}, a roughness height $z_0 = 0.024$ mm, and a hub-height velocity $U_{hub} = 6.61$ m s^{-1}. Strakes located at the inlet of the test section induced a turbulence structure with a well-defined inertial subrange that spanned over two orders of magnitude. The mean velocity and turbulence intensity profiles, as well as the power spectrum of the hub-height velocity, are illustrated in figure 6.1.

Velocity measurements were made with two synchronous hotwire anemometers.

Velocity sampling was performed one rotor diameter upwind of the center of the turbine's rotor, as well as at downwind distances ranging from 1.0 to 5.0 rotor diameters, incremented by 0.5 rotor diameters, and 6.0 to 10.0 rotor diameters, incremented by 1.0 rotor diameters, for a total of 14 synchronous upwind/downwind velocity time series measurements. Velocities were sampled at a rate of 1 kHz for a duration of 300 s. Identical synchronous time series were made without the turbine present. A schematic of the experimental setup is shown in Figure 6.2.

6.4 Analysis

Using the synchronous upwind and downwind time series, the change in the velocity spectra is decomposed into its added and destroyed components. Concretely, the coherent output power spectrum Φ_{cop} of the downwind point is calculated.

$$\Phi_{cop}(f) = C_{1,2}(f)\Phi_2(f), \tag{6.3}$$

where $C_{1,2}$ is the magnitude-squared coherence of the two signals, and Φ_2 is the power spectrum of the downwind signal. The magnitude-squared coherence is defined as,

$$C_{1,2}(f) = \frac{|\Phi_{1,2}(f)|^2}{\Phi_1(f)\Phi_2(f)}, \tag{6.4}$$

where $\Phi_{1,2}$ is the cross-spectral density of the upwind and downwind point, and Φ_1 is the power spectrum of the upwind point. The magnitude-squared coherence is a statistic that quantifies the causality between two signals. In the particular case of the upwind and downwind velocity measurements, it is a measure of how correlated velocity fluctuations at different time scales. A coherence value different than unity indicates that the turbulence at the two points is not perfectly correlated, which could come as a result of normal vortex stretching, or from the generation of turbulent scales by some other process, such as tip-vortex breakdown in the wake of a turbine [76]. Examples of the upwind, downwind, and coherent downwind power spectra are shown in Figure 6.3 with and without a turbine present. The data presented come from the closest downwind measurement location.

Several notable observations can be made of the spectra presented in Figure 6.3. Without the turbine present, the upwind, downwind, and downwind coherent spectra overlap closely in the low frequencies, suggesting that large-scale

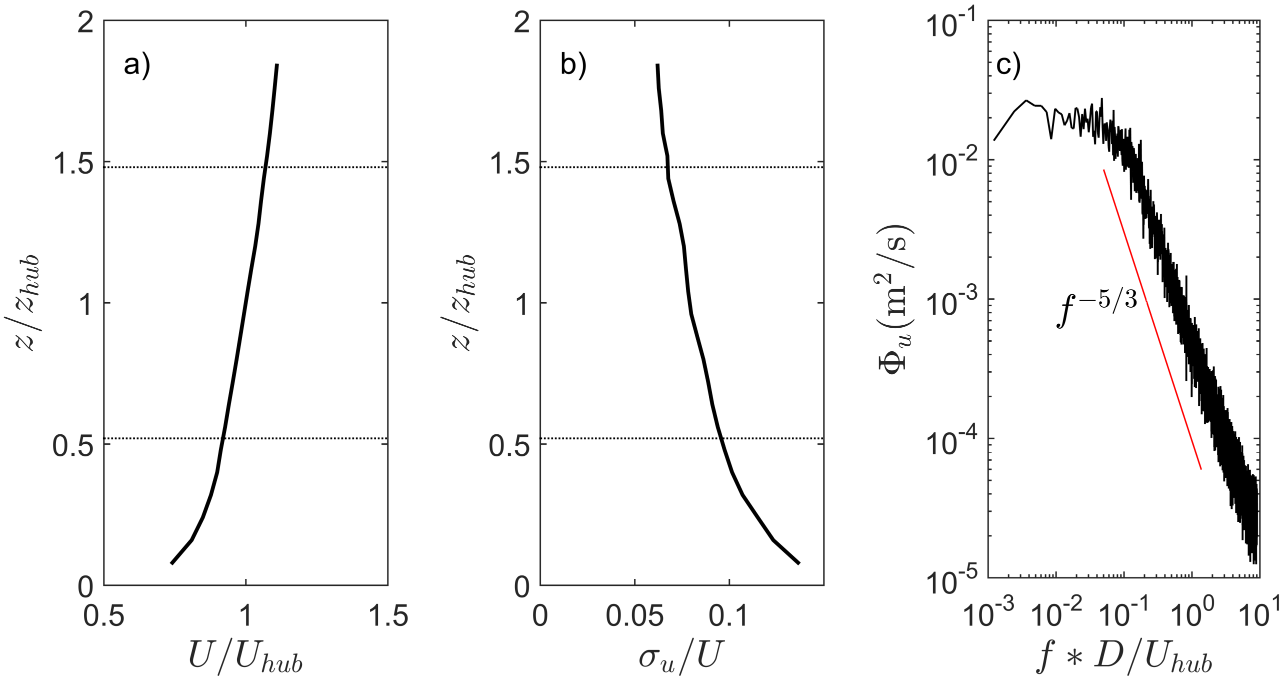

Figure 6.1: Characteristics of the incoming boundary layer; a) mean velocity profile, b) turbulence intensity, c) power spectrum of streamwise velocity component.

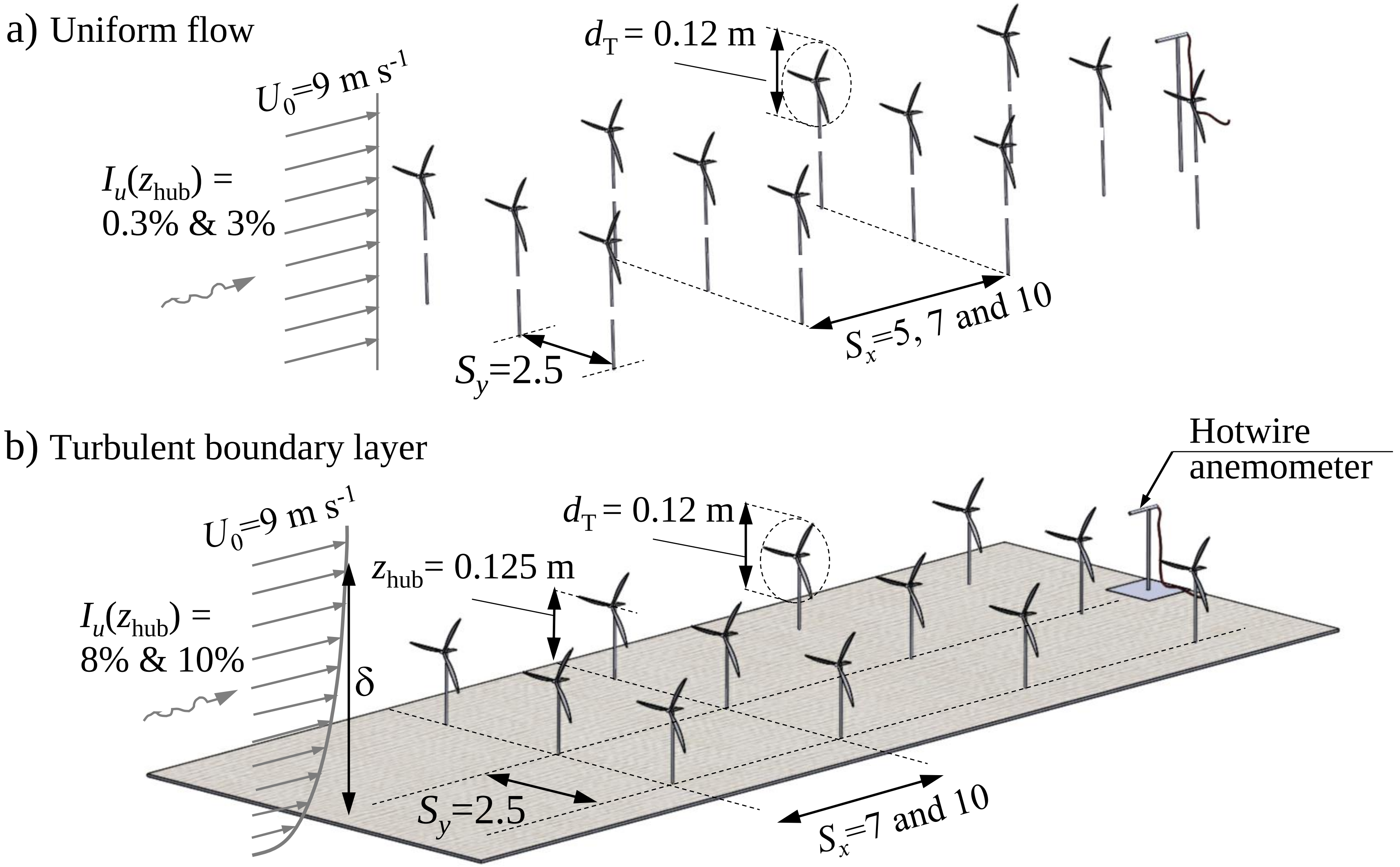

Figure 6.2: Basic schematic of the experimental setup illustrating the synchronized flow measurements upwind and downwind of the model turbine using two hotwire anemometers.

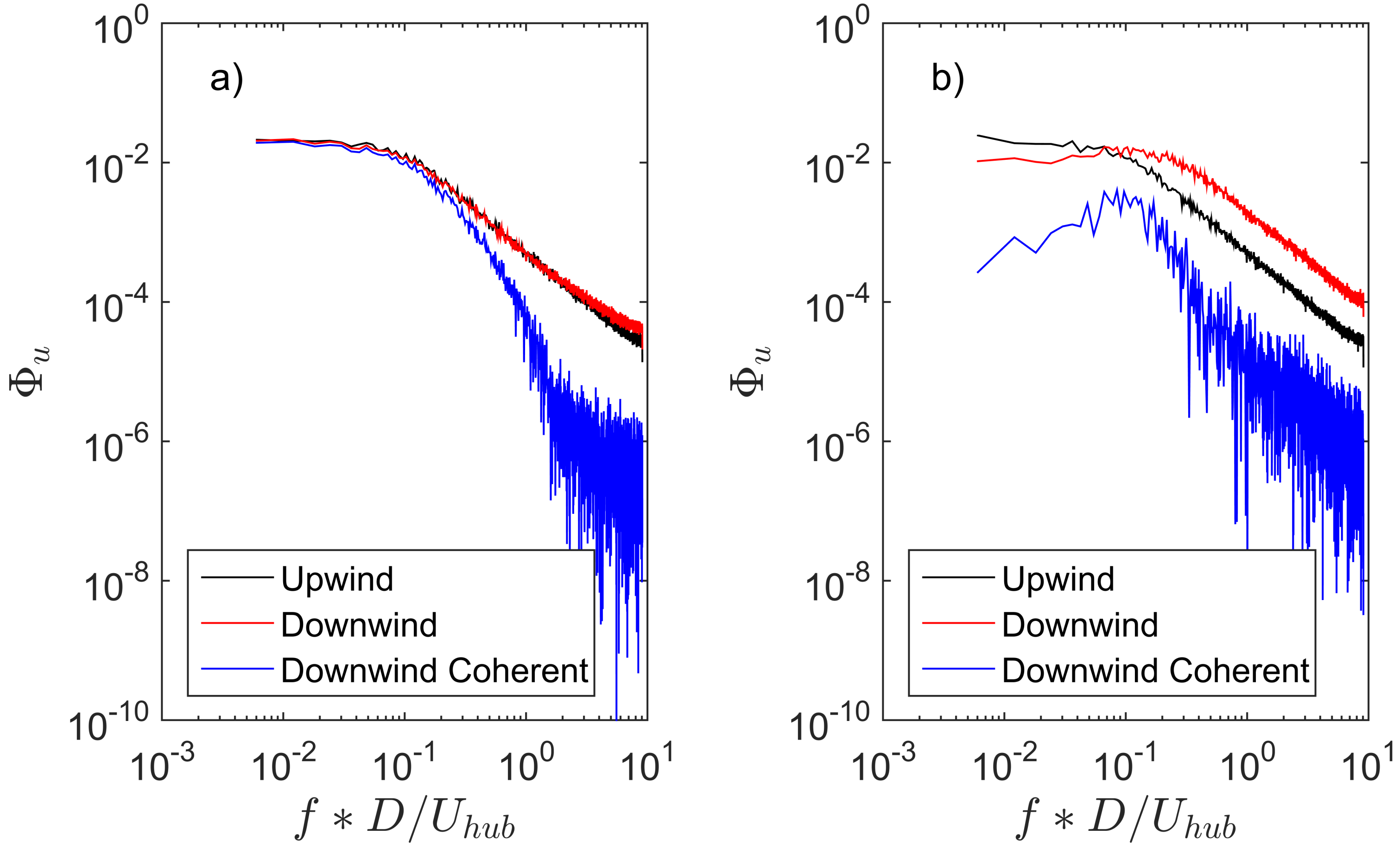

Figure 6.3: Upwind, downwind, and downwind coherent velocity spectra: a) without turbine present; b) with turbine present.

motions simply advect downwind without being strongly distorted. However, in the relatively high frequencies, the downwind coherent spectrum deviates significantly from the other two, suggesting that the high-frequency downwind motions have evolved significantly in the short distance between the two points. This could either be due to normal turbulent evolution, or from modulation by the hotwire structure. In the low-frequency region of Figure 6.3 b), the downwind energy content is reduced, consistent with previous results [24]. However, the downwind coherent spectrum has a significantly reduced magnitude compared to the downwind spectrum. This result can be interpreted as suggesting either that the large scales approaching a turbine are broadly destroyed and replaced by new motions shed from the turbine, or are distorted to the point of being only weakly correlated with their original state. At relatively high frequencies , there is a net increase in turbulence energy, again consistent with previous works [24]. The frequency at which the energy content is higher, $f * D/U_{hub} \approx 0.1$, is consistent with a turbulent cascade from large-scale motions due to wake meandering, which has been observed to occur at $St \approx 0.1 - 0.3$. With the two distinct processes of destruction of large-scale motions and introduction of meandering motions, we define the destroyed (Φ_-) and added (Φ_+) power spectra as

$$\Phi_- = \Phi_1 - \Phi_{cop}, \tag{6.5}$$

$$\Phi_+ = \Phi_2 - \Phi_{cop}, \tag{6.6}$$

so that $\Phi_2 = \Phi_1 - \Phi_- + \Phi_+$. The premultiplied wake-added power spectra are shown in Figure 6.4 varying with downwind distance. As seen in this Figure, the wake-added motions are predominantly in the frequency range of $F * D/U_{hub} \approx$ 0.1 - 0.5, again consistent with the interpretation that wake-added motions are primarily due to meandering. The slight trend toward higher energy content at lower frequencies with downwind distance is in agreement with the interpretation that wake meandering is due to the growth of small-scale vortices into larger structures.

Figure 6.5 similarly shows the premultiplied wake-destroyed power spectra. The frequency of maximum motion destruction does not change appreciably with distance, though there does appear to be a trend toward greater total energy destruction. The frequency of greatest energy destruction is also noticeably lower than that of energy creation.

With Φ_+ and Φ_- defined and calculated from the data, bulk statistics of the created and destroyed turbulence may be calculated. For instance, the increase/decrease of velocity variance can be calculated as:

$$\sigma^2_{+,-} = \int_0^\infty \Phi_{+,-}(f)df. \tag{6.7}$$

The integral time scale of the added or destroyed turbulence can also be

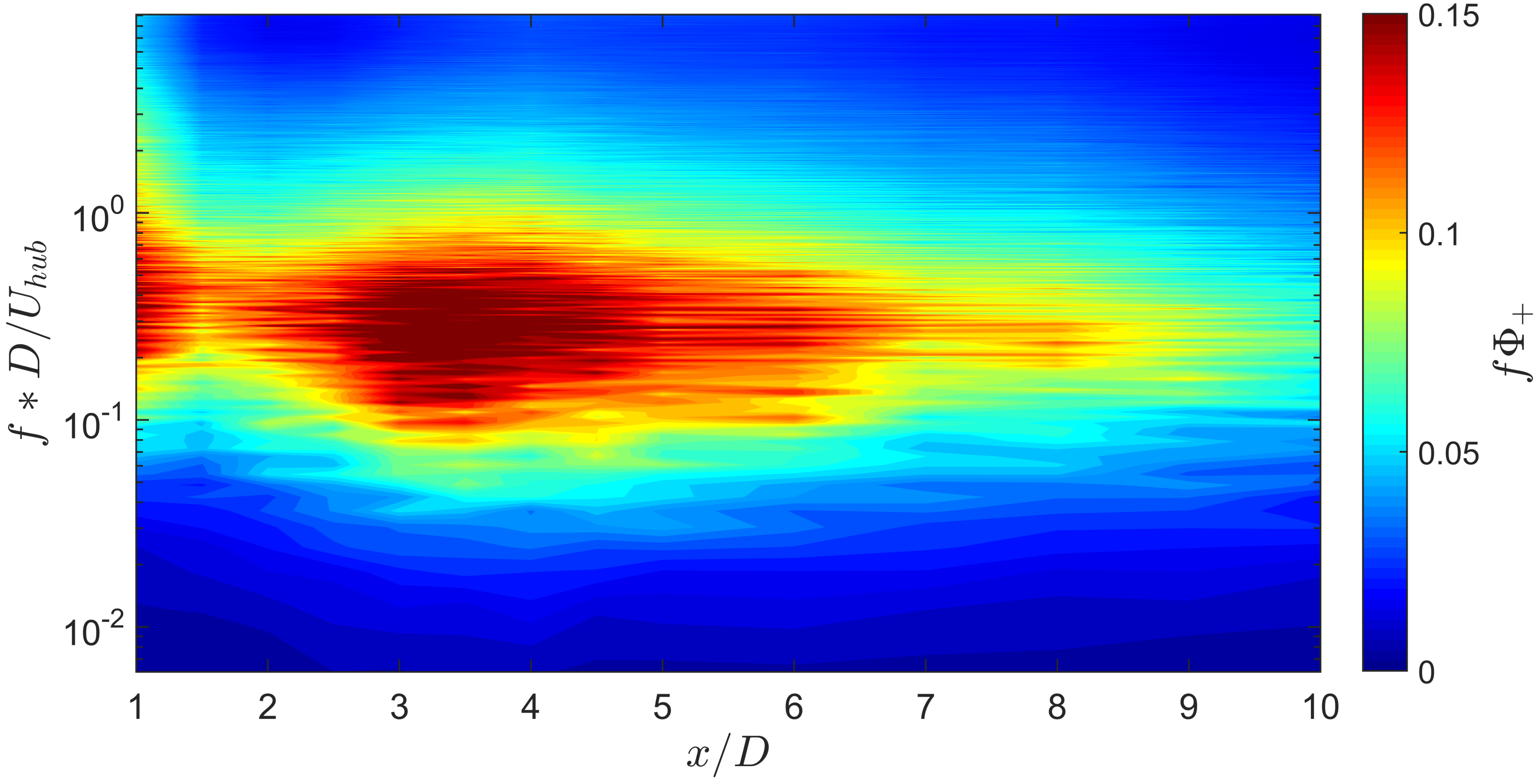

Figure 6.4: The premultiplied wake-added power spectrum with downwind distance.

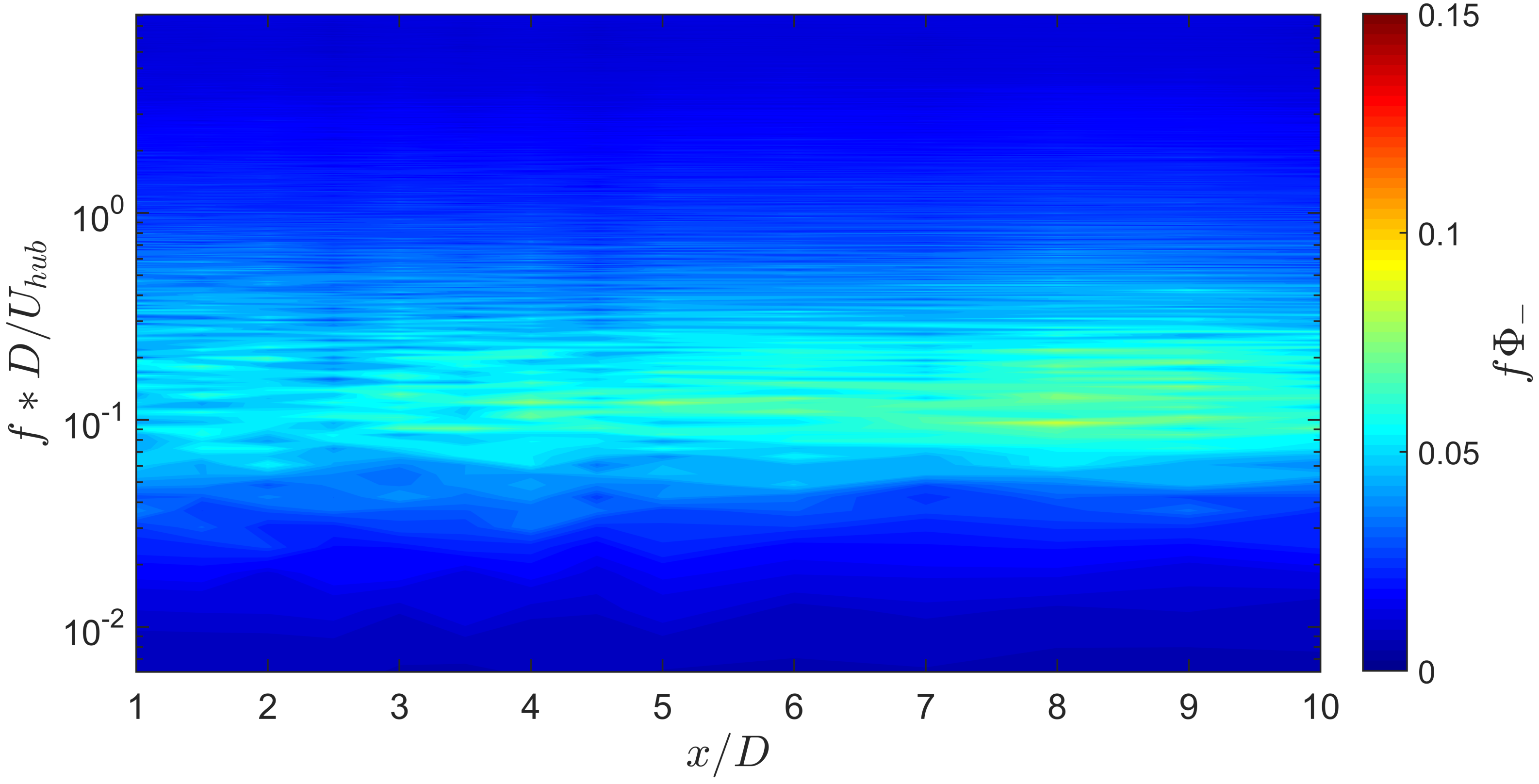

Figure 6.5: The premultiplied wake-destroyed power spectrum with downwind distance.

calculated as

$$T_{+,-} = \frac{\int_0^\infty f^{-1} \Phi_{+,-} df}{\int_0^\infty \Phi_{+,-}}. \tag{6.8}$$

The turbulence intensity and integral time scales of the added and destroyed turbulence show some interesting trends, and are plotted in Figure 6.6 and 6.7. As seen in Figure 6.6, the turbine-destroyed turbulence does not appreciably increase with downwind distance. It does, however, appear to decrease in integral time scale as seen in Figure 6.7. These combined results are interesting, and may be explained as large-scale, correlated boundary-layer motions impinging into the wake while smaller-scale motions nonlinearly interact and become distorted and incoherent. The turbine-added turbulence intensity displays an interesting trend. Between $1.0D$ and $1.5D$, a significant decrease occurs, followed by a subsequent increase until $3.5D$, with a monotonic decrease afterwards. The turbine-added integral time scale quickly increases between $1.0D$ and $2.5D$, with a slow upward trend after $2.5D$. These may both be explained by the findings of Howard et al. [50] that far-wake meandering motions are triggered by the near-wake hub vortex, and grow with downwind distance. The near-wake decrease in turbulence intensity is then consistent with the decay of the hub vortex, followed by the growth of meandering motions that decay in intensity and grow in length scale.

The synchronous velocity measurements also allow for an investigation of a possible dispersive effect for the spectral energy content. Applying Taylor's frozen turbulence hypothesis to a pair of points, one directly downwind of the other, an expression can be derived for the phase angle of the cross-spectrum of the velocity time series of the two points. The frozen turbulence hypothesis makes the assumption that turbulent motions are advected by the mean velocity U as,

$$\frac{\partial u'}{\partial t} + U \frac{\partial u'}{\partial x} = 0. \tag{6.9}$$

Taking the Fourier transform of this relation results in an ordinary differential equation for $\hat{u}(f, x)$, the Fourier transform of the velocity fluctuations. Solving this equation gives an expression for the cross spectral density of the two points as,

$$\Phi_{1,2} = \Phi_1 \exp\left(\frac{-2\pi i f x}{U}\right), \tag{6.10}$$

so that the phase angle θ of the cross-spectrum is predicted to be equal to $-2\pi f x/U$. Measured phase angles different from these values would therefore indicate a dispersion of the velocity scales passing through the turbine's rotor. We therefore define a dispersion velocity $\hat{U}$ as

$$\hat{U} = -\frac{2\pi f x}{\theta}. \tag{6.11}$$

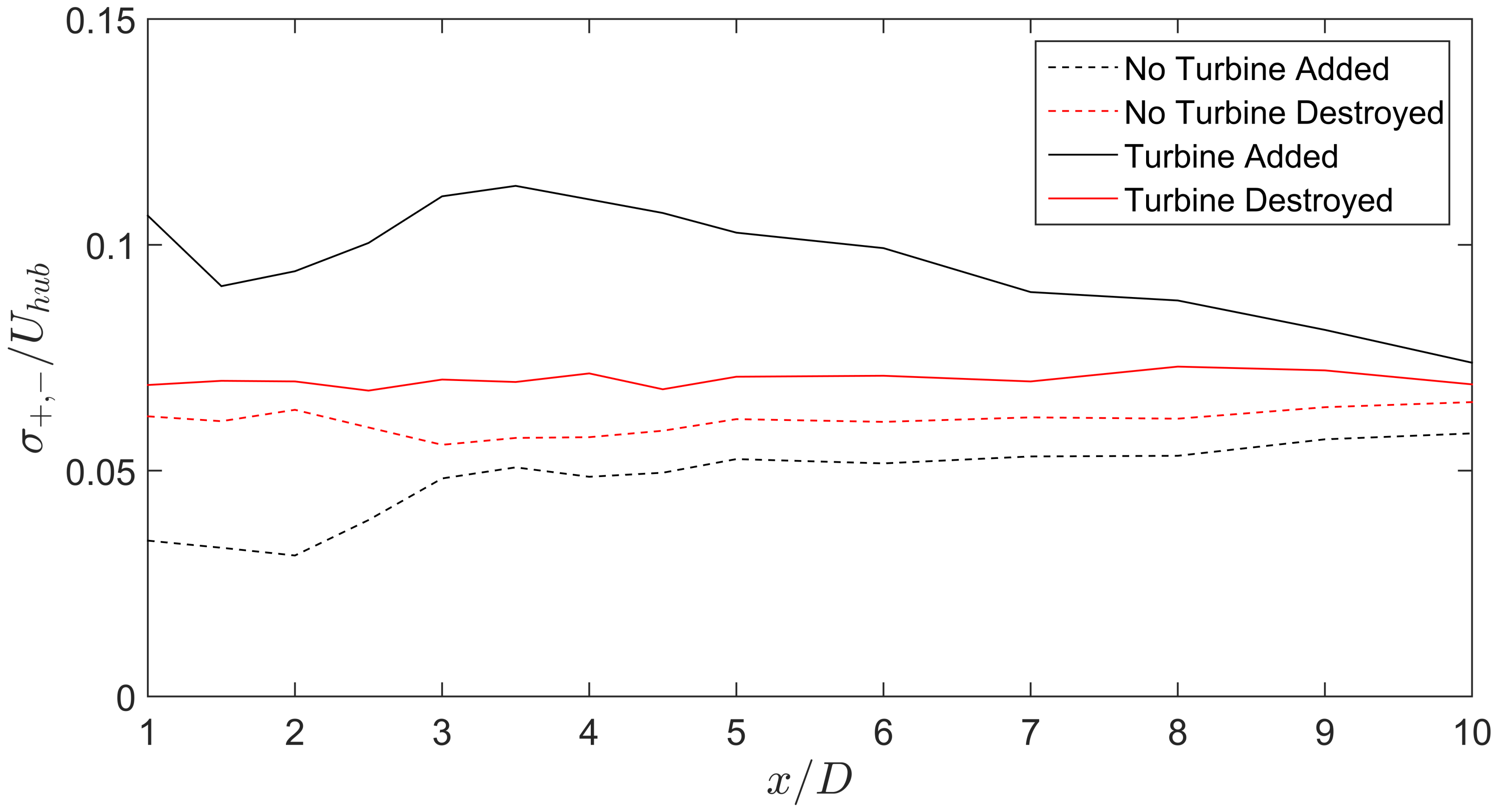

Figure 6.6: Evolution of added and destroyed turbulence intensity with downwind distance.

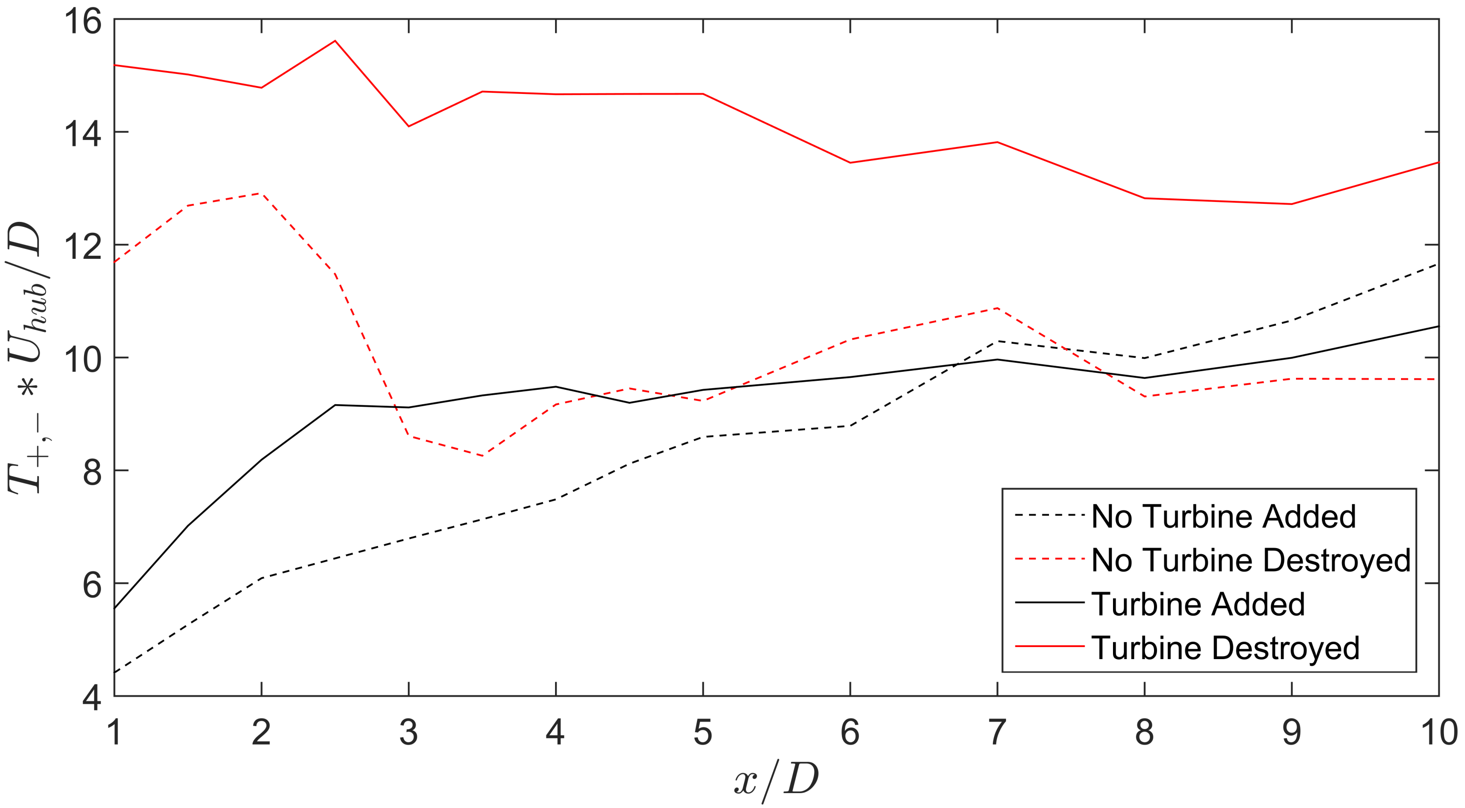

Figure 6.7: Evolution of added and destroyed integral time scale with downwind distance.

This dispersion velocity is shown plotted, normalized by the local mean velocity, in Figure 6.8. In this Figure, the dispersion velocity of the nearest measurement in shown in red, and the lines become bluer with greater distance downwind of the turbine. There appears to be a tendency in the near wake for the low frequencies to be advected at a frequency lower than the local velocity, an effect which disappears with greater downwind distance. The lower dispersion velocity in the near-wake low-frequency components is an interesting result, though the tendency toward the local mean velocity with greater distance is again consistent with the interpretation that large-scale motions impinge into the wake far downwind and re-introduce correlated large-scale motions.

6.5 Concluding Remarks

The modulation of turbulent motions by wind turbines is an immensely complex problem, with important implications in power variability, turbine design, and grid integration. Particularly for matters of power variability, it appears to be important to make a more thorough distinction between the different components of the turbulence in the wake, as wakes have a profound impact on the spatio-temporal correlations in the atmospheric boundary layer in which they are immersed. However, we stress that this work is largely exploratory, and an investigation of the spatio-temporal correlations within a large wind farm, which may operate in turbulent environments different than the current one, may be warranted.

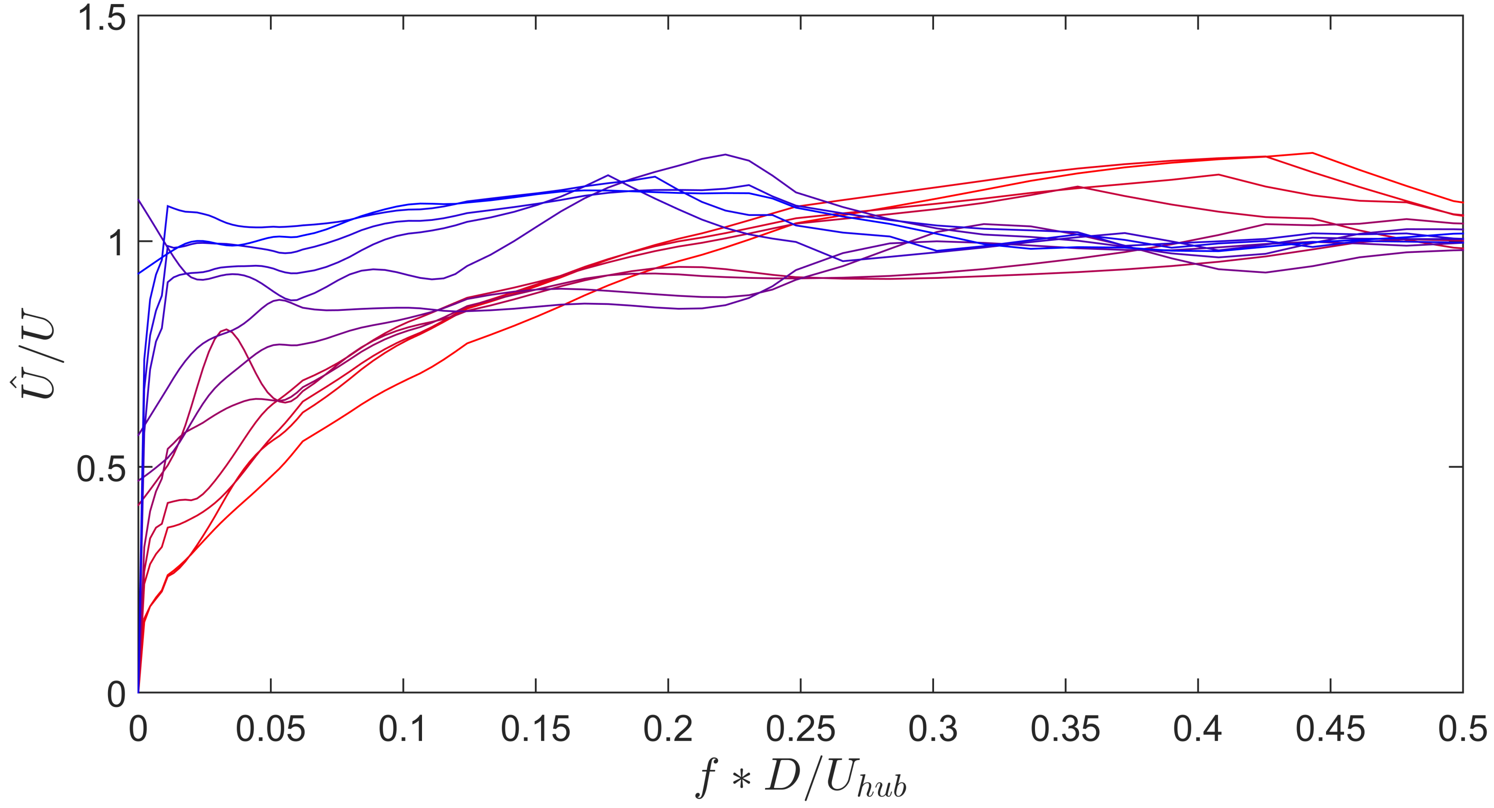

Figure 6.8: Conceptual schematic freestream experiments.

Chapter 7

Conclusions and Future Directions

7.1 Conclusions

Possibly the most important challenge in integrating renewable sources of energy such as wind power into electrical grids is their variability. The variability of wind power occurs over an extremely wide range of spatial and temporal scales, with the fluctuations at different time scales associated with different integration costs. Over relatively short time scales, power fluctuations are inextricably linked to atmospheric turbulence. The linkage between turbulence and power variability is a complex, two-way exchange. It is quite useful to treat turbines as simply sampling the boundary layer in which they operate, though caveats and weaknesses of this assumption are important. Like any probe, the operation of the turbine impacts the scales over which the probing behavior is valid, with high-frequency filtering due to rotor inertia and the control schemes of the turbine. Also, the role that wakes play on the modulation of the boundary layer within a wind farm is an unavoidable complication. Wakes change the spatiotemporal scales and the turbulent energy content approaching turbines in an array, so that the characteristics of their power fluctuations are significantly altered. The wake-added motions also appear to be nearly uncorrelated with the upwind motions, so that a significant component of the power fluctuations of turbines deep within a wind farm do not have significant cross-correlation with other turbines. This leads to conspicuous alterations of the characteristics of turbine-turbine correlations at different times of the day, depending on the stability state of the atmosphere. The addition of uncorrelated motions is also complicated by the destruction of correlated motions by a spinning wind turbine, and the fact that the statistics of the changes are strong functions of location, particularly within the wake.

7.2 Unaddressed Topics

Many aspects of the physics governing wind-power variability are still quite unclear, and some important phenomena warrant investigation. One of the major simplifying assumptions made throughout all the analysis performed in this thesis is that the wind field is steady-on-average. However, this assumption may become stressed in a real atmospheric boundary layer, where the wind speed and direction are constantly changing, and events such as ramping can occur. It would therefore be interesting to consider how the analysis may change, or how the predictive ability of the framework detailed in this thesis would break down in a non-steady environment. The precise role of wakes is also still elusive. Much of the analysis of wakes in this work is either observational or semi-empirical. It would therefore be interesting to attempt to derive some treatment for the modulation of turbulence with a stronger grounding in first principles.

References

[1] U.S. wind industry annual market report. Technical report, American Wind Energy Association. 2013a (2013).

[2] R. J. Adrian, C. D. Meinhart, and C. D. Tomkins. Vortex organization in the outer region of the turbulent boundary layer. *J. Fluid Mech.*, 422: 1–54, 2000.

[3] Jay Apt. The spectrum of power from wind turbines. *Journal of Power Sources*, 169(2):369–374, 2007.

[4] Cristina L Archer and Mark Z Jacobson. Supplying baseload power and reducing transmission requirements by interconnecting wind farms. *Journal of Applied Meteorology and Climatology*, 46(11):1701–1717, 2007.

[5] Mahesh M Bandi. Spectrum of wind power fluctuations. *Physical review letters*, 118(2):028301, 2017.

[6] T. K. Barlas and ban Kuik G. A. M. Review of state of the art in smart rotor control research for wind turbines. *Prog. Aerosp. Sci.*, 46.1:1–27, 2010.

[7] Rebecca Barthelmie, Gunner Larsen, Sara Pryor, Hans Jørgensen, Hans Bergström, Wolfgang Schlez, Kostas Rados, Bernhard Lange, Per Vølund, Søren Neckelmann, et al. Endow (efficient development of offshore wind farms): modelling wake and boundary layer interactions. *Wind Energ.*, 7 (3):225–245, 2004.

[8] Rebecca Jane Barthelmie, Sten Tronæs Frandsen, MN Nielsen, SC Pryor, P-E Rethore, and Hans Ejsing Jørgensen. Modelling and measurements of power losses and turbulence intensity in wind turbine wakes at middelgrunden offshore wind farm. *Wind Energy*, 10(6):517–528, 2007.

[9] Majid Bastankhah and Fernando Porté-Agel. A new analytical model for wind-turbine wakes. *Renew. Energ.*, 70:116–123, 2014.

[10] Fernando D Bianchi, Hernan De Battista, and Ricardo J Mantz. *Wind turbine control systems: principles, modelling and gain scheduling design.* Springer, 2006.

[11] Ferhat Bingöl, Jakob Mann, and Gunner C Larsen. Light detection and ranging measurements of wake dynamics part i: one-dimensional scanning. *Wind Energy: An International Journal for Progress and Applications in Wind Power Conversion Technology*, 13(1):51–61, 2010.

[12] Juliaan Bossuyt, Michael F Howland, Charles Meneveau, and Johan Meyers. Measurement of unsteady loading and power output variability in a micro wind farm model in a wind tunnel. *Exp Fluids*, 58(1):1, 2017.

[13] Juliaan Bossuyt, Charles Meneveau, and Johan Meyers. Wind farm power fluctuations and spatial sampling of turbulent boundary layers. *Journal of Fluid Mechanics*, 823:329–344, 2017.

[14] Tony Burton, Nick Jenkins, David Sharpe, and Ervin Bossanyi. *Wind energy handbook*. John Wiley & Sons, 2011.

[15] Raúl Bayoán Cal, José Lebrón, Luciano Castillo, Hyung Suk Kang, and Charles Meneveau. Experimental study of the horizontally averaged flow structure in a model wind-turbine array boundary layer. *Journal of Renewable and Sustainable Energy*, 2(1):013106, 2010.

[16] Marc Calaf, Charles Meneveau, and Johan Meyers. Large eddy simulation study of fully developed wind-turbine array boundary layers. *Physics of fluids*, 22(1):015110, 2010.

[17] Rudy Calif, François G Schmitt, and Yongxiang Huang. Multifractal description of wind power fluctuations using arbitrary order hilbert spectral analysis. *Physica A*, 392(18):4106–4120, 2013.

[18] P. Caselitz, W. Kleinkauf, T. Kruger, J. Petschenka, M. Reichardt, and K. Storzel. Reduction of fatigue loads on wind energy converters by advanced control methods. In *Proceedings of the European Wind Energy Conference*, pages 555–558, Dublin, 1998. Slane County Meath, Republic of Ireland : Irish Wind Energy Association.

[19] L. P. Chamorro and F. Porté-Agel. A wind-tunnel investigation of wind-turbine wakes: Boundary-layer turbulence effects. *Bound-lay Meteorol*, 132:129–149, 2009.

[20] L. P. Chamorro, R. E. A. Ardnt, and F. Sotiropoulos. Turbulent flow properties around a staggered wind farm. *Bound-Lay. Meteorol.*, 141: 349–367, 2011.

[21] L. P. Chamorro, S. J. Lee, D. Olsen, C. Milliren, J. Marr, R. E. A. Arndt, and F. Sotiropoulos. Turbulence effects on a full–scale 2.5 mw horizontal–axis wind turbine under neutrally stratified conditions. *Wind Energ.*, 18(2):339–349, 2015.

[22] Leonardo P Chamorro and Fernando Porté-Agel. Effects of thermal stability and incoming boundary-layer flow characteristics on wind-turbine wakes: a wind-tunnel study. *Bound-lay. Meteorol.*, 136(3):515–533, 2010.

[23] Leonardo P Chamorro, N Tobin, REA Arndt, and F Sotiropoulos. Variable-sized wind turbines are a possibility for wind farm optimization. *Wind Energy*, 17(10):1483–1494, 2014.

[24] LP Chamorro, M Guala, REA Arndt, and F Sotiropoulos. On the evolution of turbulent scales in the wake of a wind turbine model. *Journal of Turbulence*, (13):N27, 2012.

[25] LP Chamorro, C Hill, S Morton, C Ellis, REA Arndt, and F Sotiropoulos. On the interaction between a turbulent open channel flow and an axial-flow turbine. *Journal of Fluid Mechanics*, 716:658–670, 2013.

[26] LP Chamorro, C Hill, VS Neary, B Gunawan, REA Arndt, and F Sotiropoulos. Effects of energetic coherent motions on the power and wake of an axial-flow turbine. *Phys. Fluids.*, 27(5):055104, 2015.

[27] S. Chowdhury, J. Zhang, A. Messac, and L. Castillo. Unrestricted wind farm layout optimization (uwflo): Investigating key factors influencing the maximum power generation. *Renew. Energ.*, 38.1:16–30, 2012.

[28] Chia-Ren Chu and Pei-Hung Chiang. Turbulence effects on the wake flow and power production of a horizontal-axis wind turbine. *Journal of Wind Engineering and Industrial Aerodynamics*, 124:82–89, 2014.

[29] M. J. Churchfield, S. Lee, P. J. Moriarty, L. A. Martínez, S. Lonardi, Vijayakumar G., and J. G. Brasseur. A large-eddy simulation of wind-plant aerodynamics. In *50th AIAA Aerospace Sciences Meeting including the New Horizons Forum and Aerospace Exposition*, number AIAA 2012-0537, 2012.

[30] Matthew J Churchfield, Ganesh Vijayakumar, James G Brasseur, and Patrick J Moriarty. Wind energy-related atmospheric boundary layer large-eddy simulation using openfoam: Preprint. Technical report, National Renewable Energy Lab.(NREL), Golden, CO (United States), 2010.

[31] Matthew J Churchfield, Sang Lee, John Michalakes, and Patrick J Moriarty. A numerical study of the effects of atmospheric and wake turbulence on wind turbine dynamics. *Journal of turbulence*, 13:N14, 2012.

[32] Umberto Ciri, Mario Rotea, Christian Santoni, and Stefano Leonardi. Large-eddy simulations with extremum-seeking control for individual wind turbine power optimization. *Wind Energ.*, 2017.

[33] A. Crespo and J. Herna. Turbulence characteristics in wind turbine wakes. *J. Wind Eng. Ind. Aerod.*, 61(1):71–85, 1996.

[34] Antonio Crespo, J Hernandez, and Sten Frandsen. Survey of modelling methods for wind turbine wakes and wind farms. *Wind Energy: An International Journal for Progress and Applications in Wind Power Conversion Technology*, 2(1):1–24, 1999.

[35] J Cuxart and MA Jiménez. Mixing processes in a nocturnal low-level jet: An les study. *Journal of the atmospheric sciences*, 64(5):1666–1679, 2007.

[36] A. J. Eggers, R Digumarthi, and K. Chaney. Wind shear and turbulence effects on rotor fatigue and loads control. *J. Sol. Ener.-T. ASME*, 125(4): 402–409, 2003.

[37] Emily Fertig, Jay Apt, Paulina Jaramillo, and Warren Katzenstein. The effect of long-distance interconnection on wind power variability. *Environmental research letters*, 7(3):034017, 2012.

[38] Paul Fleming, Pieter MO Gebraad, Sang Lee, Jan-Willem van Wingerden, Kathryn Johnson, Matt Churchfield, John Michalakes, Philippe Spalart, and Patrick Moriarty. Simulation comparison of wake mitigation control strategies for a two-turbine case. *Wind Energy*, 18(12):2135–2143, 2015.

[39] Paul Fleming, Matt Churchfield, Andrew Scholbrock, Andrew Clifton, Scott Schreck, Kathryn Johnson, Alan Wright, Pieter Gebraad, Jennifer Annoni, Brian Naughton, et al. Detailed field test of yaw-based wake steering. In *Journal of Physics: Conference Series*, volume 753, page 052003. IOP Publishing, 2016.

[40] Paul Fleming, Jennifer Annoni, Jigar J Shah, Linpeng Wang, Shreyas Ananthan, Zhijun Zhang, Kyle Hutchings, Peng Wang, Weiguo Chen, and Lin Chen. Field test of wake steering at an offshore wind farm. *Wind Energy Science*, 2(1):229–239, 2017.

[41] Daniel Foti, Xiaolei Yang, Michele Guala, and Fotis Sotiropoulos. Wake meandering statistics of a model wind turbine: Insights gained by large eddy simulations. *Phy. Rev. Fluids.*, 1(4):044407, 2016.

[42] A. N. Fragoulis. The complex terrain wind environment and its effects on the power output and loading of wind turbines. In *1997 ASME Wind Energy Symposium*, number AIAA 97-0934, pages 33–40, 1997.

[43] S. T. Frandsen and M. L. Thøgersen. Integrated fatigue loading for wind turbines in wind farms by combining ambient turbulence and wakes. *Wind Eng.*, 23:327–339, 1999.

[44] Sten Frandsen, Rebecca Barthelmie, Sara Pryor, Ole Rathmann, Søren Larsen, Jørgen Højstrup, and Morten Thøgersen. Analytical modelling of wind speed deficit in large offshore wind farms. *Wind Energ.*, 9(1-2): 39–53, 2006.

[45] T. Göçmen, P. van der Laan, P. E. Réthoré, A. P. Diaz, G. C. Larsen, and S. Ott. Wind turbine wake models developed at the technical university of denmark: A review. *Renwe. Sust. Energ. Rev.*, 60:752–769, 2016.

[46] M Harris, M Hand, and A Wright. Lidar for turbine control. *National Renewable Energy Laboratory, Golden, CO, Report No. NREL/TP-500-39154*, 2006.

[47] Unsal Hassan. *A wind tunnel investigation of the wake structure within small wind turbine farms.* Harwell Laboratory, Energy Technology Support Unit, 1993.

[48] Jiarong Hong, Mostafa Toloui, Leonardo P Chamorro, Michele Guala, Kevin Howard, Sean Riley, James Tucker, and Fotis Sotiropoulos. Natural snowfall reveals large-scale flow structures in the wake of a 2.5-mw wind turbine. *Nature communications*, 5:4216, 2014.

[49] KB Howard, JS Hu, LP Chamorro, and M Guala. Characterizing the response of a wind turbine model under complex inflow conditions. *Wind Energ.*, 18(4):729–743, 2015.

[50] Kevin B Howard, Arvind Singh, Fotis Sotiropoulos, and Michele Guala. On the statistics of wind turbine wake meandering: An experimental investigation. *Physics of Fluids*, 27(7):075103, 2015.

[51] Ming-Chen Hsu, Ido Akkerman, and Yuri Bazilevs. Finite element simulation of wind turbine aerodynamics: validation study using nrel phase vi experiment. *Wind Energy*, 17(3):461–481, 2014.

[52] Hrvoje Jasak, Aleksandar Jemcov, Zeljko Tukovic, et al. Openfoam: A c++ library for complex physics simulations. In *International workshop on coupled methods in numerical dynamics*, volume 1000, pages 1–20. IUC Dubrovnik, Croatia, 2007.

[53] N. O. Jensen. A note on wind generator interaction. *Tech. rep., Ris-M-2411.*, 1983.

[54] Pankaj K Jha and Sven Schmitz. Blade load unsteadiness and turbulence statistics in an actuator-line computed turbine–turbine interaction problem. *Journal of Solar Energy Engineering*, 138(3):031002, 2016.

[55] Pankaj K Jha and Sven Schmitz. Actuator curve embedding–an advanced actuator line model. *Journal of Fluid Mechanics*, 834, 2018.

[56] Pankaj K Jha, Matthew J Churchfield, Patrick J Moriarty, and Sven Schmitz. The effect of various actuator-line modeling approaches on turbine-turbine interactions and wake-turbulence statistics in atmospheric boundary-layer flow. In *32nd ASME Wind Energy Symposium*, page 0710, 2014.

[57] Pankaj K Jha, Earl PN Duque, Jessica L Bashioum, and Sven Schmitz. Unraveling the mysteries of turbulence transport in a wind farm. *Energies*, 8(7):6468–6496, 2015.

[58] Yaqing Jin, Huiwen Liu, Rajan Aggarwal, Arvind Singh, and Leonardo P Chamorro. Effects of freestream turbulence in a model wind turbine wake. *Energies*, 9(10):830, 2016.

[59] Erick Johnson, Arnold A Fontaine, Michael L Jonson, Richard S Meyer, William A Straka, SA Young, CP van Dam, Henry Shiu, and Matthew Barone. A1: 8.7 scale water tunnel test of an axial flow water turbine. In *Proceedings of the 1rst Marine Energy Technology Symposium, METS13, Washington Dc*, Washington D.C., 2013. Foundation for Ocean Renewables.

[60] I Katic, J Højstrup, and Niels Otto Jensen. A simple model for cluster efficiency. In *European wind energy association conference and exhibition.* A. Raguzzi, 1987.

[61] Warren Katzenstein, Emily Fertig, and Jay Apt. The variability of interconnected wind plants. *Energy Policy*, 38(8):4400–4410, 2010.

[62] N. D. Kelley. Turbulence descriptors for scaling fatigue loading spectra of wind turbine structural components. 1994. Rep. NREL/TP-442-7035, prepared for the IEA Expert Meeting on Wind Conditions for Wind Turbine Design, Hamburg, Germany, June 2728, 1994, National Renewable Energy Laboratory, Colorado.

[63] N. D. Kelley. A case for including atmospheric thermodynamic variables in wind turbine fatigue loading parameter identification. 1999. Rep. NREL/CP-500-26829, National Renewable Energy Laboratory, Colorado.

[64] N. D. Kelley, B. J. Jonkman, G. N. Scott, and Pichugina Y. L. Comparing pulsed doppler lidar with sodar and direct measurements for wind assessment. 2007. NREL Report No. CP-500-41792, National Renewable Energy Laboratory.

[65] Samir Khanna and James G Brasseur. Three-dimensional buoyancy-and shear-induced local structure of the atmospheric boundary layer. *Journal of the atmospheric sciences*, 55(5):710–743, 1998.

[66] Andrey Nikolaevich Kolmogorov. The local structure of turbulence in incompressible viscous fluid for very large reynolds numbers. In *Dokl. Akad. Nauk SSSR*, volume 30, pages 299–303, 1941.

[67] C. Kong, J. Bang, and Y. Sugiyama. Structural investigation of composite wind turbine blade considering various load cases and fatigue life. *Energy*, 30.11-12:2101–2114, 2005.

[68] K. A. Kragh, M. H. Hansen, and T. Mikkelsen. Improving yaw alignment using spinner based LIDAR. In *49th AIAA Aerospace Sciences Meeting including the New Horizons Forum and Aerospace Exposition*, number AIAA 2011-264, 2011.

[69] Robert H Kraichnan. Kolmogorov's hypotheses and eulerian turbulence theory. *The Physics of Fluids*, 7(11):1723–1734, 1964.

[70] Robert H Kraichnan. Inertial ranges in two-dimensional turbulence. *Phys. Fluids.*, 10(7):1417–1423, 1967.

[71] J. Laks, L. Pao, A. Wright, N. Kelley, and B. Jonkman. The use of preview wind measurements for blade pitch control. *Mechatronics*, 21.4:668–681, 2011.

[72] L. Landberg. Short-term prediction of the power production from wind farms. *J. Wind Eng. Ind. Aerod.*, 80.1(1):207–220, 1999. ISSN 1099-1824.

[73] Gunner C Larsen, Helge Aa Madsen, Kenneth Thomsen, and Torben J Larsen. Wake meandering: a pragmatic approach. *Wind Energy: An International Journal for Progress and Applications in Wind Power Conversion Technology*, 11(4):377–395, 2008.

[74] Gunner Chr Larsen, Jørgen Højstrup, and H Aagaard Madsen. Wind fields in wakes. In *1996 European Wind Energy Conference and Exhibition*, pages 764–768. HS Stephens & Associates, 1996.

[75] A. W. Lavely, G. Vijayakumar, M. P. Kinzel, and J. G. Brasseur. Space-time loadings on wind turbine blades driven by atmospheric boundary layer turbulence. In *49th AIAA Aerospace Sciences Meeting Including the New Horizons Forum and Aerospace Exposition*, number AIAA 2011-635, 2011.

[76] LEM Lignarolo, D Ragni, F Scarano, CJ Simão Ferreira, and GJW van Bussel. Tip-vortex instability and turbulent mixing in wind-turbine wakes. *Journal of Fluid Mechanics*, 781:467–493, 2015.

[77] Huiwen Liu, Yaqing Jin, Nicolas Tobin, and Leonardo P Chamorro. Towards uncovering the structure of power fluctuations of wind farms. *Physical Review E*, 96(6):063117, 2017.

[78] Huiwen Liu, Imran Hayat, Yaqing Jin, and Leonardo P Chamorro. On the evolution of the integral time scale within wind farms. *Energies*, 11 (1):93, 2018.

[79] C. Luo, B. Shen, and B.T. Ooi. Strategies to smooth wind power fluctuations of wind turbine generator. *IEEE T. Energy Conver*, 22(2):341–349, 2007.

[80] J. Mann. The spatial structure of neutral atmospheric surface-layer turbulence. *J. Fluid Mech*, 273:141–168, 1994.

[81] J. Meyers and C. Meneveau. Optimal turbine spacing in fully developed wind farm boundary layers. *Wind Energy*, 15(2):305–317, 2011.

[82] T. Mikkelsen, N Angelous, K. Hansen, M. Sjholm, M. Harris, C. Slinger, P. Hadley, and R. Scullion. A spinner-integrated wind LiDAR for enhanced wind turbine control. *Wind Energy*, 16:625–643, 2013.

[83] P. Milan, M. Wächter, and J. Peinke. Turbulent character of wind energy. *Phys. Rev. Lett.*, 110(13):138701, 2013.

[84] Chin-Hoh Moeng. A large-eddy-simulation model for the study of planetary boundary-layer turbulence. *Journal of the Atmospheric Sciences*, 41 (13):2052–2062, 1984.

[85] Chin-Hoh Moeng and Peter P Sullivan. A comparison of shear-and buoyancy-driven planetary boundary layer flows. *Journal of the Atmospheric Sciences*, 51(7):999–1022, 1994.

[86] EE Morfiadakis, GL Glinou, and MJ Koulouvari. The suitability of the von karman spectrum for the structure of turbulence in a complex terrain wind farm. *J. Wind Eng. Ind. Aerod.*, 62(2):237–257, 1996.

[87] T. Mucke, D. Kleinhans, and J. Peinke. Atmospheric turbulence and its influence on the alternating loads on wind turbines. *Wind Energy*, 14: 301–316, 2011.

[88] Joaquín Mur-Amada and Ángel A Bayod-Rújula. Characterization of spectral density of wind farm power output. In *9th International Conference on Electrical Power Quality and Utilisation*, pages 1–6, 2007.

[89] L. D. Nelson, L. Manuel, H. J. Sutherland, and P. S. Veers. Statistical analysis of wind turbine inflow and structural response data from the list program. *J. Sol. Energ.-T. ASME*, 125(4):541–550, 2003.

[90] Amin Niayifar and Fernando Porté-Agel. A new analytical model for wind farm power prediction. In *J. Phys. Conf. Ser.*, volume 625, page 012039, 2015.

[91] Yuji Ohya. Wind-tunnel study of atmospheric stable boundary layers over a rough surface. *Bound-Lay Meteorol*, 98(1):57–82, 2001.

[92] Valery L Okulov, Igor V Naumov, Robert F Mikkelsen, Ivan K Kabardin, and Jens N Sørensen. A regular strouhal number for large-scale instability in the far wake of a rotor. *Journal of Fluid Mechanics*, 747:369–380, 2014.

[93] A. Ozbay, W. Tian, Z. Yang, and H. Hu. An experimental investigation on the wake interference of multiple wind turbines in atmospheric boundary layer winds. *AIAA Paper*, 2012.

[94] Lucy Y Pao and Kathryn E Johnson. A tutorial on the dynamics and control of wind turbines and wind farms. In *American Control Conference, 2009.*, pages 2076–2089, St. Louis, MO, 2009. IEEE.

[95] A. Peña and O. Rathmann. Atmospheric stability-dependent infinite wind-farm models and wake-decay coefficient. *Wind Energ.*, 17(8):1269–1285, 2014.

[96] F. Porté-Agel, Y. T. Wu, H. Lu, and R. J. Conzemius. Large-eddy simulation of atmospheric boundary layer flow through wind turbines and wind farms. *J. Wind Eng. Ind. Aerod.*, 99.4:154–168, 2011.

[97] C. Potter and M. Negnevitsky. Very short-term wind forecasting for Tasmanian power generation. *IEEE T. Power Syst.*, 21.2(1):956–972, 2006. ISSN 1099-1824.

[98] D. Quarton and J. Ainslie. Turbulence in wind turbine wakes. *J. Wind Eng.*, 14:15–23, 1989.

[99] ÁG González Rodríguez, A González Rodríguez, and M Burgos Payán. Estimating wind turbines mechanical constants. In *Proceedings of the International Conference on Renewable Energy and Power Quality*, volume 7, Seville, 2007. European Association for the Development of Renewable Energies, Environment and Power Quality.

[100] A Rosen and Y Sheinman. The power fluctuations of a wind turbine. *J. Wind Eng. Ind. Aerod.*, 59(1):51–68, 1996.

[101] PB S. Lissaman. Energy effectiveness of arbitrary arrays of wind turbines. *Journal of Energy*, 3(6):323–328, 1979.

[102] B. Sanderse, S.P. van der Pijl, and B. Koren. Review of computational fluid dynamics for wind turbine wake aerodynamics. *Wind Energ.*, 14: 799–819, 2011.

[103] A. Sathe, T. Barlas, W. A. A. M. Bierbooms, and G. J. W. van Bussel. Influence of atmospheric stability on wind turbine loads. *Wind Energy*, 16(7):1013–1032, 2013.

[104] Ameya Sathe and Wim Bierbooms. Influence of different wind profiles due to varying atmospheric stability on the fatigue life of wind turbines. In *Journal of Physics: Conference Series*, volume 75(1), page 012056. IOP Publishing, 2007.

[105] Wolfgang Schlez and David Infield. Horizontal, two point coherence for separations greater than the measurement height. *Boundary-Layer Meteorology*, 87(3):459–480, 1998.

[106] David Schlipf, Dominik Johannes Schlipf, and Martin Kühn. Nonlinear model predictive control of wind turbines using lidar. *Wind Energy*, 16 (7):1107–1129, 2013.

[107] H Shiu, C P van Dam, E Johnson, M Barone, R Phillips, W Straka, A Fontaine, and M Jonson. A design of a hydrofoil family for current-driven marine-hydrokinetic turbines. In *Proceedings of the 2012 20th International Conference on Nuclear Engineering collocated with the ASME 2012 Power Conference ICONE20-POWER2012*. American Society of Mechanical Engineers, 2012.

[108] H. Shiu, C.P. van Dam, E. Johnson, M. Barone, R. Phillips, W. Straka, A. Fontaine, and M. Jonson. A design of a hydrofoil family for current-driven marine-hydrokinetic turbines. *Proceedings of the 20th International Conference on Nuclear Engineering and the American Society of Mechanical Engineers 2012 Power Conference*, pages 839–847, 2012.

[109] Mahmood M Shokrieh and Roham Rafiee. Simulation of fatigue failure in a full composite wind turbine blade. *Composite structures*, 74(3):332–342, 2006.

[110] Eric Simley, Lucy Y Pao, Neil Kelley, Bonnie Jonkman, and Rod Frehlich. Lidar wind speed measurements of evolving wind fields. In *50th AIAA Aerospace Sciences Meeting including the New Horizons Forum and Aerospace Exposition*, number AIAA 2012-0656, 2012.

[111] Joseph Smagorinsky. General circulation experiments with the primitive equations: I. the basic experiment. *Monthly weather review*, 91(3):99–164, 1963.

[112] Zbigniew Sorbjan. *Structure of the atmospheric boundary layer.* Prentice Hall, Englewood Cliffs, NJ, 1989.

[113] J. N. Sørensen and W. Z. Shen. Numerical modeling of wind turbine wakes. *J. Fluid Eng-T ASME*, 124.2:393–399, 2002.

[114] Poul Sørensen, Anca D Hansen, and Pedro André Carvalho Rosas. Wind models for simulation of power fluctuations from wind farms. *J. Wind Eng. Ind. Aerod.*, 90(12):1381–1402, 2002.

[115] J.N. Sørenson. Aerodynamic aspects of wind energy conversion. *Annu. Rev. Fluid Mech.*, 43:427–448, 2011.

[116] Gerald Steinfeld, Jens Tambke, Joachim Peinke, and Detlev Heinemann. Application of a large-eddy simulation model to the analysis of flow conditions in offshore wind farms. In *EGU General Assembly Conference Abstracts*, volume 12, page 8320, Göttingen, Germany, 2010. Copernicus Publications.

[117] Richard JAM Stevens and Charles Meneveau. Temporal structure of aggregate power fluctuations in large-eddy simulations of extended windfarms. *Journal of Renewable and Sustainable Energy*, 6(4):043102, 2014.

[118] Geoffrey Ingram Taylor. The spectrum of turbulence. In *Proc. R. Soc. London Ser.*, volume 164, pages 476–490, 1938.

[119] H Tennekes. Eulerian and lagrangian time microscales in isotropic turbulence. *Journal of Fluid Mechanics*, 67(3):561–567, 1975.

[120] Wei Tian, Ahmet Ozbay, Wei Yuan, Partha Sarakar, and Hui Hu. An experimental study on the performances of wind turbines over complex terrain. In *51st AIAA Aerospace Sciences Meeting including the New Horizons Forum and Aerospace Exposition*, number AIAA 2013-0612, 2013.

[121] N Tobin, H Zhu, and LP Chamorro. Spectral behaviour of the turbulence-driven power fluctuations of wind turbines. *Journal of Turbulence*, 16(9): 832–846, 2015.

[122] N. Tobin, A. M. Hamed, and L. P. Chamorro. Fractional flow speed-up from porous windbreaks for enhanced wind-turbine power. *Bound-Layer Meteorol*, 163(2):253–271, 2017.

[123] Nicolas Tobin and Leonardo P Chamorro. Turbulence coherence and its impact on wind-farm power fluctuations. *Journal of Fluid Mechanics*, 855: 1116–1129, 2018.

[124] Nicolas Tobin, Ali M. Hamed, and Leonardo P. Chamorro. An experimental study on the effects of winglets on the wake and performance of a model wind turbine. *Energies*, 8:11955–11972, 2015.

[125] Juan-José Trujillo, Ferhat Bingöl, Gunner C Larsen, Jakob Mann, and Martin Kühn. Light detection and ranging measurements of wake dynamics. part ii: two-dimensional scanning. *Wind Energy*, 14(1):61–75, 2011.

[126] Luong Van Binh, Takeshi Ishihara, Pham Van Phuc, and Yozo Fujino. A peak factor for non-gaussian response analysis of wind turbine tower. *J. Wind Eng. Ind. Aerod.*, 96(10):2217–2227, 2008.

[127] Ahmadreza Vasel-Be-Hagh and Cristina L Archer. Wind farm hub height optimization. *Applied energy*, 195:905–921, 2017.

[128] L. J. Vermeer, J. N. Sørenson, and A. Crespo. Wind turbine wake aerodynamics. *Prog. Aerosp. Sci.*, 39:467–510, 2003.

[129] Theodore Von Karman. Progress in the statistical theory of turbulence. *Proc. Natl. Acad. Sci. U.S.A.*, 34(11):530–539, 1948.

[130] SG Voutsinas, KG Rados, and A Zervos. On the analysis of wake effects in wind parks. *Wind Eng.*, 14:204–219, 1990.

[131] M Wilczek and Y Narita. Wave-number–frequency spectrum for turbulence from a random sweeping hypothesis with mean flow. *Phys. Rev. E.*, 86(6):066308, 2012.

[132] Michael Wilczek, Richard JAM Stevens, and Charles Meneveau. Spatio-temporal spectra in the logarithmic layer of wall turbulence: large-eddy simulations and simple models. *Journal of fluid mechanics*, 769, 2015.

[133] Ryan Wiser and Mark Bolinger. 2016 wind technologies market report. Technical report, Department of Energy, Office of Energy Efficiency and Renewable Energy, 2016.

[134] Shengbai Xie and Cristina Archer. Self-similarity and turbulence characteristics of wind turbine wakes via large-eddy simulation. *Wind Energ.*, 18(10):1815–1838, 2015.

[135] Shengbai Xie, Cristina L Archer, Niranjan Ghaisas, and Charles Meneveau. Benefits of collocating vertical-axis and horizontal-axis wind turbines in large wind farms. *Wind Energy*, 20(1):45–62, 2017.